FAILURE OF CREEP BRITTLE MATERIALS

Thesis submitted for the degree of

Doctor of Philosophy

at the University of Leicester

by

Julian David James De Voy BSc (Leicester)

Department of Engineering

University of Leicester

October 1993

UMI Number: U051711

UMI

Dissertation Publishing

UMI U051711

ProQuest

ProQuest LLC
789 East Eisenhower Parkway
P.O. Box 1346
Ann Arbor, MI 48106-1346

If the Lord Almighty had consulted me
before embarking upon Creation, I should
have recommended something simpler.

Alfonso X [Att.]

ACKNOWLEDGEMENTS

List of Contents

NOMENCLATURE LIST

A   Constant of proportionality

A_0 A specified definite integral

a   Crack size

a_c Critical crack size

a_i Constant in theta projection

           Initial crack size

$\dot{a}$ Crack growth rate

$\bar{a}$ Normalised crack growth rate

B_0 Constant of proportionality

b   bredth

b_i Constant in theta projection

C^* Rate equivalent of the path independent integral J

$C(t)$ Time dependent variation of C^*

C_h^* C^* incorporating the effects of strain hardening

$\overline{C^*}$ Normalised form of C^*

C_{MG} Monkman-Grant constant

c_i Constant in theta projection

$c_{1,2}$ Constants

D   Diffusion coefficient

           Constant in Kachanov's kinetic law of creep damage

           Distance between outer reference points for measuring creep deflection

D_b Boundary diffusivity

d   depth

d_i Constant in theta projection

ds   Element of contour

$d\epsilon^p$ Increment in plastic strain at collapse

E   Young's modulus

F   Volume fraction of void

F_1 Volume fraction of void at nucleation

F_2 Volume fraction of void at failure

f   Area fraction of void

      A function (of specified argument)

f_1 Area fraction of void at nucleation

f_3 A function of the creep exponent

f_{ij} Function of angle

G   Elastic energy release rate

      A specified function of its arguement

$g_{1,2}(n)$ Dimensionless functions of creep exponent

I_n Dimensionless function of creep exponent

J   A path independent integral

$\dot{J}$ An alternative symbol for C*

K   Elastic stress intensity factor

K_I Mode one elastic stress intensity factor

k   Boltzmann's constant

k_t stress concentration factor

k_c An alternative definition of stress concentration factor

l grain size

M   Applied bending moment

M_L Limit moment

M_n Applied bending moment on notched specimen

M_p Applied bending moment on profiled specimen

M'   Equivalent bending moment in profiled specimen

m   Weibull modulus

A constant to determine the shape of the displacement rate field

n   Creep exponent

P   Load

P_L Limit load

$P(\sigma)$ Larson-Miller parameter

Q   Activation energy

R   Length of the damage zone

Reliability

Radius of curvature

$\overline{R}$ Normalised damage zone size

$\tilde{R}$ Universal gas constant

r   Void radius

Distance from crack tip

$r_{1,2}$ Principal radii of void

r_c Extent of creep dominant region

r_e Extent of elastic region

r_{HR} Extent of the HR field

r^*	Point at which creep and elastic strain rates are equal
S_{ij}	The stress deviator $\equiv \sigma_{ij} - \frac{1}{3}\sigma_{kk}$
T	Absolute temperature
T_a	Absolute ambient temperature
T_e	Absolute exhaust temperature
T_m	Absolute melting point
$\tilde{T}$	Traction vector
t	Time
t_d	Design lifetime
t_f	Time to failure
t_{fn}	Time to failure of a notched specimen
t_{fp}	Time to failure of a profiled specimen
t_R	Failure time ratio $= t_{fn}/t_{fp}$
U	Elastic energy
u	Displacement
$\dot{u}$	Displacement rate
$\dot{u}_0$	Characteristic displacement rate
$\bar{u}$	Normalised displacement rate
V	Volume
V_T	Volume in tension
v	volume
W	energy
W	Dimension of standard crack growth specimen
$\overline{W}$	Work

x	Cartesian coordinate
$\bar{x}$	$= x/R$
y	Distance from neutral axis
z	No. of grains in the damage zone
α	Factor equal to unity in plane stress, and $1-\nu^2$ in plane strain
	Ratio of compressive to tensile yield strength
Γ	Contour of integration
γ	Surface energy
δ	Displacement within the damage zone
	Mid-point deflection of bend specimen
$\dot{\delta}$	Displacement rate within the damage zone
$\dot{\delta}_t$	Crack tip opening displacement rate
δ_b	Grain boundary thickness
δ_t	Critical crack tip opening displacement
$\bar{\delta}_t$	Normalised critical crack tip opening displacement
δ_{ij}	Unit tensor
ϵ	Strain
ϵ_c	Creep strain
ϵ_d	Design strain
ϵ_e	Elastic strain
ϵ_f	Strain to failure
ϵ_t	Accumulated strain at time t
ϵ_{ij}	Strain tensor
$\dot{\epsilon}_{ij}$	Strain rate tensor

$\dot{\epsilon}_{ij}^{c}$ Creep strain rate tensor

$\dot{\epsilon}_{ij}^{e}$ Elastic strain rate tensor

ϵ_0 Reference strain

$\dot{\epsilon}$ Strain rate

$\dot{\epsilon}_c$ Creep strain rate

$\dot{\epsilon}_e$ Elastic strain rate

$\dot{\epsilon}_0$ Reference strain rate

η Viscosity

      Efficiency

θ Angle

θ_i Constant in theta projection

λ Half mean void spacing

$\bar{\lambda}$ Normalised half mean void spacing

μ Potential

ν Poisson's ratio

ξ A normalised crack growth rate

$\dot{\rho}$ Nucleation rate

σ Stress

σ_I Maximum principal tensile stress

σ_{max} Maximum stress

σ_{peak} Peak stress in notched component

σ_γ Sintering stress

$\sigma_{\gamma n}$ Capillarity stress at nucleation

$\sigma_{\gamma 0}$ Reference stress below which damage is small scale

σ_e equivalent tensile stress

σ_0 Reference stress

            Weibull normalising stress

σ_0^F Reference stress for failure

σ_{ij} Stress tensor

σ_{kk} $\sigma_{11} + \sigma_{22} + \sigma_{33}$

$\tilde{\sigma}_{ij}(\theta)$ Dimensionless function of θ

$\psi(\sigma_{ij}^{\infty})$ Stress distribution

σ_y Yield stress

ϕ Constant in Kachanov's kinetic law of creep damage

ϕ_0 Ratio of diffusive to power law creep rates

χ, ς Constant in Kachanov's kinetic law of creep damage

            Characteristic length for creep

Ω Mean atomic volume

ω Kachanov's damage parameter

$\dot{\omega}$ Rate of change of Kachanov's damage parameter

$\dot{\omega}_0$ Reference value of $\dot{\omega}$

CHAPTER ONE: INTRODUCTION

In this thesis we investigate the high temperature behaviour of brittle materials with particular attention being paid to the transition from ductile to brittle behaviour.

The title of this thesis is 'Failure of Creep Brittle Materials' and by using the word 'materials' it is intended to emphasise the generic nature of the research presented here. Whilst the emphasis in the main text is towards ceramic materials, culminating in a discussion of our experimental work on reaction bonded silicon nitride, it should be remembered that the models developed here are not intended to be applicable solely to ceramics but are equally applicable to brittle metals.

1.1   Failure of engineering materials at high temperatures.

In order to design with a material it is necessary first to understand the ways in which the material is likely to fail in use; and materials fail at high temperatures in a manner which is quite different from their room temperature behaviour.

At low temperatures crystalline materials fail either by cleavage (except for the more common f.c.c. metals), in which cracks propagate along preferentially oriented crystallographic planes, or by brittle intergranular fracture. At higher temperatures different failure mechanisms dominate.

Fracture mechanism maps provide a simple means of identifying the regions, in stress-temperature space, over which particular failure mechanisms dominate. They may be constructed either empirically, by collating failure data for the material in question or theoretically by modelling the individual failure mechanisms. A number of these maps are presented in Figure 1.1.

At temperatures above the brittle-ductile transition, cleavage and brittle intergranular fracture are replaced as the dominant mechanisms by ductile

transgranular fracture in which decohesion at second phase particles nucleates cavities which grow by plastic straining of the surrounding material. A high load may result in almost instantaneous failure of the material as the effective cross section is reduced by cavitation. If, however, the net section stress is maintained constant or the specimen is tested under displacement control then very large deformations are possible providing that the material does not neck.

The behaviour described above is essentially time independent but at higher temperatures the material behaviour starts to become time dependent. This time dependent plasticity is called creep and it is this phenomenon, with particular reference to brittle materials, with which this thesis is concerned. The temperatures required for creep vary from material to material but generally a temperature in excess of about 30% of the absolute melting point, T_m, is required for metals and one in excess of about 40% of T_m for ceramics.

The scientific study of creep as a phenomenon started with Phillips' work on metal wires[1] in the early 1900's, and over the past 40 years a large amount of data has been collected on the creep of metals. The development of research into the creep of ceramics took rather longer as the recurring problem of their susceptibility to thermal shock lead engineers initially to believe that they would have no use in high temperature applications.

When a solid is loaded at a high temperature it deforms slowly with time. If the strain, ϵ, is plotted as a function of time then a creep curve of the type shown in Figure 1.2 may be obtained. This Figure defines the instantaneous elastic and/or plastic strain and the regions of primary, steady state (or secondary) and tertiary creep.

The shape of the curve in the primary region, where the creep rate decreases

until it reaches its steady state value, is due to the effect of strain hardening as a dislocation structure develops within the material. In the steady state region the rate of strain hardening is balanced by the rate of creep recovery and the creep strain rate (the slope of the creep curve - commonly referred to as the creep rate) is therefore constant. Different materials may produce variations on this form of curve but as a schematic it is generally agreed that it represents the behaviour of by far the majority of materials. We say 'generally agreed', but the validity of the primary, secondary, tertiary curve is not *universally* accepted. There is an alternative view held by some workers[2] that real materials do not in fact display a secondary creep phase and that there is a transition from primary to tertiary creep without a steady state. The so called 'theta projection' method (described more fully in Chapter 2) has been developed to describe creep behaviour in terms of the competition between primary and tertiary effects; without the need for secondary creep. However, as theta projection is complicated, and a consensus has yet to be reached as to its validity, or not, in this thesis we will assume that the materials we consider do display steady state behaviour.

Experimentation has shown that, for a wide range of materials and creep conditions, the steady state creep rate, $\dot{\varepsilon}$, is proportional to the applied stress, σ, raised to a power, n, known as the creep index or creep exponent.

$$\dot{\varepsilon} = A\sigma^n \qquad (1.1)$$

This form of relationship was first proposed by Norton[3] in 1929 and is known as Norton's law. In a more general form this law may be written as

$$\dot{\varepsilon} = \dot{\varepsilon}_0 \left(\frac{\sigma}{\sigma_0}\right)^n \qquad (1.2)$$

The constant of proportionality in Norton's Law, A, is of the form

$$A \propto D \exp\left(-\frac{Q}{\tilde{R}T}\right) \qquad (1.3)$$

where $\tilde{R}$ is the universal gas constant; Q is the activation energy for the particular mechanism and D is the diffusion coefficient. The constant of proportionality is mechanism dependent but in any case the diffusion coefficients are known so imprecisely that the expressions are best used qualitatively to describe the creep mechanism rather than to obtain numerical results.

1.2   Power law creep.

At high stresses the creep index, n, is commonly found to be in the range 2 to 8. This is known as power law creep and occurs as a result of the movement or 'glide' of dislocations under the action of an applied stress.

When a crystalline material deforms plastically the stress to cause yielding is that required for the dislocations to overcome the intrinsic lattice resistance plus any additional resistance which may be due, for example, to the effect of precipitate hardening. When the material is stressed the dislocations glide along slip planes until they meet an obstruction (a precipitate particle, for example). Dislocations so obstructed cannot glide around the obstruction. However, if the atoms in the material above the dislocation can diffuse away, the dislocation can pass around the obstruction. This mechanism is called 'dislocation climb' and is the rate controlling stage of the process. The energy required for it to occur comes from variations on an atomic level in the thermal energy of the individual atoms within the material. The literature on power law creep has been reviewed by Cannon and Langdon[4] who list 16 different possible mechanisms with stress exponents ranging from 3 to 6. Although there is no theoretical basis for supposing it to be so, 15 of these 16

propose integer values for the creep exponent n.

1.3 Linear viscous creep.

At lower stress levels n often equals unity. This is referred to as linear viscous creep and also occurs as a result of diffusion.

Individual atoms diffusing through a crystalline material may diffuse either through the bulk of the material or along the grain boundaries. This leads to a redistribution of material and hence to creep. In practice both paths are followed simultaneously by different atoms. However, if the material comprises small grains and the temperature is at the low end of the creep range then intergranular diffusion will be the dominant mechanism. Conversely coarse grained materials at higher temperatures show predominantly transgranular diffusion.

In the early 1960's Coble[5] established that for intergranular creep the strain rate, $\dot{\epsilon}$ is given by

$$\dot{\epsilon} \propto \frac{\sigma \Omega D_b \delta_b}{kTl^3} \qquad (1.4)$$

Where l is the mean grain size; $D_b \delta_b$ is the boundary diffusion coefficient times the boundary thickness; T is the absolute temperature; k is Boltzmann's constant and Ω is the mean atomic volume. The exact value of the constant of proportionality is relatively unimportant as it depends to a large extent on the accuracy to which $D_b \delta_b$ is known, however Coble predicted a value of 150 and, more recently, different values such as 36[6] have been proposed. The significant result, however, is that $\dot{\epsilon}$ is proportional to the stress as observed, and that it is inversely proportional to the cube of the grain size. Coble's work was so well received that creep controlled by boundary diffusion is now better known as Coble creep. For the same reason creep arising from the diffusive flux of vacancies through the grains is better known as

Nabarro-Herring creep[7,8]. Nabarro and Herring's result is similar to Coble's except that they predict a creep rate inversely proportional to the square of the grain size; this weaker dependence on grain size agreeing with the observation that Nabarro-Herring creep is the dominant mechanism in large grained materials.

1.4 Nucleation of voids.

Materials may creep solely as the result of stress directed diffusion of matter through virgin material, however, more often than not, microscopic examination of the material reveals that creep is associated with the presence of voids and/or microcracks, collectively referred to as creep damage. At the microscopic level damage is considered to become a crack when its principle dimension exceeds some characteristic length for the damaging process, for example the grain size. The presence of this damage means that if the material is subjected to a constant load the stress on the undamaged ligaments of material must increase, leading to more damage. It is as a direct consequence of the coupling of these two processes that the creep rate in the tertiary region of the creep curve increases up to fracture.

The nucleation process is of particular importance in metals which are, generally speaking, fully dense in the first place, and less so in ceramic materials which nearly always contain pre-existing voids, usually introduced during fabrication. However as much of the theoretical work presented here is generic, a brief description of two of the more significant models of void nucleation will be given.

Classical nucleation theory models nucleation as the result of the condensation of vacancies on stressed grain boundaries. Raj and Ashby[9] have calculated a rate of nucleation, $\dot{\rho}$,

$$\dot{\rho} \propto \exp\left(\frac{-\sigma\Omega}{kT}\right) \qquad\qquad (1.5)$$

and similar models have been put forward for nucleation in ceramic materials.

Argon[10] has shown that equation (1.5) indicates that stresses of the order of E/100 would be required for significant nucleation. Clearly, stresses of this order are much too high to be produced solely as the result of the direct application of a load and so if this mechanism is correct some form of stress concentration must be present if voids are to nucleate.

The presence of grain boundary particles and triple points combined with grain boundary sliding have been suggested as possibly causing sufficiently large stress concentrations. Argon et. al.[11] have demonstrated that by far the most significant stress concentrations are produced at grain boundary particles and experimental evidence in support of their result has been produced by Grant and Mullendore[12] who have demonstrated that cavities will not nucleate solely as a result of grain boundary sliding without the presence of included particles.

A second explanation of void nucleation, and one which appears to be more significant at lower temperatures, is the postulated requirement for a critical plastic strain for nucleation. Goods and Nix[13], and Dyson[14] have produced experimental evidence which supports this theory. Metallic specimens were pre-strained to nucleate voids and the times and strains to failure of these specimens, when creep tested, were compared with specimens which had not been pre-strained. They found that the presence of pre-existing voids reduced the failure time by an order of magnitude and the strain to failure by 2/3, the difference between the two strains representing that required to cause nucleation.

The fact that there is experimental evidence to show that 90% of the time

taken for a specimen to fail as a result of creep cavitation may be that required to nucleate the cavities and that therefore only 10% of the failure time is required for them to grow from nucleation to failure indicates the importance of void nucleation in the failure process.

1.5 Void growth.

At much lower stresses than those required for growth due to plastic flow competition between two different rate controlling processes governs the diffusive growth of grain boundary voids. If diffusion of material on the surface of the void is more rapid than in the grain boundary then atoms on the surface of the void have time to redistribute themselves by diffusion and the void will maintain its lenticular equilibrium shape. This mechanism is called boundary controlled diffusion and has been analysed in detail by, amongst others, Hull and Rimmer[15], Speight and Harris[16] and Raj and Ashby[9].

Raj and Ashby, by solving the governing equation for stress directed diffusion of matter from a void have obtained an expression for its rate of change of volume, under the action of an applied stress, σ. If the void is sufficiently large that sintering can be ignored then Raj and Ashby's result can be approximated by[17]

$$\frac{dv}{dt} = \frac{2\pi D_b \delta_b \sigma \Omega (1-f)}{kT \ln\left(\frac{1}{\sqrt{f}}\right)} \qquad (1.6)$$

where f is the area fraction of a boundary occupied by a void, defined by the expression

$$f = \frac{r^2}{\lambda^2} \qquad (1.7)$$

where, in turn, r is the radius of a void in the plane of the grain boundary and λ is

half the void spacing.

The other limiting condition occurs when diffusion in the grain boundary is faster than over the surface of the void. In this surface controlled diffusion limit, matter is removed more rapidly from the edge of the void than it can redistribute over its surface and the void loses its equilibrium shape becoming flatter and more crack-like. This process has been studied by, for example, Chuang et al[18].

Equations are presented for growth controlled by diffusion in the grain boundary and not for the other mechanisms mentioned because this mechanism is analysed in detail later in the text.

As well as growing by diffusion void growth may also occur as a result of power law creep of the surrounding material[19] or as a result of a combination of both power law creep and diffusion[20,18,21].

For completeness we should note that at very high temperatures the rate of diffusion (which increases exponentially with temperature) becomes so rapid that, for tensile specimens in particular, failure as a result of dynamic recrystallisation can occur. However this is a quite separate phenomenon from creep and so will not be discussed further.

1.6 Creep crack growth.

Dalgleish et. al.[22] in their experimental work on the creep of polycrystalline alumina have shown that creeping ceramics may fail in two quite different ways. In both instances the failure is associated with the presence of damage. At low stresses there is sufficient time for any pre-existing cracks to blunt and failure eventually occurs as the result of a net section stress effect. This low stress behaviour is common to both metals and ceramics.

At high stresses metals fail plastically, whereas at high stresses for ceramics,

and intermediate stress levels for metals, failure occurs as the result of the creep growth and linkage of this damage with the crack tip, a process known as creep crack growth; failure finally occurs when one crack becomes so large that the critical stress intensity factor (defined below) is exceeded and the specimen fails in a brittle manner.

It would however be wrong to infer that creep crack growth is not a significant failure mechanism in metals; indeed it was first identified as a phenomenon in metallic components in power generating plant. Creep ductile metals are, by definition, not prone to failure as a result of creep crack growth. However high temperature structural alloys, such as the nickel based alloy nimonic 80A are, when compared with ductile metals, comparatively brittle and it is these creep brittle materials which are susceptible to failure as a result of creep crack growth.

The earliest reference in the literature to creep crack growth that the author could find is from 1970[23]. Since then it has been the subject of extensive work by numerous authors and the area has been reviewed many times[eg. 24,25] and is reviewed again in Chapter two.

1.7 Fracture mechanics and crack tip stress fields.

A crack in a solid can be stressed in any one, or a combination, of three orthogonal modes, see Figure 1.3. The stress distribution around the tip of a mode I crack can be written in the generalised form

$$\sigma_{ij} = \frac{K_I}{\sqrt{2\pi r}} f_{ij}(\theta) \qquad (1.8)$$

Where the factor K_I is known as the stress intensity factor and uniquely defines the state of stress at the crack tip; r and θ are the polar coordinates of the point at

which the stress σ_{ij} is determined. K_I is given by

$$K_I = \sigma \sqrt{\pi a}\, f\,(a/w) \qquad (1.9)$$

where a specimen of width w, containing a crack of size a, is subjected to a remote

tensile stress σ. For a crack in an infinite plate the function $f\,(a/w)$ goes to unity.

Equation (1.9) is in fact an approximation to the complete solution, being the

first term in a series; further away from the tip the approximation becomes less

accurate and additional terms have to be considered. Mode II and III cracks are

similarly characterised by K_{II} and K_{III} respectively and also show an inverse square

root dependence on the distance from the crack tip.

In 1921 Griffith[26] postulated that crack propagation will occur if the elastic

energy released when a crack grows is greater than or equal to that required for the

growth to occur. Based upon the earlier work of Inglis[27], Griffith calculated the

change in the elastic energy, dU, when an elliptical flaw of length 2a grows by an

amount da, as being

$$-\frac{dU}{da} = \frac{2\pi\sigma^2 a}{E} \equiv 2G \qquad (1.10)$$

where G is the elastic energy release rate per crack tip. From equations (1.9) and

(1.10) we can see that for plane stress

$$\frac{K^2}{E} = G \qquad (1.11)$$

while for plane strain the K^2 term must be replaced by $K^2(1-\nu^2)$.

The stress field equations presented above are elastic solutions and Griffith's

postulate is based on experimentation on glass, a very brittle material. In ductile

materials like metals, yielding prohibits the singularity of stress predicted by the

elastic equations. However, it is possible, within limits, to correct for the effects of plasticity and still make use of the linear elastic fracture mechanics (LEFM) equations. Two such methods of correction are due to Irwin[28] and Dugdale[29]. Dugdale's method will be briefly described as the models developed later in this thesis are of the Dugdale type.

Dugdale considered the crack to be of an effective length that is longer than its physical length, see Figure 1.4. The uncracked strip in front of the physical crack is assumed to support the yield stress (ie. the zone is plastic) which tends to close the crack, and is of a length, R, chosen so that the elastic stress singularity disappears.

Other corrections for the plastic zone have been proposed but provided that the plastic zone is small compared with the crack size then the LEFM equations still apply. This criterion

$$R \ll a \qquad (1.12)$$

is known as the small scale yield criterion and is particularly significant as it will be modified and extended to creep damage later in this thesis. If this criterion is violated, and the plastic zone becomes too large, it may still be valid to correct for the size of the plastic zone but the linear elastic equations no longer hold as they are only valid close to the crack tip.

Thus by the early 1960s the elastic stress distribution ahead of a crack tip was known and problems involving limited plasticity could be solved approximately, but there was, as yet, no solution for problems involving large scale plasticity. An exact solution to such a problem would require an analytic solution to the elastic-plastic crack tip stress field. Toward the end of the 1960s a method which

circumvented the need for such a solution was developed.

In 1968 Rice[30] proved the path independence of the integral, J, for an elastic /plastic solid, where J is given by

$$J = \oint_\Gamma \left(W dx_2 - \bar{T}\frac{du_i}{dx_1} ds \right) \qquad (1.13)$$

and where $\qquad W = \int \sigma_{ij}\, de_{ij} \qquad (1.14)$

See Figure 1.5 for definitions of the terms. For the elastic case J can be evaluated using the known elastic stress field solution, and Rice has shown that this leads to the result

$$J = G \qquad (1.15)$$

But the usefulness of J is that the integral is also valid if there is appreciable plasticity at the crack tip and its path independence means that the stress field ahead of a crack in a plastic material may be characterised in terms of the behaviour in the far field away from the plastic zone. However the path independence of J strictly only holds for the deformation theory of plasticity which does not allow for the unloading which occurs during crack growth. J as a means of characterising the stress field ahead of the crack tip is therefore restricted to crack initiation.

Previously in 1954 Hoff[31], had demonstrated that a problem involving a creeping structure may be transformed to an equivalent problem in elasticity or vice versa by replacing strains by strain rates and displacements by displacement rates in the relevant constitutive equations. This elastic-viscous analogy allowed Landes and Begley[32] and Nikbin et. al.[33] to produce an expression that is the rate equivalent of the J integral, C* (pronounced "see-star"; some workers use $\dot{J}$ but C*

is the more common term now).

For a two dimensional crack C* can be expressed as a contour integral analogous to that used to determine J

$$C^* = \oint_\Gamma \left(\bar{W} dx_2 - \tilde{T} \frac{d\dot{u}_i}{dx_1} ds \right)$$ (1.16)

where
$$\bar{W} = \int \sigma_{ij} d\dot{e}_{ij}$$ (1.17)

The slightly different terms in these expressions are also defined in Figure 1.5. The significance of this integral is the same as that of J in that its path independence provides a means of relating the stresses in the far field of a time dependent cracked body to conditions at the crack tip.

In principle C* can be determined analytically by direct integration of equation (1.16). This obviously requires knowledge of the complete stress field, σ_{ij}, and is usually done by computer using the finite element method.

In practice C* is determined by testing a pair of cracked specimens which are identical except that the crack in one of the specimens is longer, by an amount, da than the other. C* for the configuration is related to the rate of change of energy dissipation with respect to the change in crack length and is obtained by differentiating the area under the load displacement rate curve with respect to the crack length, see Figure 1.6.

$$C^* = \frac{\partial}{\partial a} \int_0^{\dot{u}_0} P \, d\dot{u}$$ (1.18)

Also, simple approximate expressions for C* have been developed, such as that due to Ainsworth[34], which will be described in Chapter two, which obviate the need for the complicated specimen testing described above.

For the special case of linear viscous creep there is a direct relationship between C^*, the elastic stress intensity factor K, and the material viscosity, η

$$K^2 = 3\eta C^* \tag{1.19}$$

and it is the relationship, and competition, between elastic effects characterised by K and creep effects, characterised by C^*, which is the underlying theme of this thesis.

In Chapter two we present a more extensive review of the literature on creep crack growth in both metals and ceramics.

In Chapter three we determine criteria for the changeover from K to C^* controlled creep crack growth. These criteria enable us to produce maps showing regions of C^* and K controlled creep. Real test data where C^* or K control are claimed are plotted on these maps where the validity of the claims can be established. It is also shown how the maps can also be used as design and assessment aids.

Simple equations for void growth rates such as the approximation to Raj and Ashby's result, given in equation (1.6) are overly conservative in that they significantly underestimate the times to rupture of real components as a consequence of overestimating the void growth rates found in practice. In reality a growing void is constrained by the surrounding material and thus grows more slowly than it would without this constraint. In Chapter four we assume all the damage to be contained within a process zone or 'damage zone' (analogous to Dugdale's plastic strip model already mentioned) ahead of the crack tip and examine the limiting cases of fully constrained crack growth (ie. the damaged material is infinitely more compliant than the surrounding material) and

unconstrained crack growth (vice versa) and we determine the relationships between the crack growth rate and the size of the damage zone. A new result based on an assumption of a prescribed variation of displacement rate within the damage zone is presented. These three idealised cases are combined to produce an overall relationship between the creep crack growth rate and the damage zone size for a real material. These results are compared, for linear creep, with those of another model due to Thouless et. al.[35] in which the constraint in the damage zone is modelled using dislocation theory. In Thouless' model an array of dislocations is considered to lie in the plane of the crack, ahead of the tip, modelling the displacements of each grain. The sum of the Burger's vectors at each point corresponding to the displacement of that grain. The compressive stress at a given distance from the crack tip due to a particular dislocation is a standard result from dislocation theory and so the total stress field ahead of the crack can be found by superposition. Our results are shown to agree well with Thouless' but our model has the advantage over his that it is not restricted to linear creep.

In Chapter four we also show how the maps developed in Chapter three may be used to determine the range of applicability of creep crack growth models. We also investigate the size of the damage zone, whether it is a material property or whether it is dependent on other parameters and determine its magnitude using critical strain accumulation as a criterion for void nucleation.

Chapter five contains an account of our experimental work in which we investigate the competition between creep and elastic effects in reaction bonded silicon nitride (RBSN). In this work notched RBSN specimens were creep tested at 1500°C. The notch geometries were designed to give known elastic stress concentrations and the behaviour of the specimens in 4-point bending was

compared with plane specimens having a cross-section a known fraction of the section of the notched specimens at the notch root. We examine how, with increasing stress, the specimen behaviour changes from, being controlled by creep effects to elastic effects dominating.
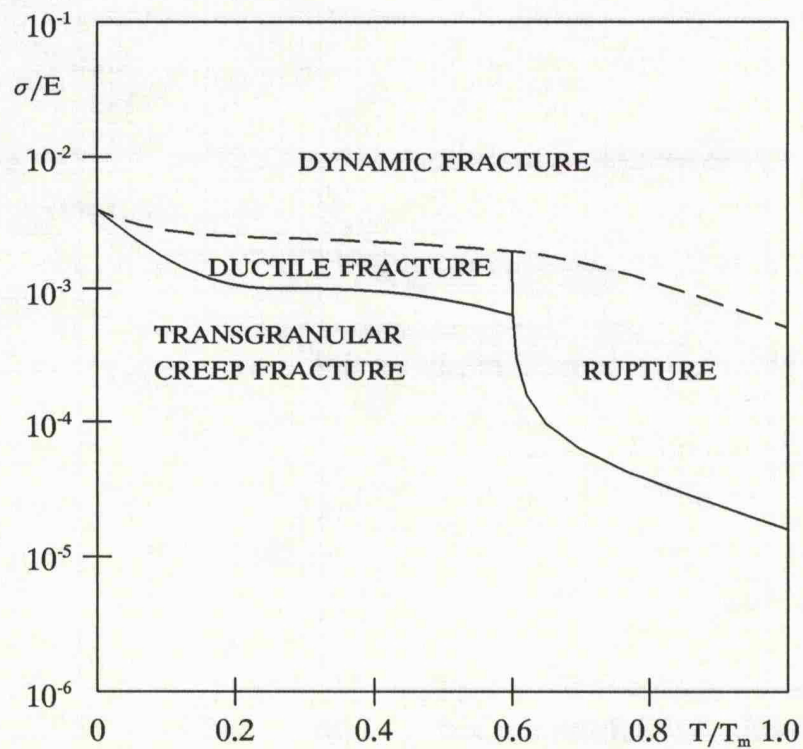
Figure 1.1a. A fracture mechanism map for high purity aluminium (after Ashby et. al.[36]).
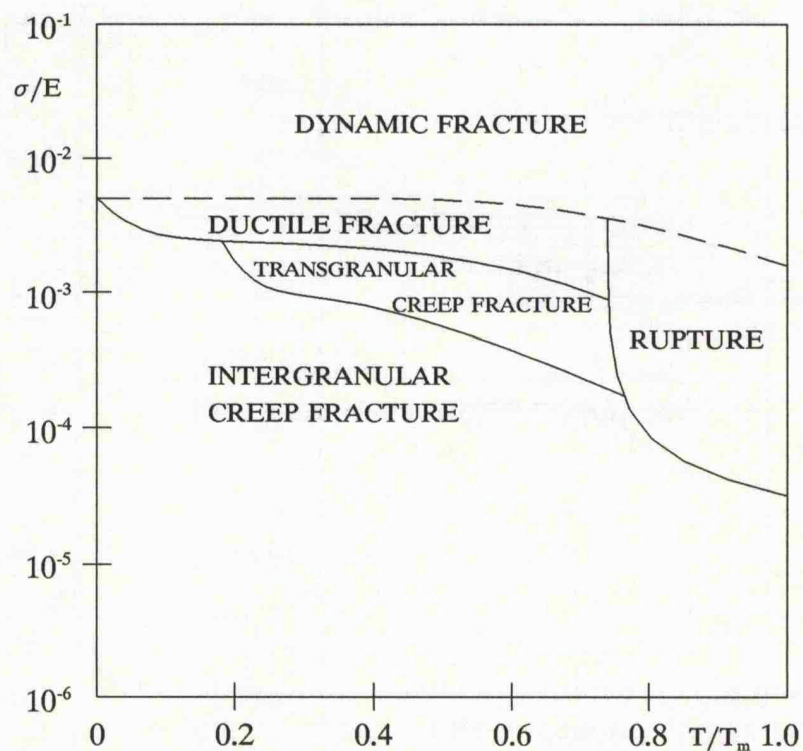

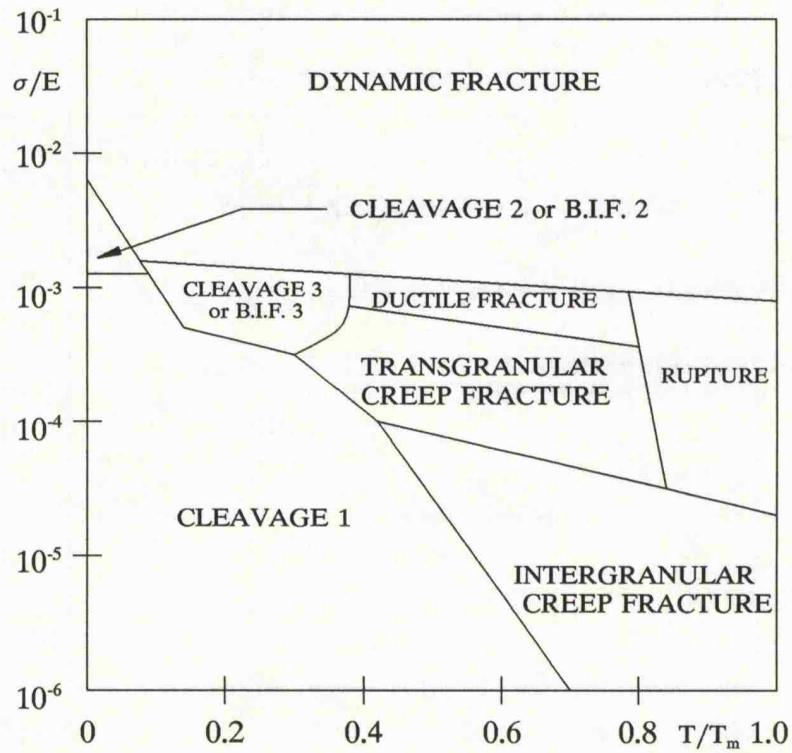**Figure 1.1b.** A fracture mechanism map for high purity silver (after Ashby et. al.[36]).

Figure 1.1c. A fracture mechanism map for chromium (after Gandhi and Ashby[37]).
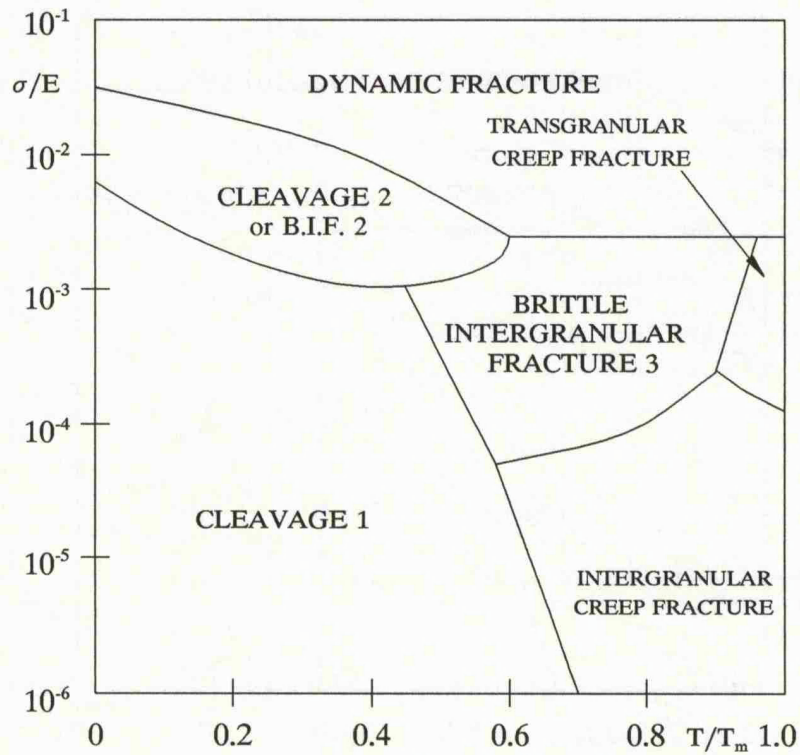
Figure 1.1d A fracture mechanism map for alumina (after Gandhi and Ashby[37]).
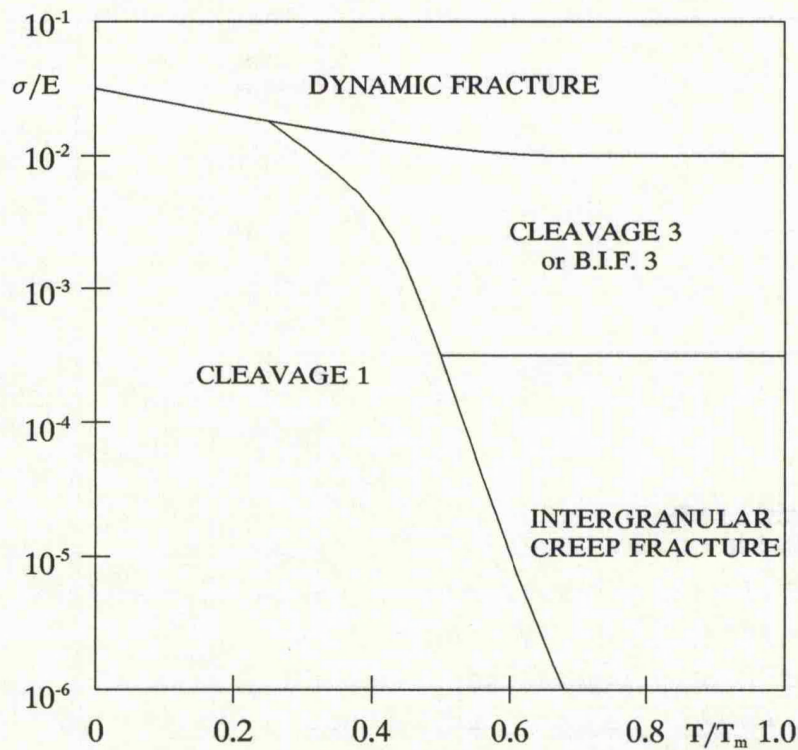
Figure 1.1e. A fracture mechanism map for hot pressed silicon nitride (after Gandhi and Ashby[37]).

Figures 1.1a-e. Fracture mechanism maps for a) high purity aluminium; b) high purity silver; c) chromium; d) alumina - Al_2O_3; e) hot pressed silicon nitride - Si_3N_4. Note the similarity between the maps for aluminium and silver, two fcc metals. Similar materials typically display qualitatively similar maps easily distinguishable from those of a different class of material. Maps for lead and copper are therefore of a similar type to maps a) and b). Map c) is a quite different but typical map for a b.c.c. refractory metal. Map d) is typical for a refractory oxide and map e) is typical for a covalent ceramic. "Cleavage 1" is the propagation of pre-existing cracks. "Cleavage 2" is the propagation of slip or twin induced cracks. "Cleavage 3" is the propagation by cleavage of cracks after appreciable plastic deformation. Brittle intergranular fracture (B.I.F.) occurs when the failure plane follows the grain boundary.

As the atomic bonding changes from metallic to covalent in maps a) to e) there is a change in behaviour away from ductile fracture towards cleavage being the dominant mechanism. In other words, within the portion of stress-temperature space represented by these maps there is a general shift to the right of the fields of dominance as the materials change from metallic to covalent.
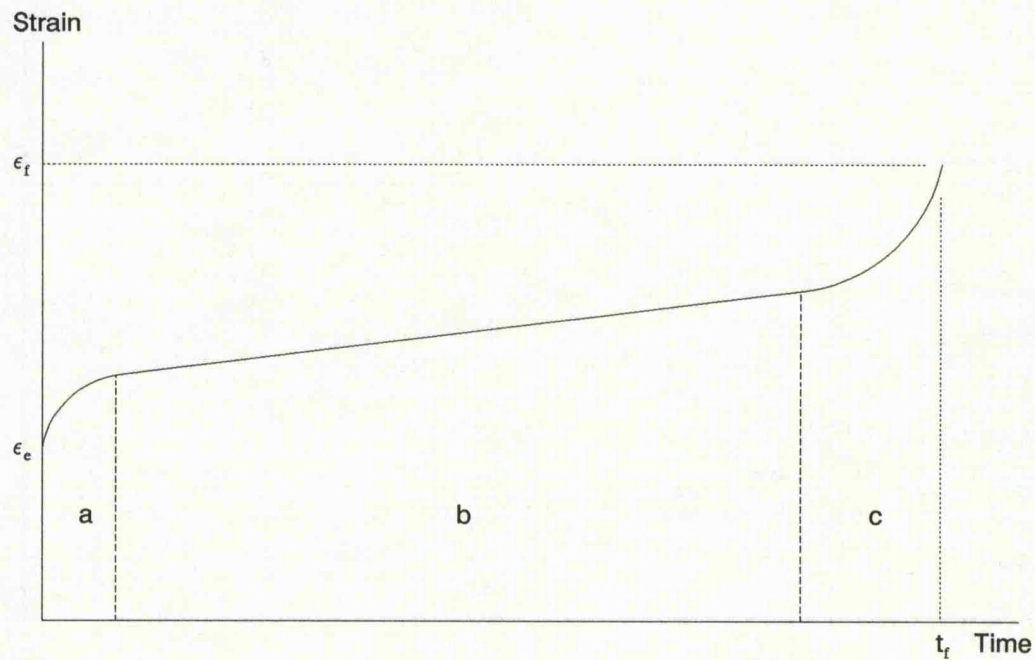
Figure 1.2. A schematic creep curve in which strain is plotted as a function of time. The curve shows the three regimes of primary, secondary and tertiary creep labelled a, b and c respectively. The instantaneous elastic strain, ϵ_e is shown, as are the strain and time to failure, ϵ_f and t_f. The slope of the curve in the secondary region is the steady state creep rate.

Mode I   Mode II   Mode III
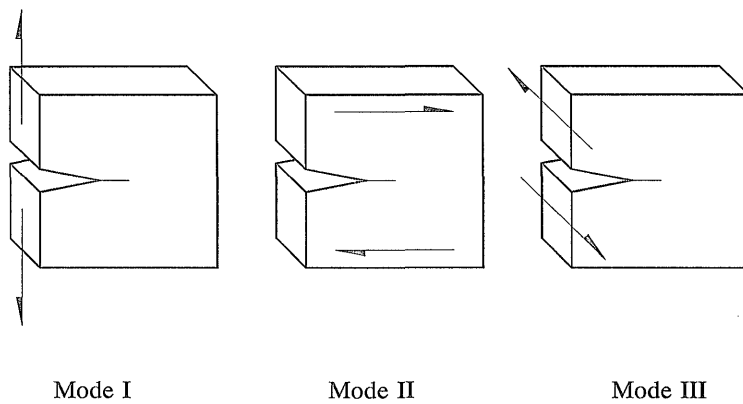
Figure 1.3. The three principal modes of notch loading; Mode I, in-plane tension; mode II, in-plane shear; mode III, anti-plane shear.
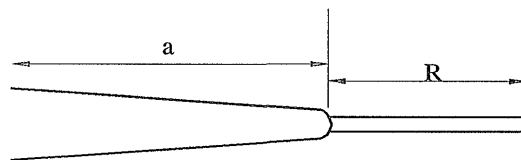
Figure 1.4. Dugdale's correction for limited plasticity ahead of the crack tip. A plastic zone of extent R is assumed ahead of the crack tip. The size of R is such that the elastic singularity vanishes at the crack tip and the crack behaves as though it is of length $a+R$. The stress field ahead of this larger 'crack' may then be approximately described by the equations of linear elastic fracture mechanics provided that $R \ll a$.
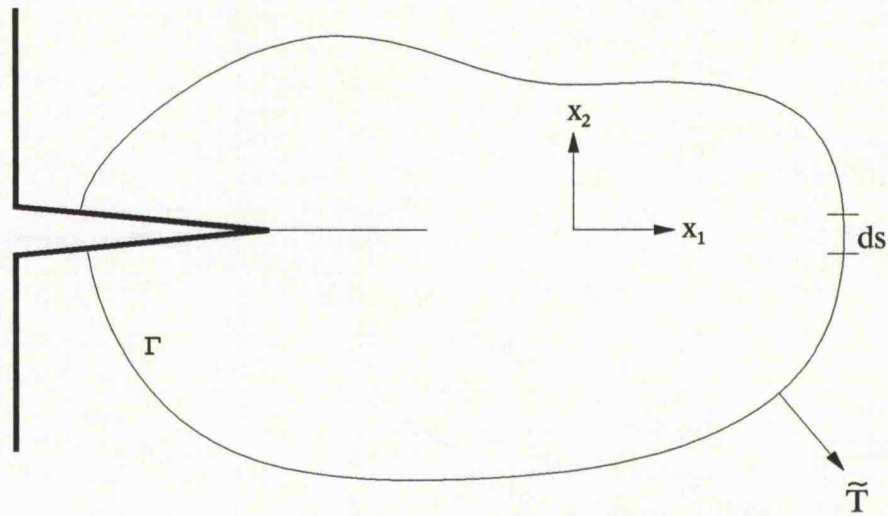
Figure 1.5. The magnitude of J (C*) is determined by integrating equation (1.13/1.16) around the contour Γ, of which ds is an element. $\tilde{T}$ is the traction vector acting on the contour and u (ù) is the displacement (displacement rate) in the direction of $\tilde{T}$. The body of the material is acted upon by a stress system σ_{ij} which results in a strain (strain rate) ϵ_{ij} ($\dot{\epsilon}_{ij}$).
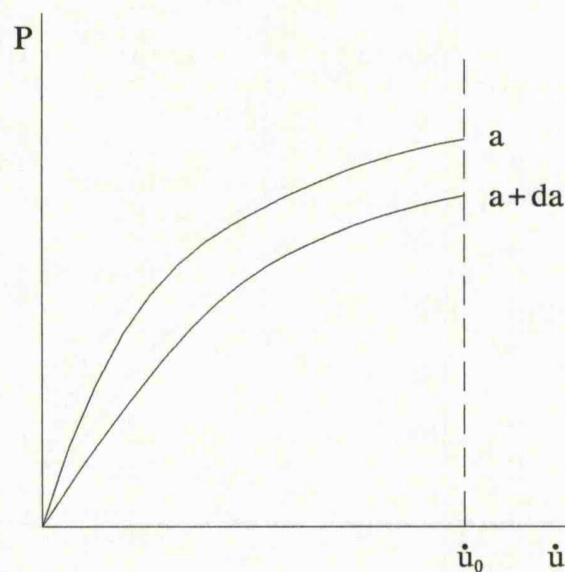
Figure 1.6. A schematic plot of load per unit thickness, P, as a function of displacement rate, ù, for two identical, non-linear, specimens containing cracks of length a and a+da. The area between the curves is the change in the energy release rate as the crack grows by an amount da.

CHAPTER TWO: CREEP FAILURE OF ENGINEERING MATERIALS

In this Chapter we present a review of the more significant work from the extensive body of literature on the creep failure of engineering materials, both by creep crack growth and as a result of continuum damage processes.

2.1   Failure by continuum processes.

At the turn of the century Phillips[1] reported that metal wires, glass and India rubber all developed a "slow stretch" over time when loaded at various temperatures. This work marked the beginning of the scientific interest in the phenomenon of creep. However, the first researcher to systematically study the creep of metals (and amongst other contributions introduce the terms 'primary', 'secondary' and 'tertiary' creep) was Andrade c.1910[38] and it was Andrade's work rather than the earlier work of Phillips which was largely responsible for stimulating the enormous amount of research that has been done on the creep of metals.

In the period between the wars there was a dramatic increase in the use of superheated steam in power plant and in 1929 at M.I.T., Norton[3], who was attempting to determine a threshold stress and temperature below which creep would not occur, discovered that a constant uniaxial stress, σ, will produce a constant secondary creep rate, $\dot{\varepsilon}$, given by the rule

$$\dot{\varepsilon} = A \, \sigma^n \qquad\qquad (2.1)$$

where A and n are material constants that depend on temperature only; a rule that became known as Norton's law.

Following Norton's work the theoretical and empirical investigation of creep proceeded apace and it became clear that far from being a relatively restricted, if interesting, phenomenon creep occurs in most solids if the temperature is

sufficiently high and is, at least partially, responsible for such large scale phenomena as the shape of the earths crust and glacial flow.

As a result of the extensive experimental work that was conducted on creep after the second world war, several empirical formulae were proposed to describe the creep behaviour of high temperature materials.

The Larson-Miller parameter.

The earliest of the widely used empirical relationships is due to Larson and Miller[39] who, in 1952, proposed the following relationship between the absolute test temperature, T, the stress, σ, and the time to failure, t_f.

$$P(\sigma) = \frac{(20 + \log t_f)T}{1000} \tag{2.2}$$

Where $P(\sigma)$ is the Larson-Miller parameter which is determined experimentally.

The Sherby-Dorn parameter.

Shortly after Larson and Miller, in 1954, Sherby, Orr and Dorn[40] assumed that t_f, T, and σ are related by

$$\theta(\sigma) = t_f e^{-Q/RT} \tag{2.3}$$

where R is the universal gas constant, Q is an experimentally determined activation energy and $\theta(\sigma)$ is the Sherby-Dorn parameter, again to be determined experimentally.

The Monkman-Grant rule.

As a result of their work on aluminium alloys, titanium alloys, austenitic and ferritic stainless steels and nickel alloys, Monkman and Grant[41] observed the unusual result that the product of the steady state strain rate and the time to failure is approximately constant and independent of the stress and temperature

$$\dot{\varepsilon} t_f \approx C_{MG} \qquad (2.4)$$

C_{MG} is the Monkman-Grant constant which typically lies in the range 0.03 to 0.3. This result is surprising, given the variety of possible high temperature failure mechanisms, and the number of different materials tested, however its validity has been confirmed by numerous workers for a wide range of materials and test conditions; see for example the review by Evans[42].

The continuum damage approach of Kachanov.

Kachanov[43] and Rabotnov[44] consider the evolution of a damage parameter, ω, which is in some way related to the degree of damage in the material. ω varies from 0 for uncavitated material to unity at rupture and is assumed to obey the kinetic law

$$\dot{\omega} = \frac{D \sigma^{\chi}}{(1+\phi)(1-\omega)^{\phi}} \qquad (2.5)$$

The damage parameter, though often associated with the area fraction, is not meant to be directly measurable in the way that f is, but influences the stress and strain rate according to

$$\dot{\varepsilon} = \frac{A \sigma^{n}}{(1-\omega)^{n}} \qquad (2.6)$$

If the stress is constant then equation (2.5) can be integrated to give the time to failure

$$t_f = \frac{1}{D \sigma^{\chi}} \qquad (2.7)$$

During steady state creep, which in classical theory is assumed to occur before cavitation has commenced, $\omega = 0$ and so equation (2.6) reduces to Norton's law, of

equation (2.1)

$$\dot{\epsilon} = A\sigma^n \qquad\qquad (2.8)$$

By multiplying equations (2.7) and (2.1) we can see that the Monkman-Grant product is given by

$$C_{MG} = \frac{A\sigma^{n-\chi}}{D} \qquad\qquad (2.9)$$

and is therefore only strictly constant when n = χ. In general χ < n but for most materials the difference is small, and allowing for experimental scatter C_{MG} can sensibly be assumed constant over a reasonable stress range.

The θ projection concept.

A much more recent empirical relationship is the θ projection concept of Evans, Parker and Wilshire[2]. The fundamental idea behind θ projection is that the steady state creep behaviour commonly reported for many materials is not a real phenomenon but a consequence of poor experimental technique or insensitive measurement. The proponents of θ projection argue, and there is some evidence to support this, that the more accurately measurements are made, the narrower the region is found to be over which the creep rate can sensibly be considered constant. θ projection assumes that nominally steady state behaviour is not steady at all but the result of competition between decaying primary and accelerating tertiary effects. The θ projection technique allows for this by considering the creep strain to vary with time according to

$$\epsilon = \theta_1\left(1 - e^{-\theta_2 t}\right) + \theta_3\left(e^{\theta_4 t} - 1\right) \qquad\qquad (2.10)$$

θ_1 and θ_2 determine the extent of the primary and tertiary stages with respect to strain while θ_3 and θ_4 characterise the curvatures of the primary and tertiary

elements respectively. The θ parameters themselves vary with stress and temperature according to

$$\ln \theta_i = a_i + b_i \sigma + c_i T + d_i \sigma T \qquad (2.11)$$

where a_i, b_i, c_i and d_i are constants (for i = 1 to 4). In practice the constants in equation (2.11) are evaluated from precise short-term constant stress data.

With a knowledge of these 16 parameters (a further 4 are required to include the effects of rupture) deformation behaviour can be accurately described. More significantly the authors claim θ projection allows results to be accurately predicted, including over very long times where data are scarce and expensive to obtain.

The creep behaviour of ceramic materials was not studied experimentally for the first half of this century as these materials' inherent brittleness and susceptibility to thermal shock lead most engineers to doubt their usefulness in high temperature applications. However while their resilience may be questionable the very high melting points of these materials cannot be denied, and as the need for alternative materials for high temperature components became more obvious the creep of ceramics began to be studied in the 1950's. However, unlike the study of metals, the beginning of the experimental work on ceramics is not marked by the work of one or two key individuals like Phillips or Andrade.

2.2   Failure by creep crack growth.

After several failures of power generating plant caused by the slow propagation and then catastrophic failure of creep cracks, the problem began to be discussed in the literature in the early 1970's[eg. 45].

The earliest paper that the author could find on the subject is a paper by

Siverns and Price[23] from 1970 who describe tests on a 2¼Cr1Mo steel which displayed a power law relationship between crack growth rate, $\dot{a}$, and the elastic stress intensity factor, K, of the form

$$\dot{a} = A K^n \qquad (2.12)$$

Where A and n were empirically determined constants. For this particular steel they reported a value of $n \approx 5.5$ which they describe as being similar to the Norton's law stress exponent for this material.

Elastic fracture mechanics started with the pioneering work of Griffith[26] in the 1920's who, by proposing that the strain energy released when a crack grew was equal to that needed to create its new surfaces, introduced the concept of fracture toughness. Following on from this work it was later demonstrated that in cracked brittle materials the asymptotic stress field at the crack tip is characterised by the elastic stress intensity factor K. In ductile materials this is not the case, the elastic stress, which is unbounded at the crack tip, exceeds the yield stress over a significant distance, the material deforms plastically and the crack tip field is no longer characterised by K. This problem had been recognised for some time and indeed plastic zone solutions (for example Dugdale's[29] strip model) had been found for it, when, in 1969, Rice[30] introduced his path independent integral J, described in Chapter one.

Soon after the publication of Rice's work on the J integral came the announcement of what is now considered a landmark result. Independently Hutchinson[46,47] and Rice and Rosengren[48] (collectively known as HRR) determined the asymptotic crack tip field for power law elastic materials which were characterised using the new J integral. For these materials, obeying the material

law $\epsilon = B_0\sigma^n$, the stress field valid as the distance, r, from the crack tip approaches zero, is

$$\sigma_{ij} = \left(\frac{J}{I_n B_0 r}\right)^{\frac{1}{n+1}} \tilde{\sigma}_{ij}(\theta) \qquad (2.13)$$

Where I_n is a function of n normalising the dimensionless function $\tilde{\sigma}_{ij}(\theta)$ such that the equivalent tensile stress, $\tilde{\sigma}_e(\theta)$, has a maximum value of 1; σ_e is defined by

$$\sigma_e = \sqrt{\frac{3}{2} S_{ij} S_{ij}} \qquad (2.14)$$

where S_{ij} is the stress deviator such that

$$S_{ij} = \sigma_{ij} - \frac{1}{3} \delta_{ij} \sigma_{kk} \qquad (2.15)$$

δ_{ij} is the unit tensor such that $\delta_{ij} = 1$ if $i = j$ and $\delta_{ij} = 0$ if $i \neq j$. For a graphical representation of how $\tilde{\sigma}_{ij}(\theta)$ varies with θ see, for example, Riedel's book[49].

In 1975, by studying the behaviour of a power law hardening centre cracked plate, Goldman and Hutchinson[50] demonstrated a theoretical relationship between the crack tip singularity, characterised by J, and the crack tip opening displacement (CTOD). Although their model is explicitly plastic in its behaviour, they showed that their results are also valid for power law creep relaxation, provided that elastic, primary and tertiary effects are ignored and that the crack is stationary. At the same time, Haigh[51] working on CrMoV steels demonstrated a relationship between the initiation of crack growth and the attainment of a critical CTOD.

At about the same time Landes and Begley[32] introduced a path independent integral for time dependent materials, the rate equivalent of the J integral, C^*. This allowed the HRR fields, which were initially determined for elastic materials,

to be extended to the time dependent regime; and in 1982 Ainsworth[52] extended the work of Goldman and Hutchinson[50], this time using C^* to characterise the material behaviour and neglecting elastic and plastic strains, to relate the initiation time to the CTOD, the results of his model comparing well with Haigh's original experiments.

In 1979 Riedel and Rice[53] demonstrated analytically that if elastic effects are ignored then the HRR stress field is the asymptotic stress field at a crack whether it is growing or stationary; but if elastic effects are significant and consequently cannot be ignored then the HRR field is an accurate description for a stationary crack only; a result that was to be verified numerically in 1981 by Bassani and McClintock[54] who obtained plane strain numerical solutions for the power law relaxation of crack tip stresses around a stationary crack which agreed very well with the predicted HRR field.

Later in 1979, Hui and Riedel[55] demonstrated that for a material with a creep exponent, n > 3, there is a region ahead of a *growing* crack where elastic and creep strains are equal. This results in a change in the nature of the asymptotic stress field ahead of the crack tip which has a singularity of the form $\sigma \propto r^{-1/(n-1)}$. This asymptotic field, known as the HR field (after Hui and Riedel), unlike the fields characterised by K or C^* is specified uniquely by the current crack growth rate. However, this new HR field was shown by Ainsworth[34] to only be valid over very small structural dimensions except when the growth rate is unrealistically high.

The groundwork for the next significant step in understanding creep crack growth was laid in the early 1960's when Anderson et. al.[56] pointed out that what they called a "reference stress" could be defined to describe the creep of simple structures such as beams. At the same time, but independently, Marriott and

Leckie[57] defined a "skeletal stress" at a specific point within a structure (the skeletal stress is in fact a reference stress but the term "skeletal" is no longer used).

The idea behind the reference stress technique is that the creep behaviour of a structure can be predicted from a single uniaxial test obviating the need for numerous tests at different stress levels, to determine the exact form of the constitutive law.

The reference stress, σ_0, for the general case, was demonstrated by Sim[58] to be given by the expression

$$\sigma_0 = \frac{P}{P_L} \sigma_y \qquad (2.16)$$

Where P is the applied load; P_L is the plastic limit load for the configuration and σ_y is the material yield stress at the relevant temperature. Note that a test at a different load results in a different reference stress.

Towards the end of the 1960s Leckie and Martin[59] derived bounds to the displacement of an elastic-creeping body subjected to a constant load, bounds which were later extended by Leckie and Ponter[60,61] to include the effects of plasticity; and which were further extended by Ponter[62] to account for variable loading.

Goodall and Cockroft[63] in the early 1970's demonstrated that an upper bound to the lifetime of an undamaged creeping structure could be calculated using a limit load technique. This work was extended by Goodall and Chubb[64] who showed that these concepts, developed for uncracked components, could be applied to damaged components provided that in these materials the creep damage can spread into the material without being dominated by crack tip behaviour. They further demonstrated that if this condition, which they termed "creep ductility" was fulfilled, the life of the component may then be determined using reference stress

techniques provided that the presence of the crack is allowed for in determining the limit load. They conclude "... further studies of the interaction of creep ductile and creep brittle situations are required in order to establish a criterion of when creep ductile behaviour is to be expected."

In 1975 in an early review of the literature on creep crack growth in metals, Haigh[65] concluded that correlation of the crack growth rate with the elastic stress concentration factor K "appears to have only limited application to creep crack growth". In 1977, Neate[66], working with specimens of a ½Cr½Mo¼V steel demonstrated that the crack growth rate could by correlated by the elastic stress intensity factor K, a result supporting the work, mentioned earlier, of Siverns and Price[23]. This correlation held quite well for a quenched form of the steel whose fully bainitic structure failed without significant ductility, but for a more ductile normalised and tempered steel of the same type this correlation did not hold. Neate however did find that the crack growth rates for this, and other[67], more ductile materials could be correlated by what he called an "equivalent stress". Although this equivalent stress is presented in a different way it is in fact identical to the reference stress defined in equation (2.16).

We can now see that by the end of the 1970s, we had progressed from Siverns and Price's[23] simple use of K to characterise creep behaviour to the point where, as well as K, techniques based on crack tip opening displacement, J, C* and reference stresses had all been proposed to describe the creep behaviour of cracks, all with some empirical evidence to support their validity but with, as yet, no satisfactory limits to their range of applicability. Ainsworth[34] took a big step towards establishing such limits when he demonstrated a range of values of growth rate over which K and C* describe the steady state growth of a crack. He showed

that the applicability of K appears to be very limited, only applying for low values of n (which is usually high) and rapid growth rates (again, not generally observed experimentally).

Provided that the creep displacement rate exceeds the elastic displacement rate (due to the changing stiffness of the component as a function of crack size) C^* is shown to have wide applicability and a simple formula for estimating it is presented

$$C^* = \sigma_0 \dot{\epsilon}_0 \chi \qquad (2.17)$$

Where again σ_0 is the reference stress given in equation (2.16); $\dot{\epsilon}_0$ is related to the reference stress by equation (2.1) and χ is a characteristic length for the specimen given by

$$\chi = \frac{K^2}{\sigma_0^2} \qquad (2.18)$$

Note that as K is proportional to σ_0, this means that the characteristic length χ is a function of specimen geometry only.

Ainsworth showed that in practice this means that C^* is a valid characterising parameter provided that growth rates are sufficiently slow that crack growth may be assumed not to influence the stress fields.

Ainsworth also demonstrated that reference stress techniques are appropriate for creep ductile materials when failure does not result from local damage at the crack tip but from general continuum damage. For such circumstances he derived a bound to the crack growth rate, above which a reference stress approach is inappropriate.

By the middle of the 1980's a fairly complete picture had emerged of the

behaviour of the asymptotic stress fields. The three discrete stress fields: the elastic ($\propto r^{-1/2}$); HRR ($\propto r^{-1/(n+1)}$) and the HR ($\propto r^{-1/(n-1)}$, $n > 3$) had all been shown to have their specific regions of dominance, but the overall form of the transient field was as yet unknown.

In 1981, Bassani and McClintock[68] had suggested a matching procedure by which the complete field could be approximated and the validity of this approach was verified in 1986 by Hawk and Bassani[69]. They demonstrated that the approximate solution obtained by the simple matching technique agreed very well with the results from a high resolution finite element model, the maximum error being about 13% for the worst case and usually significantly less than this.

Using this matching technique Hawk and Bassani were able to develop a picture of the complex evolution of the crack tip fields, which can be described as follows for constant crack values of growth rate and K. At time t = 0 the solution is straightforward; the elastic parameter K characterises the field everywhere in the body. A small time later the HR field has developed embedded within the HRR field which is in turn surrounded by elastic material. As time increases the region of dominance of the HR field "grows" into the material as does that of the HRR field. As a consequence of their relative singularities the zone of dominance of the HR field grows more rapidly than that of the HRR field until at the long time limit the HRR field has disappeared and the asymptotic fields comprise the HR field embedded directly in the K field. The relative singularities and regions of dominance of the various components of the full transient field are shown in Figure 2.1 for a material with n=4. In order to develop this model Hawk and Bassani chose suitable parameters to produce the limiting case of the HR field growing faster than the HRR field. This ensured that K would always characterise the

stresses in the far field. If the opposite were the case, that the HRR field grows faster than the HR field, then the steady state would be the HR field embedded in the HRR field characterised by C*. This is the other limiting case considered by Ainsworth, mentioned earlier.

The effects of primary and tertiary creep continued to be ignored in the stress analysis of a cracked body until Riedel[70] extended his earlier work on C* to include the effects of strain hardening. He presented a generalised form of C*, which he called C_h^* (the subscript h signifying hardening), and used this to determine transition times for the changeover from small scale to extensive creep; from initial plasticity to extensive creep and from primary creep of the whole specimen to steady state creep of the whole specimen.

The creep growth of an isolated crack by direct diffusion of material from the crack tip has been analysed in detail by Chuang[71] but this model is of limited relevance as examination of failure surfaces of numerous materials, both metallic and ceramic, indicates that crack growth in crystalline materials is due to the nucleation, growth and coalescence of damage ahead of the crack tip.

Creep crack growth where the mechanism causing growth is restricted to a process zone ahead of the crack tip began to be modelled by several authors in the early 1980's. Nikbin and Webster[72], as well as others[eg. 73], assumed that all the damage is contained within the process zone ahead of the crack tip which grows into the material with a constant velocity. Failure of the undamaged ligament occurs at the crack tip and in this way the crack grows into the material.

From a consideration of the increase in damage at a point as it effectively moves towards the crack tip the crack growth rate can be determined. A model of this form originally due to Cocks and Ashby[73] was extended by Nikbin, Smith and

Webster[74] to predict the crack growth rate from uniaxial creep data and the grain size.

Wilkinson and Vitek[75] modelled crack growth under the influence of the asymptotic stress fields in 1982. They treated the stress fields and the damaging process as decoupled phenomena. This is obviously an approximation but their result does give an upper bound to the crack growth rate.

In most analyses the transitional phase of crack growth during which the steady state is achieved had been ignored, the steady state being assumed. In a further paper, Ainsworth[76] has demonstrated that this is a valid assumption for creep ductile materials but that in creep brittle materials the additional strain accumulated during transition can be a significant proportion of, or even exceed, the material's creep ductility.

Riedel and Rice[53] had earlier demonstrated that C* only characterises the stationary state fields which apply at long times after loading. They showed that the short to medium term transient fields were still of the HRR form but were characterised by a time dependent parameter greater than C*, C(t) and they established its short term plane strain magnitude

$$C(t) \approx \frac{K^2 (1 - v^2)}{(n + 1) E t} \tag{2.19}$$

Where the term $(1-v^2)$ is deleted for plane stress. Ainsworth[76] extended this work to describe a means of estimating C(t) during the transition

$$C(t) = C^* \left[\frac{(1 + EC^* t / K^2)^{n+1}}{(1 + EC^* t / K^2)^{n+1} - 1} \right] \tag{2.20}$$

This result satisfies the short term limit of equation (2.19) and we can see that in the long term limit, as $t \to \infty$

$$C(t) \to C^* \qquad\qquad (2.21)$$

This result is an approximation but still demonstrates that at short times $C(t) \gg C^*$, which emphasises the importance of the transition phase of growth. In the same paper Ainsworth goes on to present a simple reference stress technique for determining the creep strain during the transition. This is a significant result because Webster[77] has argued that creep strains need only equal elastic strains for complete stress redistribution ahead of a crack, which would then be characterised by C^*. In this situation, he argues, even creep brittle materials may be expected to be characterised by C^* unless creep strains less than the elastic strains are accumulated during the transition. Bearing in mind Ainsworth's observation, noted above, that $C(t) \gg C^*$ during the transition, this would appear an unlikely situation.

In a more recent paper Ainsworth and Budden[78] have developed a different procedure for estimating $C(t)$. In this technique J is used to correlate crack tip and far field behaviour and the validity of the method is demonstrated with a finite element model. In a companion paper[79] the same authors demonstrate that their new approximate technique for determining $C(t)$ may be used to determine crack growth rates.

In all of the analyses described above the material is assumed to deform by power law creep. However, it has been noted for some time that at high stresses "power law breakdown" occurs in some materials when Norton's law no longer describes the material behaviour. A hyperbolic-sine law has been proposed[eg. 80] which reduces to Norton's law at low stresses and at high stresses to an exponential law which more accurately describes real behaviour at these stress levels.

$$\dot{e} \propto [\sinh(\sigma/\sigma_0)]^n \qquad (2.22)$$

Bassani[81] has analysed the behaviour of an antiplane shear (mode III) stationary crack in a material that behaves both elastically and according to equation (2.22). He demonstrates that as a consequence of the hyperbolic behaviour the crack tip stress singularity is weaker than for a purely power law material whereas the strain singularity is stronger. Bassani goes on to prove that the behaviour of these materials is similar to that of power law materials with a similar transition from elastic behaviour (this time characterised by K_{III}) to C^* control with extensive creep throughout the specimen. Although this work is of interest in that it helps to fill a gap in establishing a complete picture of material behaviour it is likely to be of limited practical use as components are not usually designed to operate in the "power law breakdown" regime. Having said that, in a cracked body the stresses close to the crack tip may be high enough for localised material deformation to be governed by equation (2.22). The reference stress technique, however, can account for this because equation (2.17) is entirely general, the reference stress and strain rate may be related through any constitutive law or indeed be determined experimentally.

Creep crack growth in specifically ceramic materials has been modelled by Thouless et. al.[35]. In this work the constraint on the damage zone exerted by the surrounding undamaged material (which is assumed linear viscous) is modelled by positioning an imaginary array of dislocations ahead and in the plane of the crack. The individual displacement of each discrete grain in the damage zone is determined using a standard result from dislocation mechanics. This model predicts a crack growth rate that is proportional to the elastic stress concentration K and

inversely proportional to the material viscosity η.

Having established the constraint it is then shown to have negligible effect on the crack growth rate except for certain specific cases such as the process zone being confined to a very small region; the specific case of a damage zone of length one grain is considered.

Use of the elastic parameter K to characterise the behaviour would appear, based on what has been said above, to indicate a model with very limited applicability. However for the specific case of linear behaviour K and C^* are related to each other through the material viscosity, η, as described in equation (1.19)

$$K^2 = 3\eta C^* \qquad (2.23)$$

so where Thouless et. al. use K to describe the behaviour they are in effect using C^*.

In developing this crack growth model it is assumed that both the sintering stress and the void's internal pressure are small compared with the stress acting on the damage zone, and may be neglected. Both these assumptions can be justified, or at least have limits prescribed to them within which they are valid, in fact Thouless goes on to consider the effect of the sintering stress. However his initial statement that this model describes the behaviour of linearly viscous "i.e. ceramic" materials is somewhat misleading. In the first place ceramics generally do not display linear behaviour, Govila[82] for example, has tested hot pressed Si_3N_4 with a steady state strain rate proportional to stress to the power 5.25 and such values are not uncommon. Elsewhere[83] Thouless states that for ceramics "the assumption of linear creep is generally a good one" without substantiating this claim. His

argument would appear to be that if the two limiting cases for describing the material behaviour are n = 1 (analogous to linear viscosity) and n = infinity (analogous to plasticity) then a material with n = 4 (say) is obviously much closer to the linear limit than the plastic limit. However Goodall and Cockroft[63] have demonstrated, by considering a variety of generalised problems, that material behaviour in the creep range is better described by the values of $1/n$ rather than n itself. From this we can easily see that a creep exponent of n = 2 falls halfway between the possible values for $1/n$ of zero and unity and that it is difficult, therefore, to justify modelling materials for which n is greater than 2 as linear.

Not withstanding this criticism, Thouless' model does provide a full and detailed description of the specific case of linear creep and is used in Chapter four of this thesis as a reference model for comparison with a more general model which we derive there.

Many ceramics contain an amorphous phase, often deriving from sintering aids. The creep behaviour of this second phase, which normally exists on two grain boundaries and at triple points, usually controls the behaviour of the component as by definition sintering aids have lower melting points than the bulk material. Also cracks can initiate more easily in second phase material and at lower stresses than they can in the matrix material. Thouless[84] has also modelled crack growth in liquid phase sintered materials which he describes by two limiting solutions. In one the damage zone is small and behaviour is governed by the constraint of the matrix. In the other the growth rate is independent of the viscosity of the matrix depending only on the second phase behaviour.

This model is extended in a further paper[85] in which Thouless suggests that the actual crack velocity in these materials is the lower of the two velocities derived

by considering the limiting cases described above. Again no satisfactory attempt is made to justify the assumption of linear behaviour in these materials.
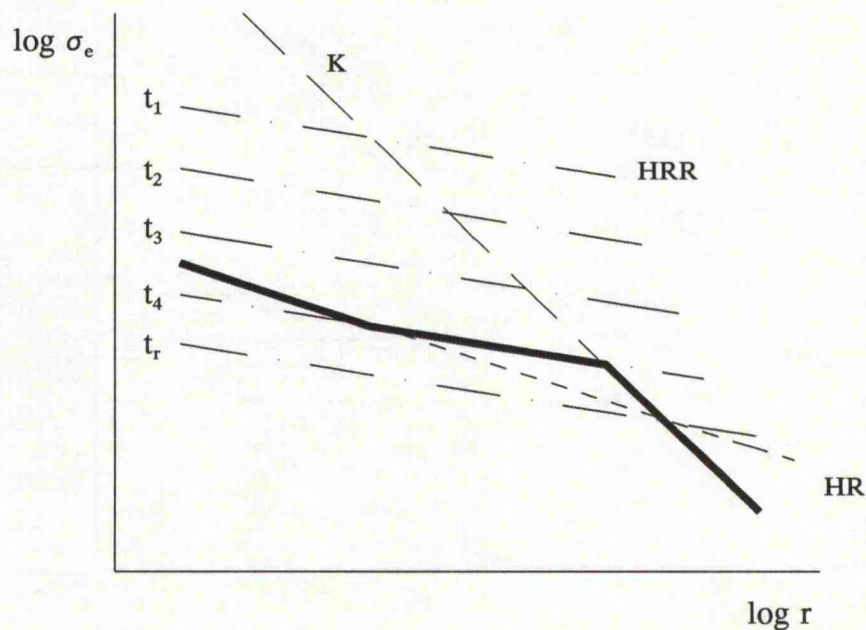
Figure 2.1. A schematic log-log plot of the effective stress, at time t_4 as a function of distance from the crack tip (after Hawk and Bassani[69]). The plot shows the elastic K field (dashed), the HRR field (chained), the HR field (short dashed) and the full transient field (thick solid). The material considered has a creep exponent, n = 4, and so the singularities of the fields are respectively $-\frac{1}{2}$, $-1/5$ and $-\frac{1}{3}$. The transient HRR field is characterised by the time dependent parameter C(t) and as the time increases from t_1 the magnitude of the HRR field decreases until at time t_r it disappears completely.

CHAPTER THREE: CREEP CRACK GROWTH MAPS

3.1   Introduction.

In this Chapter we will consider the different conditions under which either the elastic stress intensity factor, K, or the rate equivalent of the path independent integral, C*, characterise the response of a cracked component. We will present a series of simple maps, with axes of normalised stress and normalised crack growth rate on which the regions of dominance of K and C* can be clearly seen. Material test data can be plotted directly onto these maps; from which we can see whether, under the conditions used to produce the data, C* or K characterised the material's behaviour. Theoretical models can also be plotted on the maps to determine for example the crack growth rate below which a model predicting K control would be invalid.

Riedel[49] has developed an analogous series of maps, in stress-time space, which he refers to as load parameter maps, on which are plotted regions of dominance of the characterising parameters K, C*, J and C_h^* (which was described in Chapter 2). A typical Riedel type map is presented in Figure 3.1. Riedel's maps were developed from a model in which the primary creep of a stationary crack is modelled as power law strain-hardening. In this model constitutive relations are developed for extensive primary creep, the growth of a primary creep zone in an otherwise elastic body and the growth of a steady state creep zone within a zone of primary creep. The demarcation lines on the map are the characteristic times as a function of the applied stress for the transition from one dominant characterising parameter to another.

The advantage of the maps that will be presented here, compared with the Riedel type map, has already been alluded to; namely that Riedel's work is based

on a consideration of the development of the stress fields ahead of a stationary crack. The maps presented here are developed from a consideration of the fields ahead of a *growing* crack assuming steady state conditions. However, this is not to say that the Riedel type map is not useful; based as it is on a consideration of a stationary crack it is an appropriate device for determining the characterising parameter for the process of crack initiation.

3.2   Crack tip stress fields.

We will start by considering the stress fields which develop with time ahead of a growing crack in a material which creeps according to the material law

$$\dot{e}_{ij} = \frac{1+\nu}{E} \dot{S}_{ij} - \delta_{ij} \frac{1-2\nu}{3E} \dot{\sigma}_{kk} + \frac{3}{2} A \sigma_e^{n-1} S_{ij} \qquad (3.1)$$

Here, ν is Poissons ratio, E is Young's modulus and the summation rule for repeated indices implies that $\sigma_{kk} = \sigma_{11} + \sigma_{22} + \sigma_{33}$; S_{ij} is the stress deviator, defined in equation (2.15) and a superscripted dot denotes the first differential with respect to time; σ_e is the equivalent tensile stress which was defined in equation (2.14).

If an (initially) stationary crack within a creeping body is subject to rapid mode one loading the instantaneous response of the material is elastic and the stress field ahead of the crack is characterised by the mode one stress intensity factor, K_I.

The stress at a point a distance r from the crack tip is then given by

$$\sigma_{ij} = \frac{K_I}{\sqrt{2\pi r}} f_{ij}(\theta) \qquad (3.2)$$

where $f_{ij}(\theta)$ is a dimensionless function of the angle, θ, between the point under consideration and a line in the plane of the crack normal to the crack front. The stresses ahead of the crack will then redistribute with time until eventually creep

effects dominate and a steady state is reached in which the stress state can be described entirely in terms of the creep response of the material.

Hutchinson[46,47] and Rice and Rosengren[48] have analysed the crack-tip fields in power law materials. Neglecting elastic effects they found that the stress field ahead of the crack tip varies with r according to

$$\sigma_{ij} = \left(\frac{\sigma_0^n C^*}{\dot{\epsilon}_0 I_n r} \right)^{\frac{1}{n+1}} \tilde{\sigma}_{ij}(\theta) \tag{3.3}$$

where C^* is given by equation (1.16), and σ_0 is the reference stress, defined in equation (2.16) and related to $\dot{\epsilon}_0$ by equation (1.2). I_n is a dimensionless function of n chosen so that $\tilde{\sigma}_{ij}(\theta)$ has a maximum value of unity when $\theta = 0$ and is well approximated by

$$I_n = \frac{n+1}{n} \pi \tag{3.4}$$

The stress field described by equation (3.3) is the well known HRR field and provided that elastic effects are neglected it is valid whether the crack is growing or is stationary[53].

For a growing crack, Hui and Riedel[55] have demonstrated that if the creep exponent, n > 3, there will be a region ahead of the crack tip in which creep strains and elastic strains are of the same order. This causes a change in the nature of the crack tip fields within this region.

If we now consider a one-dimensional Dugdale type damage zone, the stress field within the zone is given approximately by

$$\sigma = \left(\frac{1}{n-1} \right)^{\frac{1}{n-1}} \left(\frac{\sigma_0^n \dot{a}}{\dot{\epsilon}_0 E r} \right)^{\frac{1}{n-1}} \tag{3.5}$$

(A proof of the validity of this approximation is given in Appendix 1). This stress field is known as the HR field and has the property that, unlike the K and C* controlled fields, it and its associated strain rate field are completely independent of the applied loading or of the load history, being characterised solely by the current crack growth rate and material properties.

Consider now a cracked creeping body, of a material with a stress exponent, n, greater than 3. If a mode one load is applied to the crack at time t = 0 then the initial stress field is purely elastic as there has been no time for creep to occur, therefore the stress field ahead of the crack is described by equation (3.2). A short time later, when the specimen begins to creep, the stress field ahead of the crack has the singularity of the HRR field, but is of a greater magnitude, and is characterised not by C* but by the time dependent parameter C(t). Riedel and Rice[53], by determining a characteristic time for the transition from small scale to extensive creep have demonstrated that C(t) has the short term plane strain value

$$C(t) = \frac{K_I^2 (1-\nu^2)}{E(n+1)t} \qquad (3.6)$$

while for plane stress the term $(1-\nu^2)$ should be deleted.

Assume now that the crack starts to grow. If the crack growth rate is slow at first it can be seen that the steady state comprises the HR field close to the crack tip with creep effects dominant everywhere else in the specimen and a remote stress field of the HRR form, this is illustrated in Figure 3.2a. The extent of the zone in which elastic effects are important, r_e, can be determined by equating equations (3.3) and (3.5) and substituting r_e for r

$$\left(\frac{\sigma_0^n C^*}{\dot{e}_0 I_n r_e}\right)^{\frac{1}{n+1}} = \left(\frac{1}{n-1}\right)^{\frac{1}{n-1}} \left(\frac{\sigma_0^n \dot{a}}{\dot{e} E r_e}\right)^{\frac{1}{n-1}} \tag{3.7}$$

Recalling from Chapter two that Ainsworth[34] has shown for the general case that C* may be well approximated by

$$C^* = \sigma_0 \dot{e}_0 \chi \tag{3.8}$$

and from equation (2.18) that $\quad K = \sigma_0 \sqrt{\chi} \tag{3.9}$

we find that

$$\frac{r_e}{\chi} = \frac{n}{(n+1)\pi} \left(\frac{(n+1)\pi}{n(n-1)} \frac{\sigma_0}{E} \frac{\dot{a}}{\dot{e}_0 \chi}\right)^{\frac{n+1}{2}} \tag{3.10}$$

If the crack grows more rapidly there may be insufficient time for the time dependent HRR field to form and the steady state therefore comprises a small region where the stress field is of the HR type, surrounded by non creeping elastic material. This is illustrated in Figure 3.2b. The extent of this HR zone r_c can be obtained by equating equations (3.2) and (3.5)

$$\frac{K}{\sqrt{2\pi r_c}} = \left(\frac{\sigma_0^n C^*}{\dot{e}_0 I_n r_c}\right)^{\frac{1}{n+1}} \tag{3.11}$$

Making the substitutions of equations (3.8) and (3.9) again, we find that

$$\frac{r_c}{\chi} = \frac{1}{2\pi} \left(\frac{n-1}{2\pi} \frac{E}{\sigma_0} \frac{\dot{e}_0 \chi}{\dot{a}}\right)^{\frac{2}{n-3}} \tag{3.12}$$

This is effectively the size of the zone within which creep effects are important in an otherwise elastic material and it can be seen from the above expression that the

size of this zone decreases as the crack growth rate increases.

The transition from C* to K control in the far field can be determined by simply equating equations (3.10) and (3.12) ie.

$$\frac{\sigma_0 \dot{a}}{E \dot{\epsilon}_0 \chi} = f(n) \tag{3.13}$$

where
$$f(n) \approx \frac{n+1}{n-1} \tag{3.14}$$

for n > 3.

It is important to note that in the above expressions the load applied to the component is described in terms of the reference stress, σ_0, and that all stresses are normalised with respect to this parameter. Likewise all rates are normalised by the reference strain rate, $\dot{\epsilon}_0$, and all terms with the dimension of length are normalised using the characteristic length for the specimen geometry, χ.

The above results have been derived from a simplified model of the way in which real materials behave. The derivation of the HRR field requires a mathematically sharp crack, whereas in reality before a crack can start to grow its tip will be blunted by creep flow of the surrounding material. Blunting attenuates the HRR field over a distance which is proportional to the crack tip opening displacement, δ_t[86]. Outside this region the HRR field is still an accurate approximation. The HRR field is therefore only valid outside a region which is itself large compared with the crack tip opening displacement; so at one extreme the validity of the HRR field is limited by blunting and at the other extreme by specimen geometry. This means that the specimen must be of a sufficient size if a valid HRR field is to be able to form. The accuracy of the K field, on the other hand, is also affected by crack blunting at the small scale, but even in a perfect

specimen equation (3.2), which is in fact the first term in a series, is only valid close to the crack tip, with higher order terms becoming increasingly important with increasing r. Thus talk of C^* or K dominating in the far field is not strictly correct, though it is terminology that is often used.

So far the mechanism of crack growth has itself been ignored. Microscopic examination of creep crack failure surfaces often reveals that this process involves the formation, growth and linkage of damage, producing a single dominant crack which grows into the material. This damage ahead of the crack tip can affect both the short term elastic and long term creep behaviour of the material within the damage zone. However if this zone is small we can characterise the crack growth process either in terms of C^* or K depending on the relative size of the damage zone compared with either r_e or r_c. If the damage zone is larger than r_e then the elastic effects, which are only important for $r < r_e$ are swamped by the effects of the damage process and the growth process is therefore controlled by C^*. If, however, the damage zone is larger than r_c then it is the *creep* effects which are swamped by the effects of the damaging process and the growth process is K controlled.

Obviously it is not possible, without either examining the component or additional modelling, to know the extent of the damage zone and thus whether the above requirements are met. It was mentioned in Chapter one, that in the linear elastic case, the equations of elastic fracture mechanics may still be used to describe the stress field ahead of a crack where limited plasticity is present provided that the small scale yielding criterion, $R \ll a$, is met. If R no longer represents the extent of the plastic zone, but now is taken as the extent of the damage (or process) zone then $R \ll a$ is the small scale damage criterion. Provided that this criterion is met, the elastic and creep effects in the HR zone will not be swamped by the effects of

the damaging process. Although the precise magnitude of the small scale damage criterion varies with geometry it can be taken as approximately[87]

$$R/a = 0.05 \tag{3.15}$$

Now from a comparison of equations (1.9) and (3.9) we can see that the characteristic length, χ, is approximately equal to πa (the term f (a/w) being approximately equal to unity if the specimen is large compared with the crack). Therefore if we make the approximation that $20\pi = 50$, we see that the above requirements are met if $r_c/\chi < 0.02$ for K controlled growth and if $r_c/\chi < 0.02$ for C^* controlled growth. This approximation is admittedly crude, however, it will be seen that the results are relatively insensitive to the exact value, particularly for the case of creep control.

From equation (3.12) we can readily see that creep crack growth is K controlled if

$$\frac{\dot{a}}{\dot{e}_0 \chi} > \frac{g_1(n)}{\sigma_0/E} \tag{3.16}$$

where

$$g_1(n) = \frac{(n-1)}{50} \left(\frac{25}{\pi}\right)^{\frac{n-1}{2}} \tag{3.17}$$

similarly from equation (3.10) it is apparent that creep crack growth is creep controlled if

$$\frac{\dot{a}}{\dot{e}_0 \chi} < \frac{g_2(n)}{\sigma_0/E} \tag{3.18}$$

where
$$g_2(n) = \frac{(n-1)}{50^{\frac{2}{n+1}}} \left(\frac{n+1}{n} \pi \right)^{\frac{n-1}{n+1}} \qquad (3.19)$$

If inequalities (3.16) and (3.18) are plotted on log-log axes the result is a map of the type shown in Figure 3.3 on which we can identify four separate regions, one representing C^* controlled creep crack growth, another where creep crack growth is K controlled and a third region between the other two where growth is in transition and is neither controlled by C^* or K.

3.3   Continuum failure.

We may also identify a fourth region on the map of Figure 3.3 where instead of failure by the growth of a dominant crack the component fails as a result of the accumulation of continuum damage.

Suppose we wish to determine a value, ξ, of $\dot{a}/\dot{\varepsilon}_0\chi$ on the boundary between failure as a result of the accumulation of continuum damage and failure as a result of C^* controlled creep crack growth, ie.

$$\frac{\dot{a}}{\dot{\varepsilon}_0\chi} = \xi \qquad (3.20)$$

recalling that $\chi \approx \pi a$, and integrating, we obtain

$$\int_0^{t_f} \dot{\varepsilon}_0 \, dt = \frac{\ln(a_c/a_i)}{\pi \xi} \qquad (3.21)$$

Where a_c is the maximum crack size that the component can withstand and a_i is the initial crack size. Now, if the integral on the left hand side of equation (3.21) is less than the Monkman Grant product[41], C_{MG}, described in Section 2.1, the failure will be, by definition, not a continuum failure as the Monkman Grant relationship is specifically only valid for continuum failures. From this it follows that for

continuum failure

$$\xi \le \frac{\ln(a_c/a_i)}{\pi \, C_{MG}} \qquad (3.22)$$

Which, from the typical range of values of C_{MG} given in Chapter 2 and from the insensitivity of the result to the ratio a_c/a_i, we can see would fall within the approximate range $1 \le \xi \le 100$.

3.4   Presentation of material data.

Material data can easily be plotted on this map. Nikbin et. al.[74] have compiled creep data for a variety of low alloy steels, 304 stainless steel and the aluminium alloy RR58, data for nimonic 80A are given by Riedel[49], and data for alumina are given by Blumenthal and Evans[88].

In order to use the map we need first to determine the characteristic length, χ, for the specimen being tested. Equation (2.18) defined χ as

$$\chi = \frac{K^2}{\sigma_0^2} \qquad (3.23)$$

and the reference stress, σ_0, was defined in equation (2.16) as

$$\sigma_0 = \frac{P}{P_L} \, \sigma_y \qquad (3.24)$$

where P is the applied load, P_L is the limit load for the specimen and σ_y is the yield stress of the material at the test temperature. Note that, as K is proportional to P it follows that χ is only a function of specimen geometry, ie. it is independent of P. Values of χ and of the limit loads for common specimen types, and how they vary with geometry are presented in Appendix 2. By referring back to the original papers from which the above mentioned data were obtained, the type of specimens

used and their dimensions, as well as the measured creep crack growth rates can be obtained. From this, following the method described in Appendix 2, the characteristic length can be obtained. The positions of the test data are shown in Figures 3.4 to 3.9. The function $g_1(n)$ is very sensitive to the exact value of n, displaying a variation of ~13 orders of magnitude with a variation of n from 8 → 35, such that data from materials with different values on n should be plotted on separate maps.

304 stainless and 2¼CrMo steels.

The data for these steels, which have creep indices of 8 and 9 respectively, are shown in Figures 3.4 and 3.5. Both of these steels are very ductile with the stainless steel showing a strain at failure, ϵ_f, of 0.4 and the 2¼CrMo having an ϵ_f value of 0.45. With materials as ductile as these one would require very large specimens to achieve plane strain conditions at the crack tip; indeed Nikbin et. al.[74] demonstrate that conditions of plane stress prevailed in these tests. As expected therefore, from such creep ductile materials, creep crack growth was characterised by C^* rather than by K, even for the highest crack growth rates. This conclusion is in agreement with the observations of Nikbin et. al. who show that there is indeed a good correlation between crack growth rate and C^*. By plotting on the maps the boundary to the region of continuum damage, described by equation (3.22), we can see that if C_{MG} is at the low end of its observed range though creep crack growth may still occur this will not be the life controlling factor. Failure will eventually result from continuum damage.

1CrMoV and ½Cr½Mo¼V steels.

Data for these steels, which have creep indices of 14 and 17 respectively, are shown in Figure 3.6 and 3.7. These steels are less ductile than the previous two

materials (much less so in the case of the ½Cr½Mo¼V steel) but creep in the majority of the specimens is still characterised by C*, though a low value of C_{MG} would lead one to expect some continuum damage. Nikbin et. al. demonstrate that for these materials neither plane stress nor plane strain conditions prevailed at the crack tip. Now our analysis is essentially one dimensional and is therefore strictly applicable only in conditions of plane stress. However a plane strain crack grows more rapidly than a plane stress crack for the same value of C* so plotting data closer to the plane strain limit (data at the right of the boxes on Figures 3.6 and 3.7) on our plane stress map is conservative with respect to determining the correlating parameter.

RR58.

Data for this aluminium alloy, which has a creep exponent of 35, are plotted in Figure 3.8. This alloy is much less ductile than all of the materials discussed earlier, other than the ½Cr½Mo¼V steel, showing a strain at failure of 0.05. Nikbin et. al. demonstrate that conditions at the crack tip in the tests represented by Figure 3.8 were very close to plane strain for which our map, as mentioned above, is not strictly valid (in fact, as the same dimensional groups apply in both plane stress and plane strain analyses, and the map is plotted on log-log axes the boundaries are not likely to move by very much anyway). Plotting this plane strain data on our map (the broken box in Figure 3.8) shows that we would not expect a reasonable correlation between å and C* and yet Nikbin shows that such a correlation does exist. In the case of the 1CrMoV and ½Cr½Mo¼V steels it was enough simply to note that the position of the plane strain data was conservative and that growth was definitely C* controlled, however in this instance this is not satisfactory.

Recall that the characteristic length, χ, was given by

$$\chi = \alpha \frac{K^2}{\sigma_0^2} \qquad (3.25)$$

where $\alpha = 1$ in plane stress and 0.75 in plane strain. This means that were the tests represented by the broken box on Figure 3.8 repeated under plane stress conditions at the same value of C*, then σ_0 is reduced by a factor of 0.75, for the same value of $\dot{\epsilon}_0$.

Nikbin et. al. demonstrate that crack growth rates in plane strain are approximately 50 times greater than in plane stress for the same value of C*. Making these adjustments for $\dot{a}$ and σ_0 has the effect of shifting the data box down (due to the decrease in σ_0) and to the left (due to the decrease in crack growth rate), ie. towards the C* controlled region. This allows us to plot the data as plane stress data (the solid box on Figure 3.8) from which we see that the reported correlation between $\dot{a}$ and C* should, after all, be expected.

Nimonic 80A.

Data for this nickel alloy, which has a creep exponent of 13, are plotted on Figure 3.9. Riedel[49] demonstrates that this data shows a reasonable correlation between $\dot{a}$ and the elastic stress intensity factor K and the positions of the data on the map agree with K being the parameter controlling crack growth.

From their positions on the maps we can readily see that in the majority of the materials considered above, creep rather than elasticity was dominant over the range of temperatures and loads used for the tests. We can also see that the more creep ductile the material, the further to the left on the map it appears and the more likely it is to fail by continuum damage. In materials of intermediate ductility

crack growth is characterised by C*. The most creep brittle materials appear furthest to the right on the map. Nimonic 80A is a complex mixture of nickel, cobalt, tungsten, chromium, aluminium and many other elements in small amounts, the purpose of which is to form hard precipitate particles which obstruct dislocation movement. The result of this is a material with very limited ductility.

Alumina.

It must be remembered that the analysis used to produce these maps is, strictly, only valid for materials with a creep exponent greater than 3. However some engineering ceramics have n values less than or equal to this (reaction bonded silicon nitride, for example, typically displays a value of n in the range $1.0 \leq n \leq 2.0$ [89,90] and n for alumina is often found to be ≈ 1 [4]). Therefore for these materials a different criterion for the change over from creep effects being dominant to elastic effects dominating is required.

The elastic stress field ahead of the crack tip is of the form

$$\sigma \propto r^{-\frac{1}{2}} \qquad (3.26)$$

and the total strain rate ahead of the crack tip is the sum of the creep strain rate and the elastic strain rate, ie.

$$\dot{e}_{ij} = \dot{e}_{ij}^c + \dot{e}_{ij}^e \qquad (3.27)$$

Now, from equation (1.2), for n = 1 we see that

$$\dot{e}_c = \left(\frac{\sigma}{\sigma_0}\right)\dot{e}_0 \qquad (3.28)$$

and therefore, from equations (3.28) and (3.2), that

$$\dot{\epsilon}_c = \left(\frac{K}{\sqrt{2\pi r}} \right) \frac{\dot{\epsilon}_0}{\sigma_0} \qquad (3.29)$$

The elastic strain rate is therefore given by

$$\dot{\epsilon}_e = \frac{d\epsilon_e}{dr} \frac{dr}{dt} \qquad (3.30)$$

where, of course

$$\frac{dr}{dt} = -\dot{a} \qquad (3.31)$$

Therefore

$$\dot{\epsilon}_e = \frac{K}{2\sqrt{2\pi r}} \frac{\dot{a}}{Er} \qquad (3.32)$$

If we define the changeover point from creep dominance to elastic dominance, r*, as being the point at which the elastic strain rate and the creep strain rate are equal, we arrive at the following simple result for the case of linear viscosity.

$$\frac{r^*}{\chi} = \frac{1}{2} \frac{\sigma_0}{E} \frac{\dot{a}}{\dot{\epsilon}_0 \chi} \qquad (3.33)$$

If, as before, we set r* = χ/50 at the change over point we find that the elastic zone is small and creep effects dominate if r* < χ/50. Conversely if r* > χ then elastic effects dominate.

A creep crack growth map for alumina, based on the data of Blumenthal and Evans[88] is given in Figure 3.10, using the above criterion for the change over from elastic to creep controlled growth. To determine the position of the boundary of continuum damage we turn to a later paper in which Dalgleish et. al.[22] further analyse Blumenthal's results and demonstrate that for these data C_{MG} is approximately 10^{-1}. Our analysis is only weakly dependent on the ratio of a_c/a_i so for the plot we have assigned this ratio a value of 10^2.

In the tests used to produce these data it was observed that at high load

levels or if the material contained large pre-existing flaws failure was as the result of the growth of one of these flaws to a critical size, with damage restricted to the immediate vicinity of the crack tip, at which time the specimen failed in a brittle manner with a typical failure strain < 1%. These data are the top-right half of the box on Figure 3.10.

As the load was reduced (and consequently as σ_0 is reduced) the crack growth rate dropped, and the data points move down and to the left ie. into the continuum damage region. Thus we would expect at a certain threshold load level the behaviour to change from brittle to ductile, and indeed this was the case. Below a certain load the pre-existing flaws were found to blunt and failure was the result of the growth and eventual coalescence of widespread damage, with typical failure strains of about 8%. Thus we can see that the position of the data on the map is consistent with experimental observation.

These data for alumina demonstrate clearly the dichotomy of behaviour which is the central theme of this thesis, namely that under different loading conditions the same material may either behave in a brittle or ductile manner.

With the possibilities of two such diverse modes of behaviour further investigation of this duality is of paramount importance. However it is clear that there are many separate factors which affect this phenomenon, such as the number and size of pre-existing flaws, the levels of impurity present in the material and the inability of some cracks to induce a damage zone[22]. In Chapter four we concentrate our theoretical investigation on the creep crack growth regime and in Chapter five we describe our experimental investigation into the creep ductile / creep brittle transition in reaction bonded silicon nitride.

3.5 Design and assessment.

We will now give a simple example to demonstrate how these maps can be used in design. Recall from equation (3.21) that for failure not to occur within the design lifetime, t_d, we require

$$\int_0^{t_f} \dot{e}_0 \, dt \geq \frac{\ln(a_c/a_i)}{\pi \xi} \qquad (3.34)$$

Now, if the design strain limit, ϵ_d, is 1% (say) then the designer obviously requires that this is less than the accumulated strain at failure, ϵ_f, ie.

$$e_f = \int_0^{t_f} \dot{e}_0 \, dt \geq e_d \qquad (3.35)$$

By combining equations (3.35) and (3.21) we can see that for a satisfactory design the designer requires

$$\xi \leq \frac{\ln(a_c/a_i)}{\pi e_d} \qquad (3.36)$$

This is represented by the 'design box' on Figure 3.11.

This type of map would be used in the initial stages of the design process to determine whether creep crack growth is likely to be a problem in a specific component. Data to the left of the design box (by a suitably chosen factor of safety) would indicate a possible growth rate below that necessary to achieve a critical flaw size within the design lifetime.

Current design codes for high temperature components in both the nuclear and conventional power generating industries often start from the premise that the components are initially defect free when they enter service. This is unrealistic, not only because it is extremely difficult to manufacture a completely defect free component of any size or complexity, but also because of the limited resolution of

testing equipment there will always be a minimum size below which defects will escape detection. However, with increasingly more sensitive non destructive testing (NDT) equipment being used, the likelihood of cracks being detected in such plant during routine inspection will increase. An engineer discovering such a flaw must determine whether the component can safely be left in service. It is important that such an assessment is realistic when one considers the high cost of replacement of this type of component (possibly involving partial or complete shutdown of the plant) or the possible of consequences of allowing failure within the design life. These maps may be used as a means of rapidly assessing whether such a cracked component has sufficient residual life or requires replacement.

Procedures for the high temperature assessment of flawed metal components under steady loading conditions based on reference stress techniques have been developed at, for example, what used to be the CEGB[91]. Their R5 procedure which is similar to the R6 procedure for low temperature applications will now be briefly described.

Initially it is necessary to determine the service load and temperature of the component to be assessed. From these the time to failure based on general rupture of the material ahead of the largest known flaw (or the smallest detectable flaw if none is detected) is determined. If this time is shorter than the desired lifetime then this lifetime will not be achieved if a flaw is present and is unlikely to be achieved if none is detected.

Next the incubation period of the crack is determined. This is the time during which the crack blunts due to localised creep at the tip without growing, and is determined using reference stress techniques (the appropriate characterising parameter could be determined using the Riedel type map mentioned earlier).

Obviously if this time is shorter than the current age of the component then the crack must have started to grow. The crack size at the end of the service life is then determined by integrating up the crack growth rate over the lifetime less the incubation time. Some method of characterising the crack growth rate is obviously required for this and the procedure defines conditions for which C* may be used.

The time to failure as a result of general rupture of the uncracked ligament will get shorter as the crack grows due to the reduction of the area of the ligament and the consequent increase in the stress that it carries. This revised time to failure should be calculated, using a new limit load based on the current crack length, to ensure that it exceeds the remaining design life.

Lastly the factor of safety for the crack size at the end of the design life should be determined for all possible load combinations. The acceptability or not of this factor would then be decided. To establish full confidence in the assessment an analysis should then be performed to demonstrate its sensitivity to the accuracy with which the input data are known.

Suppose for example that a component that has been in service for a length of time t, and has accumulated a creep strain ϵ_t, is found to contain a crack of size a_t. For the component to be serviceable the requirement is that the strain that the component can still tolerate before failing is greater than the 'unused' portion of the design strain, ie.

$$\epsilon_f - \epsilon_t \geq \epsilon_d - \epsilon_t \tag{3.37}$$

combining this requirement with equation (3.21) gives

$$\xi \leq \frac{\ln(a_c/a_t)}{\pi(\varepsilon_d - \varepsilon_t)} \qquad (3.38)$$

This is represented by the 'assessment box' on Figure 3.11; in this example the reference stress is taken as being less than E/1000. The significance of this box is that if experimental data relating to growth of the crack in the component lie to the left of the box (again, a suitable safety factor would be applied here) then the component is safe. However if the data lie to the right of the box the component should be replaced or the loading reduced (which has the effect of reducing $\dot{\varepsilon}_0$ and moving the assessment box to the right, away from the material data).

There is however a large 'grey' area in the use of these maps for both design and assessment, not only in the transitional region between C* and K controlled growth, but also in determining whether an implied factor of safety (due to the close proximity of data to a design/assessment box is sufficient. In these cases further analysis would be recommended. This notwithstanding, however, these maps represent a useful and easy to use design/assessment tool.

3.6   Models of creep crack growth.

Numerous models exist in the literature which attempt to explain creep crack growth in engineering materials. One of the simplest of these is due to Cocks and Ashby[73], and extended by Nikbin and Webster[72], who analyse C* controlled growth by considering the strain accumulated in an element of material ahead of a growing crack. They assumed that a critical strain, ε_f, is achieved at the point where the element fails and the crack advances into the material. Their basic model can be expressed in the form

$$\bar{a} = \frac{n+1}{e_f} \left(\frac{\overline{R}}{I_n} \right)^{\frac{1}{n+1}} \tag{3.39}$$

where $\bar{a}$ is the normalised crack growth rate = $\dot{a}/\dot{\epsilon}_0 \chi$. and $\overline{R}$ is the normalised damage zone size = R/χ. For given values of these parameters equation (3.39) represents a vertical line on the map. It can be seen that the position of this line on the map is not particularly sensitive to the value of $\overline{R}$ and becomes less so as n increases. Equation (3.39) is plotted on Figure 3.11 for ϵ_f in the range 0.01 to 0.0001; $\overline{R}/I_n$ = 1 and n = 9. Note that as ϵ_f becomes very small the crack growth rate goes to infinity and as ϵ_f becomes very large crack growth stops; this model is therefore inappropriate near these limits.

It is implicit in this model that the rate of damage accumulation is a function of the creep rate, therefore there can be only one characteristic rate for the crack growth process. The damage rate however need not be a function of the creep rate. If, for example, the deformation within the process zone results from the plating out of material onto grain boundaries as it diffuses away from the voids then the deformation rate within the process zone will be quite different from that in the surrounding material, whether it deforms elastically or creeps.

Ainsworth[52] has developed a model in which the effects of crack tip blunting are considered by assuming that the crack tip blunts into a semi-circular shape. He arrives at the following expression for the crack growth rate in the C* controlled regime.

$$a^{-\frac{1}{n+1}} \dot{a} = \frac{\sqrt{3}}{2} \dot{e}_0 \left(\frac{C^*}{\sigma_0 \dot{e}_0} \frac{(3n+4)}{4n} \right)^{\frac{n}{n+1}} \tag{3.40}$$

Recalling equation (2.17) and that for an arbitrary geometry $\chi \approx \pi a$, this expression

becomes, after normalising,

$$\bar{a} = \frac{\sqrt{3}}{2} \pi^{-\frac{1}{n+1}} \left(\frac{3n+4}{4n} \right)^{\frac{n}{n+1}} \tag{3.41}$$

This equation, assuming n = 9, is represented by the solid vertical line on Figure 3.12 from which we can see that this model lies in the region of the map where we would expect continuum damage rather than crack growth. This model is therefore likely to underestimate the crack growth rate.

Thouless and Evans[84] have developed a model of fully constrained crack growth in a linear viscous material containing a second grain boundary phase, in which K is the characterising parameter. Their basic model is of the form

$$\dot{a} = \left(\frac{3\sqrt{\pi} \, K \sqrt{l} \, (l/\delta_0)}{2\sqrt{2} \, (\delta_c/\delta_0 - 1)} \right) \frac{1}{\eta_b} \tag{3.42}$$

where δ_c is akin to the critical crack tip opening displacement and δ_0 is the initial thickness of the second phase; l is the grain size and η_b is the viscosity of the second phase material. $\delta_c/\delta_0 = 22$ and $l/\delta_0 = 100$ are suggested as reasonable values, and $\eta = \sigma_0/3\dot{\varepsilon}_0$. The small scale damage limit of a ≥ 20R, and the fact that the damage zone of size R comprises z grains of size l, leads to the result that

$$\bar{a} \leq \frac{25\sqrt{2}}{7} \sqrt{\frac{1}{20z}} \tag{3.43}$$

This equation is represented by the solid vertical line on Figure 3.13, for the limiting case of a damage zone of a single grain, from which we can see that it falls within the region of the map where creep effects dominate and that it is applicable at values of $\sigma_0/E < 10^{-2}$.

A model demonstrating a different feature of material behaviour which may

be plotted on a the map is due to Riedel[87]. In this model Riedel develops the continuum damage equation of Kachanov (equation (2.5)) to arrive at the following expression for the crack growth rate (Kachanov uses χ but to avoid confusion between this and the characteristic length we shall use ς)

$$\dot{a} = \frac{n+1}{\varsigma} \left(\frac{\alpha C^*}{B} \right)^{-\frac{\varsigma}{n+1}} D \Delta a^{\frac{n+1-\varsigma}{n+1}} \qquad (3.44)$$

D may be written as

$$D = \frac{\dot{\omega}_0}{\sigma_0^{\varsigma}} \qquad (3.45)$$

where $\dot{\omega}_0$ is a reference value of $\dot{\omega}$ and Δa is the amount of crack growth since the start of the test. Riedel demonstrates that taking a value of $\alpha = 30$ gives a lower bound to the crack growth rate. We may then re-write equation (3.44) as

$$\bar{a} = 30^{\frac{\varsigma}{n+1}} \frac{n+1}{\varsigma} \frac{\dot{\omega}_0}{\dot{e}_0} \left(\frac{\Delta a}{\chi} \right)^{\frac{n+1-\varsigma}{n+1}} \qquad (3.46)$$

For aluminium the appropriate values are n = 6.9; ς = 6.48. Thus the normalised growth rate depends on the ratio of two characteristic rates. Equation (3.46) is plotted on the map of Figure 3.14.

3.7   Summary.

In this chapter we have presented a simple map which readily allows the performance of cracked components to be assessed by direct comparison of material data with design and assessment criteria. The predictions of theoretical models of the creep crack growth process can be plotted directly onto these maps which then provide a means of assessing the range of validity of the model.
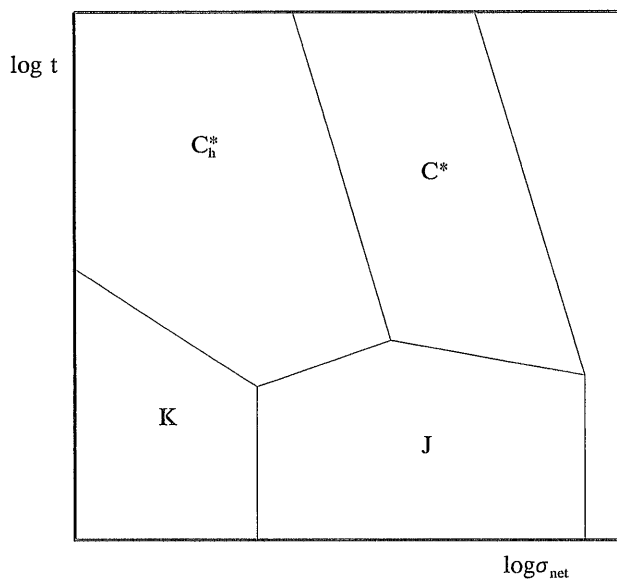
Figure 3.1. A Riedel type map[49] in stress-time space for a hypothetical material. The different regions represent the different characterising parameters applicable at that point in the stress-time history of the material.
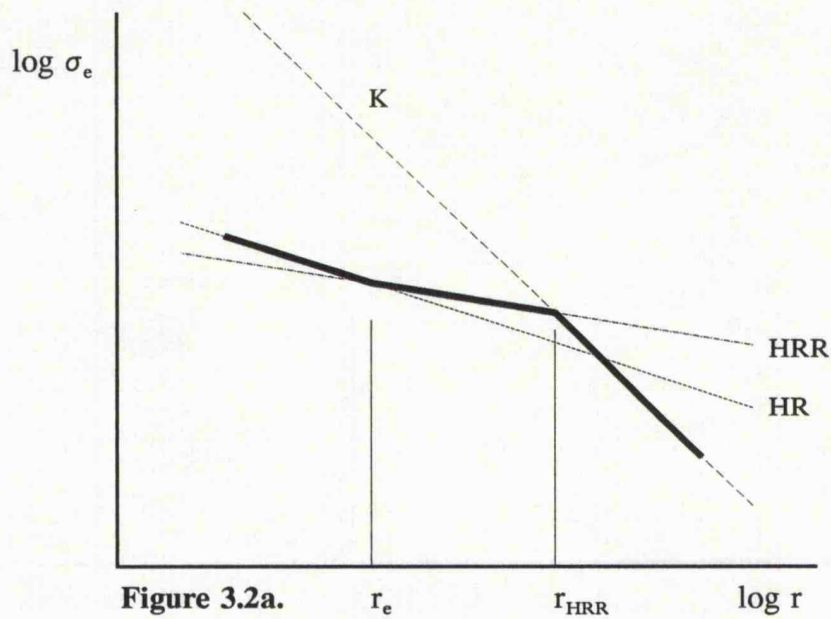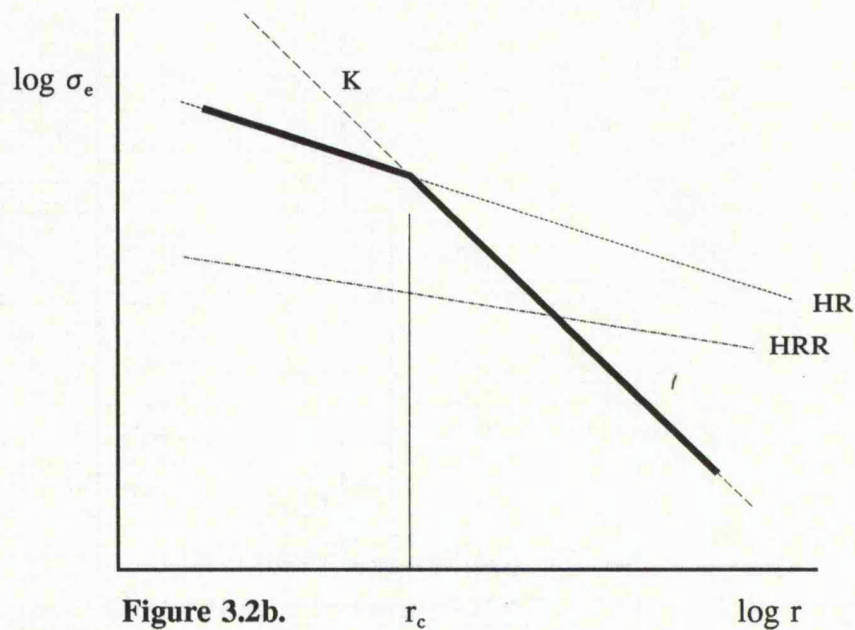
Figure 3.2a.

$\log \sigma_e$
K
HRR
HR
r_e r_{HRR} $\log r$

Figure 3.2b.

$\log \sigma_e$
K
HR
HRR
r_c $\log r$

Figures 3.2a and 3.2b. Schematic plots of effective stress as a function of distance from the tip of a growing crack in a material for which n > 3. Figure 3.2a shows the steady state situation ahead of a slowly growing crack where r_e is the edge of the zone within which elastic effects are important in an otherwise largely creeping material (note that in large specimens there may still be an elastic region in the extreme far field, outside r_{HRR}). Figure 3.2b shows the steady state ahead of a rapidly growing crack (note that the K and HRR fields are the same, but that the HR field, a function of crack growth rate, has increased in magnitude, and that therefore the region of dominance of the HRR field , r_{HRR} - r_e has disappeared); r_c is the limit of the region where creep effects are important in an otherwise elastic material.
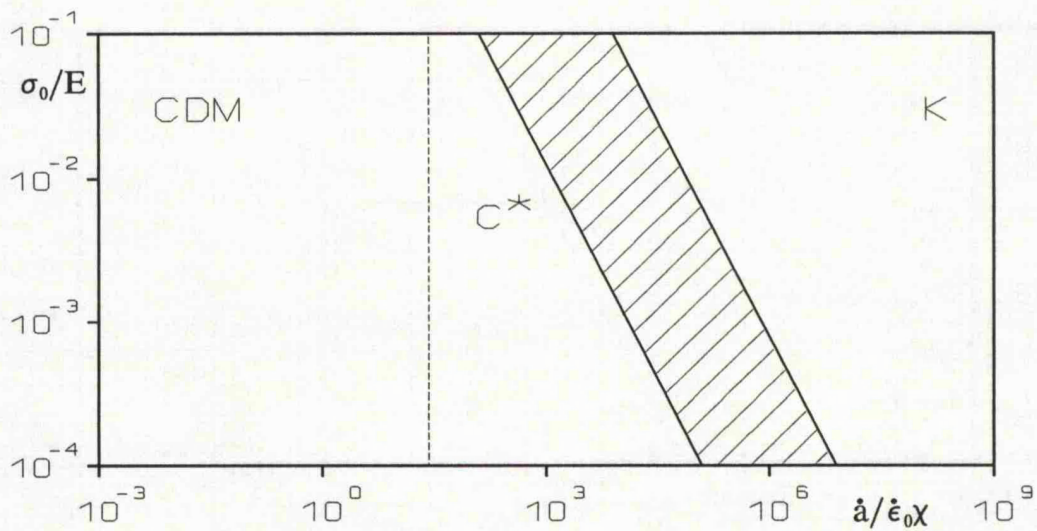
Figure 3.3. A creep crack growth map for a material for which n = 9. The region to the left of the dashed line represents the conditions under which failure by continuum damage may be expected to occur if C_{MG} = 0.07 and a_c/a_i = 10^3. The hatched region represents neither C* or K control.
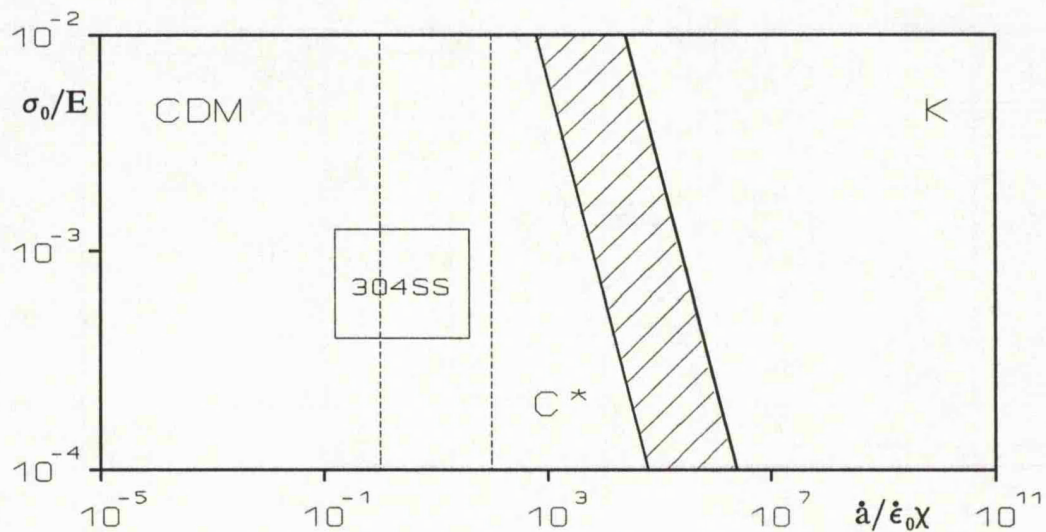
Figure 3.4. A creep crack growth map for 304 stainless steel, for which n = 8. This is a very ductile material with the specimens displaying a strain at failure of up to 0.4. The dashed vertical lines represent the boundary of the transition from C* controlled creep crack growth to continuum damage. We can see that if C_{MG} were at the higher end of its experimentally observed range we might expect continuum failures rather than crack growth to be the dominant failure mechanism.
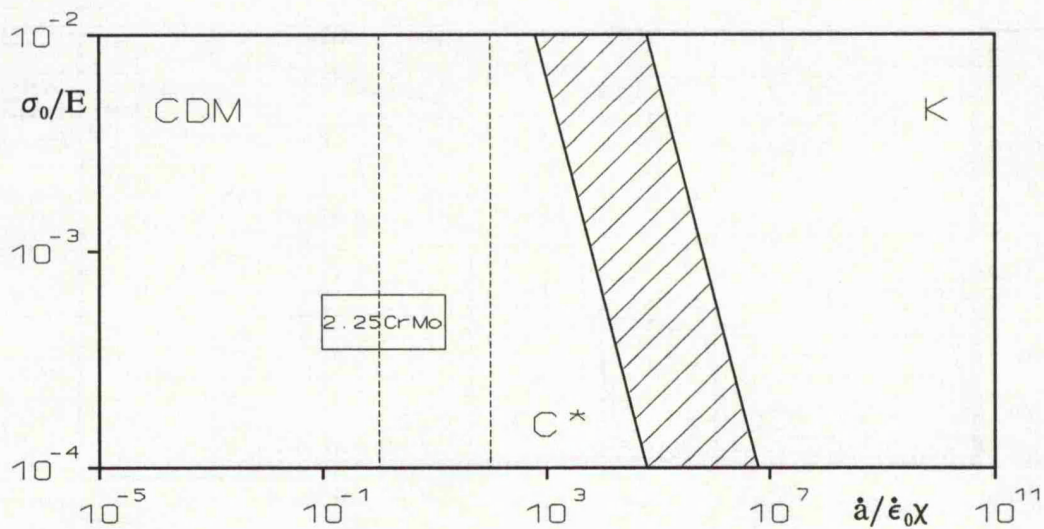
Figure 3.5. A creep crack growth map for 2¼CrMo steel, for which n = 9. This steel is even more ductile than the 304 stainless steel described above with a failure strain of up to 0.45. As expected for a material as creep ductile as this all the data all lie comfortably within the region indicating that creep was C* controlled rather than K controlled.

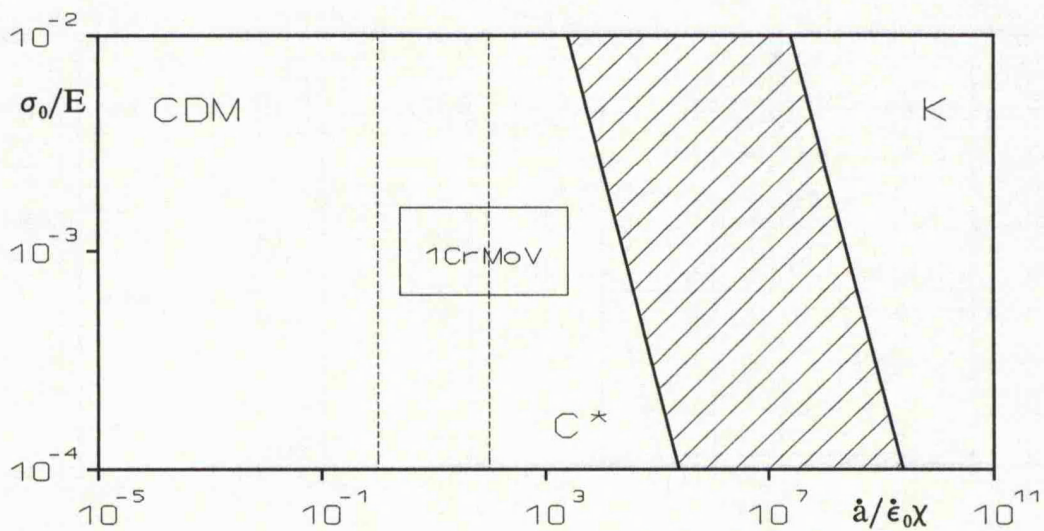**Figure 3.6.** A creep crack growth map for a 1CrMoV steel, for which n = 14. This steel is rather less creep ductile than the steels of the previous two Figures, demonstrating a failure strain of 0.2. However we can see that the data for this material also fall within the limit of C* control.
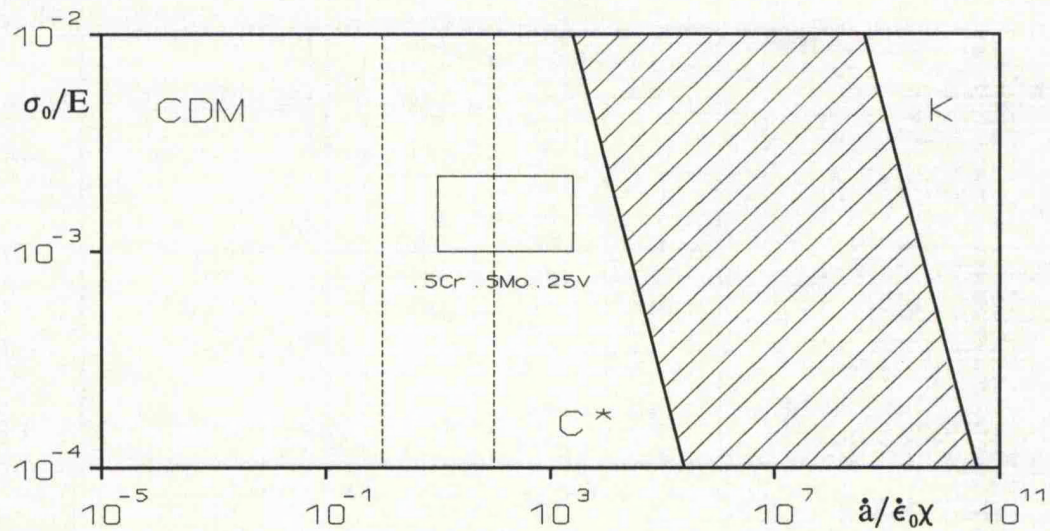
Figure 3.7. A creep crack growth map for a ½Cr½Mo¼V steel, for which n = 17. This steel is much less creep ductile than any of the previous materials displaying a strain at failure of < 0.05. We can see that again these data, even the data approaching plane strain at the right of the box, fall within the region of C* controlled creep crack growth.
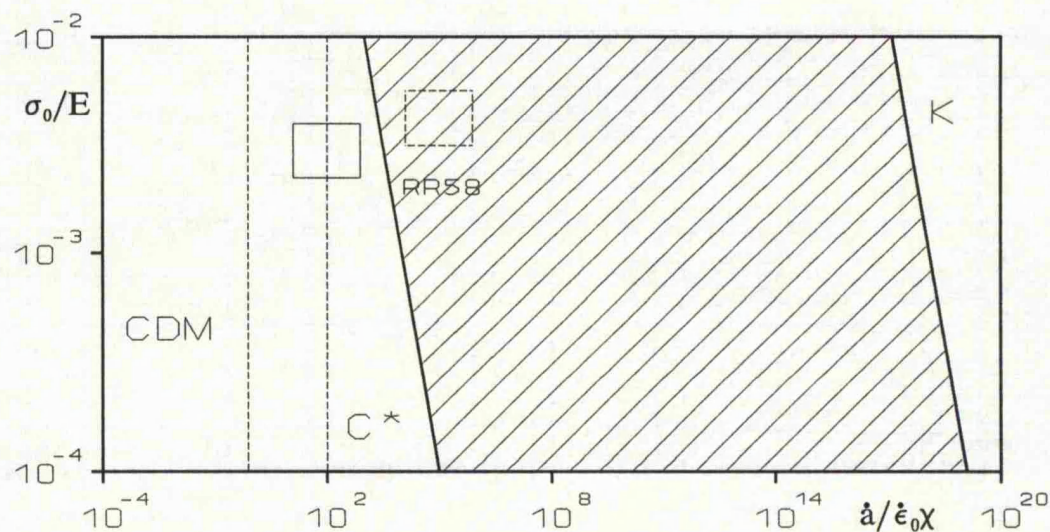
Figure 3.8. A creep crack growth map for the aluminium alloy RR58 (2½Cu1½Mg), for which n is reported as being 35. This alloy shows very little creep ductility and Nikbin et. al.[74] demonstrate that conditions at the crack tip approach plane strain for these data (broken box). The position of this box on the map indicates that one would not expect a very good correlation between crack growth rate and C*, yet Nikbin et. al. do report such a correlation. However the broken box represents the plane strain data, for which the analysis used to derive the map is invalid. When the data are modified for plane stress (the solid box) we see that the reported correlation between C* and å is to be expected.
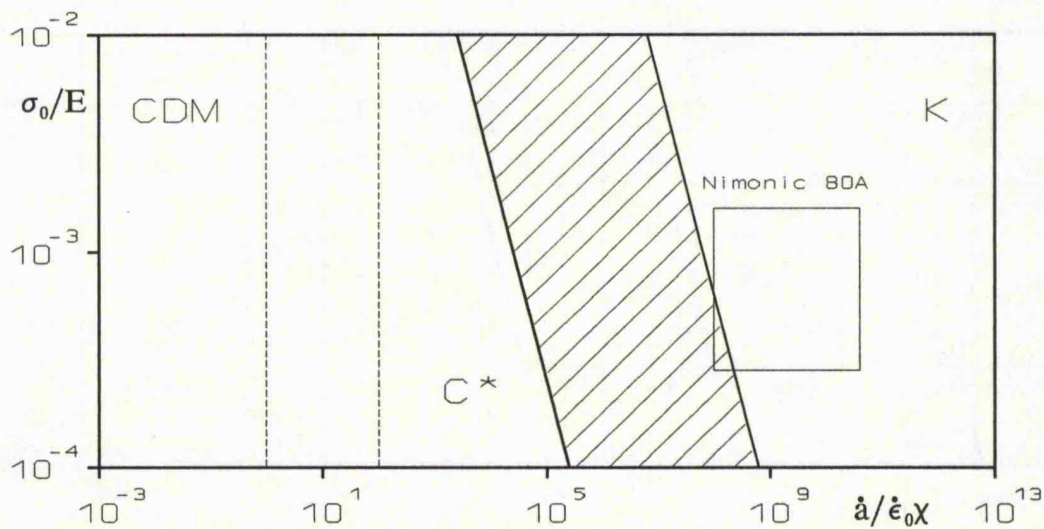
Figure 3.9. A creep crack growth map for the nickel alloy Nimonic 80A, for which n = 13. Riedel[49] reports a reasonable correlation between å and the elastic stress intensity factor K for these data and we can see that the position of the data on the map agrees with this.
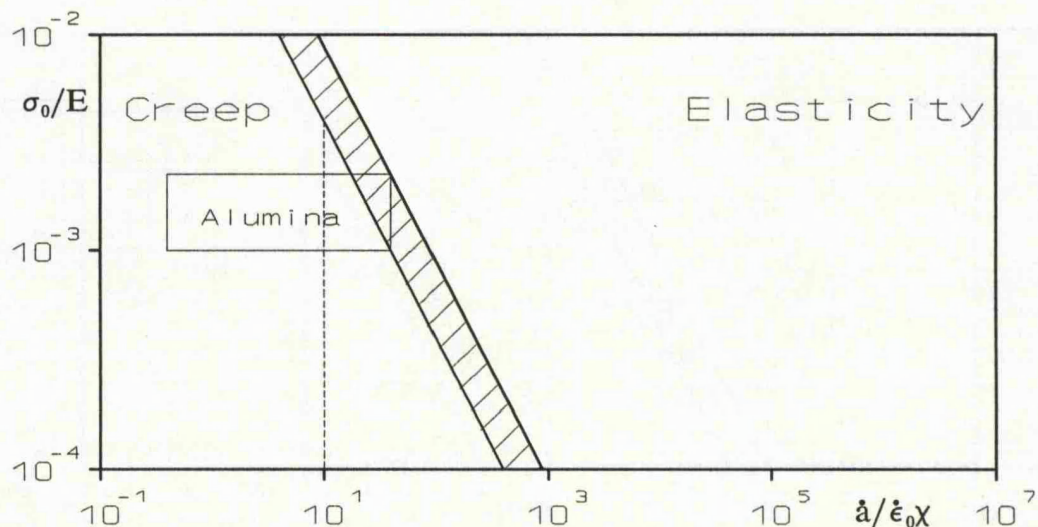
Figure 3.10. A creep crack growth map for alumina assuming n = 1. For n < 3 the criteria for determining the positions of the demarcation lines on the boundaries between C* and K control, used to produce the previous maps are not valid so a different criterion based on an equivalence of creep and elastic strain rates is used to determine the boundary on this map. Note that if n = 1 C* and K are related through equation (1.19) and so one can not distinguish between C* and K control but we can say whether creep or elastic effects dominate in the material. As in Figure 3.3 the dashed line represents the boundary between creep crack growth and continuum damage in which C_{MG} is taken as 10^{-1} [11] and a_c/a_i is 10^2. We can see that these data are a mixture of continuum damage and creep crack growth.
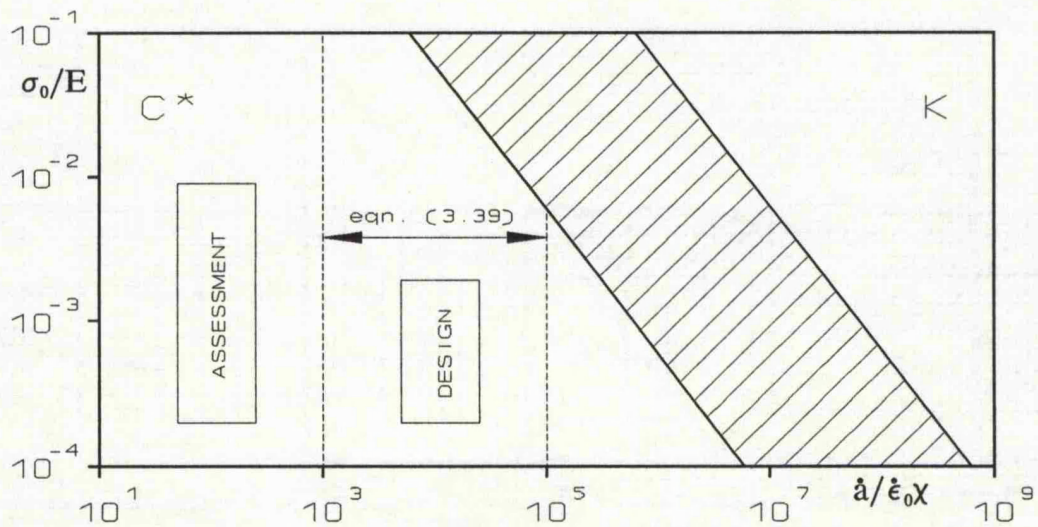
Figure 3.11. A creep crack growth map for a material, assuming n = 9, showing the validity of a simple crack growth model and regions associated with the design and assessment of high temperature plant. In the Figure the failure strain, ϵ_f, varies from 0.01 to 0.0001.
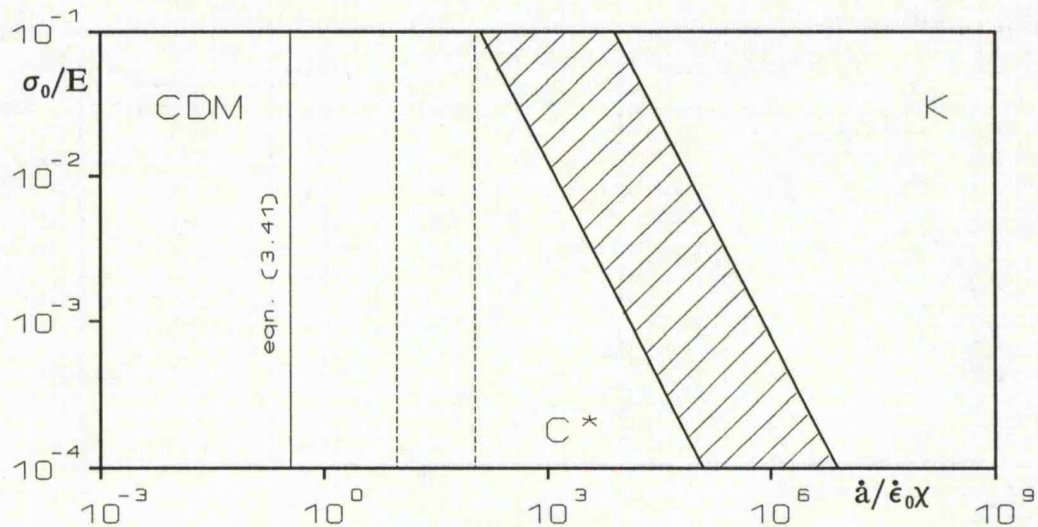
Figure 3.12. A creep crack growth map for a material, assuming n = 9, showing the prediction of a creep crack growth model due to Ainsworth[52] (equation (3.41)) as a solid vertical line. This model lies in the region of the map where we would expect continuum damage rather than crack growth and so we would expect this model to be unconservative and to underestimate crack growth rates observed in practice.
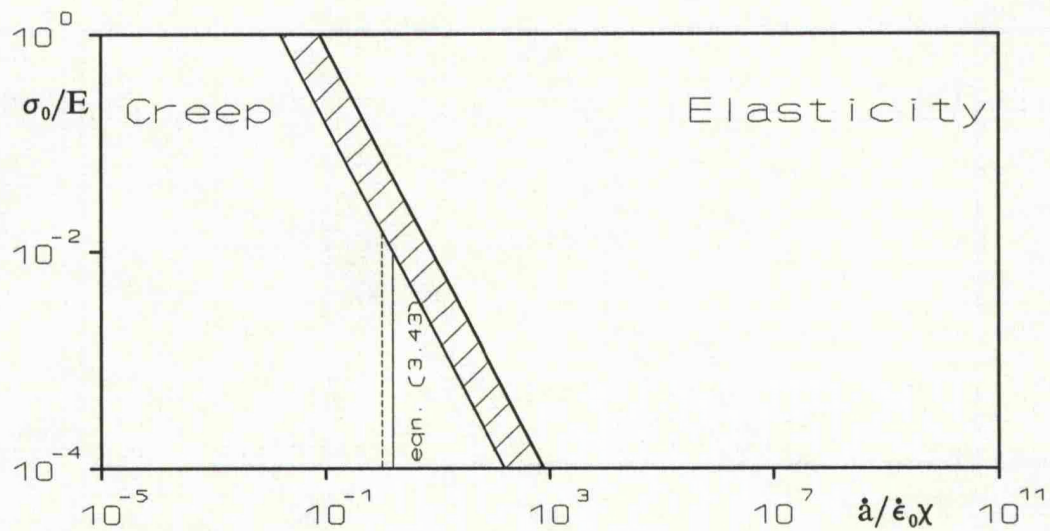
Figure 3.13. A creep crack growth map for a linear viscous material, showing the range of applicability of a crack growth model due to Thouless and Evans[84] (equation (3.43)) as a solid vertical line. The model is valid for values of $\sigma_0/E < 10^{-2}$.
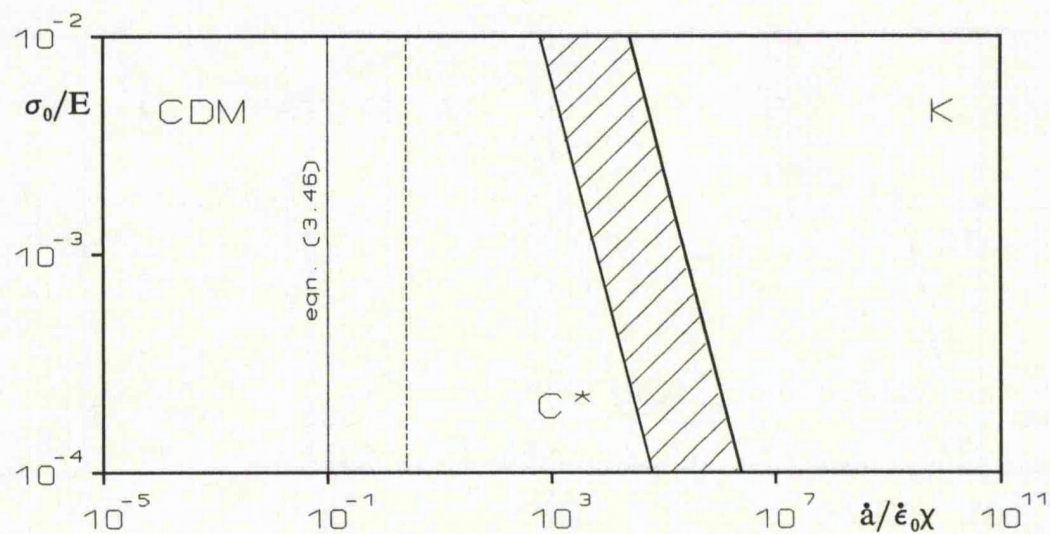
Figure 3.14. A creep crack growth map showing the validity of a model due to Riedel [87] (equation (3.46)). Data for aluminium ($n = 6.9$; $\varsigma = 6.48$; $C_{MG} = 0.33$) are used to determine the positions of the boundaries between continuum damage, C^* and K control; the model is represented for the case of $\dot{\omega}_0/\dot{\epsilon}_0 = 10^{-2}$. As the model is based on failure due to continuum damage we can determine from the Figure that the model only falls within the region where this is dominant (for these specific values of n and ς) if $\dot{\omega}_0/\dot{\epsilon}_0 < 0.27$. We can also see from equation (3.46) that as the crack grows Δa increases and $\bar{a}$ moves to the right on the map.

CHAPTER FOUR: CAVITY GROWTH AHEAD OF A GROWING CRACK

4.1   Introduction.

In this chapter we consider mechanisms for the limiting cases of both constrained and unconstrained void growth. We then introduce an intermediate case based on a prescribed displacement rate field ahead of the crack tip. In this third, 'partially constrained', case we use the path independence of the C^* integral to relate the near and far fields and thus determine the form of the displacement rate field. The validity of this partially constrained case is verified by comparison with results from a different model in the literature. By combining these three fields we demonstrate how the material behaviour changes with increasing crack velocity. We then demonstrate how the creep crack growth maps, developed in the previous chapter, may be used to determine the range of applicability of the crack growth model.

Initially we concentrate our attention on the region on the left of the creep crack growth map where C^* dominates and because the presence of damage on either side of the crack plane is assumed not to influence the crack growth rate we consider the situation where the damage is restricted to a zone of a prescribed length, R, ahead of the crack tip.

We then go on to examine the situation where elastic effects dominate, on the right of the map, and we examine how, if at all, the size of the damage zone varies with the applied load and any other material parameters.

4.2   Mechanisms of cavity growth.

Creep cavities can grow by any combination of several different mechanisms. The mechanism that we will examine here is growth by the stress directed diffusion of matter from the surface of the cavity into the grain boundary. As matter leaves

the surface of the void the void's volume increases and as the matter is deposited on the grain boundary the grains are 'jacked' apart. This jacking further increases the volume of the void and, as matter is deposited on grain boundaries which are in tension, does work equal to the loss of potential of the deposited atom.

Rapid diffusion of matter over the surface of the void means that its lenticular equilibrium shape is maintained. By assuming that growth by power law creep does not occur, ie. that the surrounding grains are rigid, that the lenticular shape and dihedral angle 2ψ (typically $75°$[9]) are maintained and that the supply of grain boundary vacancies is limitless, the equations governing boundary controlled diffusive growth can be solved. The early work in this area was done by Hull and Rimmer[15] in 1959 and by Speight and Harris[16] in 1967. However Raj and Ashby[9] have pointed out that in solving the governing equation the earlier workers assumed incorrect boundary conditions. More recent analysis of boundary controlled diffusion[eg.92,93] has progressed to the point where the mechanism is now quite well understood.

If diffusion through the grain boundary is rapid then diffusion over the void surface becomes the rate controlling mechanism. When material diffuses out from the perimeter of the void faster than the remaining matter can redistribute over the surface then instead of approximating a sphere the cavity can become penny-shaped or develop finger-like growths. The growth of these non-equilibrium cavities has been analysed by Chuang and Rice[94], work which was later developed by Chuang et. al[18].

4.3   Constrained cavity growth.

Although the basic mechanisms of boundary and surface controlled diffusion are well understood they do not accurately describe the behaviour of real materials

as they greatly overestimate the void growth rates and consequently underestimate the rupture times that are found in practice. This occurs because for most of the time during creep, cavitation is limited to a few discrete grain boundaries, which are surrounded by uncavitated material. Dyson[95] was the first to realise that if this undamaged material were rigid it would constrain the voids and no increase in their volume would be possible, and that therefore void growth could not occur without some deformation of the surrounding material. This phenomenon is called constrained cavity growth.

To illustrate the effect of this constraint consider a bar of material which is held between two rigid supports. Suppose that the specimen is now strained by an amount ϵ. The specimen is prevented from deforming by the rigid supports. If we heat the specimen into its creep range (which we will assume to be below that of the supports, which therefore do not creep) the elastic stress within the specimen reduces as the material relaxes, and creep strains replace elastic strains.

Thus in the case of constrained void growth the stress within the damage zone (the bar) is low compared with that in the bulk of the material (the rigid supports). In the limiting case of fully constrained behaviour the stresses have completely relaxed and the behaviour is controlled by the displacement field, in the same way as the relaxation of the imaginary specimen is controlled by the amount by which it is initially strained.

4.4 Constrained cavity growth in a cracked geometry.

In a cracked geometry the growth of damage ahead of the crack tip is similarly constrained by the deformation of the surrounding material. In the fully constrained case the stresses within the damage zone are assumed to be fully relaxed, with neither the crack or the damage zone carrying any load. In a manner

analogous to Dugdale's plastic zone correction[29] discussed in Chapter one, the damage zone can then be considered an extension to the crack which behaves as though it were of length $a + R$.

Consider an array of voids contained within a damage zone of length R ahead of a crack in a creeping material. We can model this situation as a series of uniaxial specimens, a distance 2λ apart, each containing a single void; the specimens being strained at different rates depending on their positions in the damage zone. Consider now one of these unit cells (see Figure 4.1). The volume, v, of the unit cell is given by

$$v = 4\lambda^2 \delta \qquad (4.1)$$

As λ is a constant the increase in the volume of the cell, dv, is given by

$$dv = 4\lambda^2 d\delta \qquad (4.2)$$

If the crack only grows when voids coalesce, or the intervening ligament ruptures, then it must grow in increments of 2λ, and so

$$2\lambda = \dot{a} dt \qquad (4.3)$$

from this it is apparent that

$$d\delta = \frac{d\delta}{dt} dt = \frac{d\delta}{dt} \frac{2\lambda}{\dot{a}} = \frac{2\dot{\delta}\lambda}{\dot{a}} \qquad (4.4)$$

and so therefore by combining equations (4.2) and (4.4) the change in volume of the cell can be expressed as

$$dv = \frac{8\dot{\delta}\lambda^3}{\dot{a}} \qquad (4.5)$$

Obviously this change in volume represents the change in volume of the void, as the

volume of the surrounding material cannot change. If we then assume, to simplify the calculation, that in equilibrium the voids are spherical we can see that

$$dv = \frac{4}{3}\pi\left(r_2^3 - r_1^3\right) \qquad (4.6)$$

where the subscripts 1 and 2 denote the radii of the void before and after the growth event respectively. If we now introduce a new term, the *volume* fraction of a void, F, which is related to the area fraction, f (defined by equation (1.7)), by

$$F = f^{1.5} \qquad (4.7)$$

then from equations (4.2) and (4.6) we may write

$$d\delta = \frac{dv}{4\lambda^2} = \frac{1}{3}\pi\lambda\left(F_2^2 - F_1^2\right) \qquad (4.8)$$

From equation (4.4) it is also obvious that

$$d\delta = \dot{\delta}\, dt = \frac{\dot{\delta}\, dx}{\dot{a}} \qquad (4.9)$$

The displacement at the crack tip, δ_t is

$$\delta_t = \int_0^R \frac{\dot{\delta}}{\dot{a}}\, dx \qquad (4.10)$$

which is equal to $d\delta$ in equation (4.8) if F_2 and F_1 are respectively the volume fractions of the void at the crack tip and at the far edge of the damage zone, and therefore

$$\dot{a} = \int_0^R \frac{3\dot{\delta}\, dx}{\pi\lambda\left(F_2^2 - F_1^2\right)} \qquad (4.11)$$

In order to proceed further it is apparent that the displacement rate as a function of position within the damage zone is required. In the limiting case of

fully constrained behaviour the stress within the damage zone has completely relaxed. Therefore from the point of view of the material outside the zone it appears that the damage zone contains no material and the crack is really of length a+R. The analogous solution in plasticity for the deformed shape of a crack is given by Goldman and Hutchinson[50]. Making use of the visco-plastic analogy we may then write

$$\dot{\delta}(x) = \dot{e}_0 k_c x^{\frac{1}{n+1}} I_n^{\frac{n}{n+1}} f_3^{\frac{-n}{n+1}} \qquad (4.12)$$

where

$$k_c = \left(\frac{C^*}{\sigma_0 \dot{e}_0 I_n} \right)^{\frac{n}{n+1}} \qquad (4.13)$$

Therefore

$$\dot{a} = \frac{(n+1)\ 3\dot{e}_0 \left(\dfrac{C^*}{\sigma_0 \dot{e}_0} \right)^{\frac{n}{n+1}} f_3^{\frac{-n}{n+1}} R^{\frac{n+2}{n+1}}}{(n+2)\pi \lambda \left(F_2^2 - F_1^2 \right)} \qquad (4.14)$$

For a crack in an infinite plate the function f_3 is dependent solely on the creep exponent, n, and for the case of linear viscosity $f_3 = \pi/3$[50]. We can rewrite equation (4.14) in nondimensional form by recalling from equation (2.17) that

$$C^* = \sigma_0 \dot{e}_0 \chi \qquad (4.15)$$

As χ has the dimension of length, therefore so does $C^*/\sigma_0 \dot{e}_0$, which means that C^*/σ_0 is a velocity. We can now introduce the following nondimensional groups

$$\bar{a} = \frac{\dot{a}\,\sigma_0}{C^*} = \frac{\dot{a}}{\dot{e}_0 \chi} \qquad (4.16)$$

$$\bar{R} = \frac{R\,\sigma_0\,\dot{e}_0}{C^*} = \frac{R}{\chi} \qquad (4.17)$$

$$\bar{\lambda} = \frac{\lambda\,\sigma_0\,\dot{e}_o}{C^*} = \frac{\lambda}{\chi} \qquad (4.18)$$

and therefore equation (4.14) can be written

$$\bar{a} = \frac{3\,(n+1)\,f_3^{-\frac{n}{n+1}}\,\bar{R}^{\frac{n+2}{n+1}}}{(n+2)\,\pi\,\bar{\lambda}\,(F_2^2 - F_1^2)} \qquad (4.19)$$

4.5 Unconstrained cavity growth in a cracked geometry.

Fully constrained void growth models a small, compliant, damage zone contained within an elastic matrix. If this represents one limiting form of behaviour then unconstrained cavity growth represents the other limit.

In unconstrained growth the material surrounding the damage zone is comparatively soft and void growth is controlled by the diffusive processes discussed in the introductory chapter which are in turn controlled by the stress acting on the damage zone. Riedel[96] has demonstrated that the growth rate of the crack depends on the applied load level, characterised by C^*; with diffusive void growth being the dominant mechanism at low crack growth rates.

If we assume that the damage zone associated with the crack is sufficiently small so as not to influence the stress field, then the field is of the HRR form described earlier

$$\sigma_{ij} = \left(\frac{\sigma_0^n\,C^*}{\dot{e}_0\,I_n\,x}\right)^{\frac{1}{n+1}} \sigma_{ij}(\theta) \equiv A\left(\frac{1}{x}\right)^{\frac{1}{n+1}} \qquad (4.20)$$

Recalling the approximation to Raj and Ashby's expression for the volumetric flow rate of matter from a void under the action of an applied stress[9]

$$\frac{dv}{dt} = \frac{2\pi D_b \delta_b \sigma \Omega (1-f)}{kT \ln\left(\frac{1}{\sqrt{f}}\right)} \qquad (4.21)$$

Now it is apparent that

$$\frac{dF}{dt} = \frac{dv}{dt}\frac{dr}{dv}\frac{dF}{dr} \qquad (4.22)$$

so if we again assume spherical voids, and combine equations (4.22) and (4.7) we see that

$$\frac{dF}{dt} = \frac{3 D_b \delta_b \Omega (1-F^{\frac{2}{3}})\sigma}{2kT\lambda^3 \ln\left(\frac{1}{\sqrt[3]{F}}\right)} \qquad (4.23)$$

If we now introduce a nondimensional term, ϕ_0, such that

$$\phi_o = \frac{2\Omega D_b \delta_b \sigma_0}{kT\lambda^3 \dot{e}_0} \qquad (4.24)$$

we obtain the result that

$$\frac{dF}{dt} = \frac{3\phi_0 \dot{e}_0 (1-F^{\frac{2}{3}})}{4\sigma_0 \ln\left(\frac{1}{\sqrt[3]{F}}\right)} A\left(\frac{1}{x}\right)^{\frac{1}{n+1}} \qquad (4.25)$$

where ϕ_0 represents the ratio of creep due to diffusion in the damage zone to that due to power law creep of the undamaged matrix. If ϕ_0 is large then diffusion within the damage zone is rapid compared with power law creep of the surrounding matrix. This leads to relaxation of the stresses within the damage zone. A low

value of ϕ_0 implies that power law creep of the matrix is faster than diffusion within the damage zone and plating onto the grain boundaries of material which has diffused out of a void is easily accommodated by creep of the matrix; the stress field within the zone is not relaxed. This means that in effect ϕ_0 is a measure of the degree of constraint. However this does not mean that for full constraint $\phi_0 \to \infty$; it will be shown later that full constraint, in terms of an upper bound to the crack growth rate is reached at a finite value of ϕ_0.

Now, of course, dx/dt is the rate at which the element of material is moving towards the crack tip, ie.

$$\frac{dx}{dt} = -\dot{a} \qquad (4.26)$$

and so

$$dF = \frac{-3\phi_0\dot{e}_0(1-F^{\frac{2}{3}})dx}{4\sigma_0\dot{a}\ln\left(\frac{1}{\sqrt[3]{F}}\right)} A\left(\frac{1}{x}\right)^{\frac{1}{n+1}} \qquad (4.27)$$

Rearranging equation (4.27) and integrating gives the result

$$\dot{a} = \frac{3(n+1)}{4n}\frac{\phi_0\dot{e}_0A}{G(F)\sigma_0}R^{\frac{n}{n+1}} \qquad (4.28)$$

where G(F) is the following nondimensional function of F

$$G(F) = \int_{F_1}^{F_2}\frac{\ln\left(\frac{1}{\sqrt[3]{F}}\right)}{(1-F^{\frac{2}{3}})}dF \qquad (4.29)$$

A plot of how G(F) varies with F_2 is shown in Figure 4.2 assuming a volume fraction, F_1, at nucleation of zero.

The growth of voids directly ahead of the crack tip is determined by the

stress normal to the boundaries on which the voids are situated ie. σ_{22} when $\theta = 0$. Therefore the crack growth rate is given by

$$\dot{a} = \frac{3\,\phi_0}{4\,G(F)}\;\frac{n+1}{n}\left(\frac{\dot{\epsilon}_0^n C^*}{I_n\,\sigma_0}\right)^{\frac{1}{n+1}}\sigma_{22}(0)\,R^{\frac{n}{n+1}} \qquad (4.30)$$

or, in nondimensional form

$$\bar{\dot{a}} = \frac{3(n+1)}{4n}\;\frac{\phi_0}{G(F)}\,I_n^{-\frac{1}{n+1}}\,\bar{R}^{-\frac{n}{n+1}}\,\sigma_{22}(0) \qquad (4.31)$$

where I_n is given by equation (3.4) and in plane stress $\sigma_{22}(0) = 1$. In plane strain the maximum value of σ_{22}, when $\theta = 0$, is given by

$$\sigma_{22}(0) = \frac{2}{\sqrt{3}} + \left(\frac{n-1}{n}\right)^2\frac{\pi}{\sqrt{3}} \qquad (4.32)$$

Thouless et. al.[35] have developed a model in which the constraint in the crack tip damage zone is modelled using dislocation theory. Making use of Hoff's visco-elastic analogy[31] a series of dislocations is placed in the plane of the crack, ahead of the tip, to model the displacement rates of each grain. The sum of the Burger's vectors at each point corresponding to the displacement rate at that point. The compressive stress at a given distance from the crack tip due to a particular dislocation is a standard result from dislocation theory and so the total stress field ahead of the crack can be found by superposition. Thouless uses this model to produce curves of normalised crack velocity as a function of the number of grains in the damage zone, z, ie. as a function of its size.

The Thouless model is limited to the case of linear viscous creep and is a discrete model, that is results are obtained only at the centres of the 'grains' in the damage zone, while the model presented here is continuous and also valid for n >

1. However, it will be instructive to compare the results from our model with those due to his. The comparison is not straightforward as we have obtained the dimensionless crack growth rate as a function of the damage zone size, R, where Thouless plots $\eta\dot{a}/K\sqrt{l}$ as a function of the number of grains in the damage zone. The conversion from one form to another is however possible (see Appendix 3) by recalling from equation (1.19) that K and C^* are related through the material viscosity, η

$$K^2 = 3\eta C^* \qquad (4.33)$$

This equation is derived from the behaviour of a creeping material under shear loading. Thouless, however, appears to have started from an equivalent expression for tensile loading as he uses the expression

$$K^2 = \eta C^* \qquad (4.34)$$

The factor of 3 difference is not significant in that it does not alter the underlying behaviour of the material but to enable an accurate comparison of the two models we will use equation (4.34). It is shown in Appendix 3 that

$$\phi_0 = \frac{(l/\lambda)^3}{6\pi} \qquad (4.35)$$

and that equations (4.19) and (4.31) can be rewritten in the form used by Thouless et. al. allowing a direct comparison to be made between their results and ours. Our results and those due to Thouless et. al. are shown in Figure 4.3 for an unconstrained creep crack with an area fraction at failure, $f_c = \frac{1}{2}$ and a $l/\lambda = 5$. It can be seen that both results are of the same order and both predict a crack velocity proportional to $\sqrt{z}$. However, these similarities apart, agreement between the results is not very close.

The approximate void growth rate equation, equation (4.21), was used initially, in preference to the full equation used by Thouless, as it is a conveniently simple approximation; displaying the characteristics of the more accurate model but without possibly 'unnecessary' detail obscuring the physics underlying the result. However, it is clear that in this situation equation (4.21) does not work well. We can considerably improve the agreement by replacing equation (4.21) with the same form of growth law as the Thouless model uses and making the same approximation that the effects of sintering (which we shall investigate later), and any internal pressure are negligible. This results in a different expression for G(F).

$$G(F) = \frac{1}{4} \int_{F_1}^{F_2} 2 \ln(1/F^{\frac{2}{3}}) - (1-F^{\frac{2}{3}})(3-F^{\frac{2}{3}}) \, dF \qquad (4.36)$$

Using this expression, which we evaluate numerically, instead of equation (4.29), we obtain much better agreement between the results of the two different models, as shown by the shorter dashed lines in Figure 4.3, for the same values of f_c and l/λ as before.

4.6 Intermediate behaviour.

Above we have developed models of fully constrained and unconstrained crack growth. These are limiting forms of behaviour, and obviously as a crack grows its behaviour will not instantaneously change from one limit to the other. In reality there will be a transitional 'partially constrained' phase. It is this form of behaviour and its range of validity that we will consider in this section.

Consider an array of voids ahead of a crack tip that is opening at a rate $\mathring{\delta}_t$ (see Figure 4.4). Assume that the displacement rate within this zone is some function of position and of the displacement rate at the crack tip. ie.

$$\dot{\delta} = \dot{\delta}_t G(x/R) \tag{4.37}$$

This assumption will be justified later, but for now, if we consider an element of the damage zone of length dx and unit width, the rate of increase of volume of the element is

$$\frac{dv}{dt} = \dot{\delta} \, dx \tag{4.38}$$

If the voids are equilibrium shaped, which we again approximate as spherical, then the total volume of all the voids, V, is simply the volume of a single void multiplied by the total number of voids.

$$V = \frac{4}{3} \pi r^3 \frac{dx}{\pi \lambda^2} \tag{4.39}$$

If we apply equation (4.22) to this situation we find that

$$\frac{df}{dt} = \frac{\dot{\delta}}{2 \lambda \sqrt{f}} \tag{4.40}$$

Now

$$\frac{dF}{dt} = \frac{dF}{df} \frac{df}{dt} = \frac{3}{2} \sqrt{f} \frac{df}{dt} \tag{4.41}$$

and so it follows that

$$\frac{dF}{dt} = \frac{3 \dot{\delta}}{4 \lambda} \tag{4.42}$$

Of course we may also write

$$\frac{dF}{dt} = \frac{dF}{dx} \frac{dx}{dt} \tag{4.43}$$

By comparing equations (4.42) and (4.43) and remembering equation (4.26) we

obtain the result that

$$\frac{dF}{dx} = -\frac{3\dot{\delta}}{4\lambda\dot{a}}$$
(4.44)

If we consider void growth by boundary controlled diffusion alone, we have, from

Cocks and Ashby[97]

$$\dot{\delta} = \frac{3\lambda\phi_0\dot{e}_0}{ln(1/F)}\left(\frac{\sigma}{\sigma_0}\right)$$
(4.45)

Before the analysis can continue we must first specify the displacement rate

function G(x/R); we can then integrate equation (4.45) between the given boundary

conditions that

$$F = F_1 @ x = R$$
(4.46)

and
$$F = F_2 @ x = 0$$
(4.47)

Consider a displacement rate field of the form

$$\dot{\delta} = \dot{\delta}_t(1-x/R)^m$$
(4.48)

Where m is a suitably chosen constant. Consideration of the first boundary

condition, equation (4.46), gives

$$F = F_1 + \frac{3R\dot{\delta}_t}{4\lambda\dot{a}(m+1)}(1-\bar{x})^{m+1}$$
(4.49)

where $\bar{x} = x/R$, and consideration of equation (4.47) gives

$$F_2 - F_1 = \frac{3R\dot{\delta}_t}{4\lambda\dot{a}(m+1)}$$
(4.50)

Combining equations (4.49) and (4.50) gives the volume fraction at the

dimensionless position, $\bar{x}$, within the damage zone as

$$F = F_1 + (F_2 - F_1)(1 - \bar{x})^{m+1} \tag{4.51}$$

If we now combine equations (4.45), (4.48), and (4.51) we can determine the stress field around the damage zone which would result in a displacement rate field of the form of equation (4.48)

$$\frac{3\lambda\phi_0\dot{e}_0}{\dot{\delta}_t}\frac{\sigma}{\sigma_0} = (1 - \bar{x})^m \ln\left(\frac{1}{F_1 + (F_2 - F_1)(1 - \bar{x})^{m+1}}\right) \tag{4.52}$$

Consider again the displacement rate field given by equation (4.48). If we assume that displacement only occurs in the direction perpendicular to the plane of the damage zone then it is apparent that

$$\dot{u} = \dot{\delta}/2 \tag{4.53}$$

At this stage of the analysis we still have two unknowns ($\dot{a}$ and δ_t) in what is essentially one equation. However, (as in all the work presented here) we are assuming small scale damage (we will determine the validity of this assumption later). This assumption implies that the remote field is not influenced by the damage zone, and so by using the path independence of C^* we can relate the conditions at the crack tip to those in the far field and in this way obtain an expression for the crack tip opening displacement rate, δ_t. It is important to remember that when determining C^* in a damaging/damaged material we must ensure that the integral is evaluated outside of the damage zone as the integral is not path independent if the contour of integration crosses damaged material (this is proved in Appendix 4). C^* was defined in equation (1.16) as

$$C^* = \oint_\Gamma \left(\overline{W} dx_2 - \tilde{T} \frac{d\dot{u}_i}{dx_1} ds \right) \qquad (4.54)$$

Now because we are implicitly assuming a Dugdale type strip model the term in dx_2 is zero and so by combining equations (4.48) and (4.54) and integrating around the outside of the damage zone we find

$$C^* = m \dot{\delta}_t \int_0^1 \sigma (1-\overline{x})^{m-1} d\overline{x} \qquad (4.55)$$

Substituting for the stress σ from equation (4.52) gives

$$C^* = \frac{\dot{\delta}_t^2 \sigma_0 m A_0}{3 \lambda \phi_0 \dot{e}_0} \qquad (4.56)$$

where

$$A_0 = \int_0^1 (1-\overline{x})^{2m-1} \ln \left(\frac{1}{F_1 + (F_2 - F_1)(1-\overline{x})^{m+1}} \right) d\overline{x} \qquad (4.57)$$

A plot of how A_0 varies with F_2 assuming $F_1 = 0$ is given in Figure 4.5.

Now by combining equations (4.56) and (4.50) we arrive at an expression for the crack growth rate resulting from the prescribed displacement rate field. If we assume a linear variation of displacement rate with position, ie. m = 1, then

$$\dot{a} = \frac{3R}{8\lambda (F_2 - F_1)} \left[\frac{3C^* \lambda \phi_0 \dot{e}_0}{A_0 \sigma_0} \right]^{\frac{1}{2}} \qquad (4.58)$$

or, in nondimensional form,

$$\overline{\dot{a}} = \frac{3\sqrt{3}}{8(F_2 - F_1)} \left(\frac{\phi_0}{m \overline{\lambda} A_0} \right)^{\frac{1}{2}} \overline{R} \qquad (4.59)$$

It is significant to note that using different values of the parameter m does not

change the functional form of this expression, it only affects the preceding constant.

Equation (4.59) is quite sensitive to the term $F_2 - F_1$, this is understandable as it represents the void growth that is required before the crack can advance by an amount 2λ. The area fraction at nucleation, F_1, is likely to be small, therefore $F_2 - F_1$ is approximately equal to F_2. At first sight it might be assumed that a value of $F_2 = 1$, representing failure by void coalescence, would be reasonable. However, the model presented above ignores the possibility of localised necking in the ligament of material between the voids which would, in most practical cases, result in an F_2 value significantly less than unity.

By comparing equations (4.19), (4.31) and (4.59) we can see the way that the dependence of the creep crack growth rate on the damage zone size varies as the material evolves varies from being initially constrained, through intermediate linear behaviour to unconstrained behaviour, ie. in each of these regimes

Constrained
$$\overline{\dot{a}} \propto \overline{R}^{-\frac{n+2}{n+1}}$$
(4.60)

linear
$$\overline{\dot{a}} \propto \overline{R}$$
(4.61)

and unconstrained
$$\overline{\dot{a}} \propto \overline{R}^{-\frac{n}{n+1}}$$
(4.62)

It is interesting to note that the strength of the power law dependence of the crack growth rate on $\overline{R}$ decreases by $1/(n+1)$ at each step from constrained to linear to unconstrained. The values of $\overline{R}$ and ϕ_0 over which the three models are valid may be seen from Figures 4.6a and c. In these Figures n is taken as 1.0, implying $f_3 = \pi/3$, and the volume fraction at nucleation is taken as zero. A volume fraction at failure, F_2, of 0.3 is assumed, which from Figures 4.2 and 4.5 gives $G(F) = 0.308$ and $A_0 = 1.1$. If R is assumed to be on the limit of small scale damage then $\overline{R}$

$\approx 1/20\pi$. The value of $\bar{\lambda}$ is determined as follows

$$\bar{\lambda} \equiv \frac{\lambda}{\chi} \approx \frac{\lambda}{\pi a} \qquad (4.63)$$

From equation (A3.10)

$$\lambda = \frac{l}{\sqrt[3]{6\pi\phi_0}} \qquad (4.64)$$

If the damage zone is of a fixed size, say 10 grains, then $R/l = 10$ and therefore

$$\bar{\lambda} = \frac{1}{200\pi\sqrt[3]{6\pi\phi_0}} \qquad (4.65)$$

which means that the constrained model is a function of $\phi_0^{1/3}$ and the linear model is a function of $\phi_0^{2/3}$. We can see from Figure 4.6a, for the case of $F_2 = 0.3$, that very high values of ϕ_0, which means many voids, are required for the crack growth rate to approach the full constrained value and that the full solution for all practical values of ϕ_0 is unconstrained behaviour at low values of ϕ_0 and linear behaviour for higher values. By equating equations (4.19), (4.31) and (4.59) we find that the transition from unconstrained to intermediate behaviour occurs at $\phi_0 = 70$ and from intermediate to constrained behaviour at $\phi_0 = 5160$; which represent l/λ values of about 11 and 46 respectively. Voids in ceramic materials often only occur at triple grain junctions which means that the void spacing is of the order of the grain size, ie. $l/\lambda \approx 2$. In metals, however, cavitated grain boundaries usually contain numerous voids which would indicate that the unconstrained model would tend better to describe the behaviour of ceramics while the intermediate model would be more appropriate for metals.

When the steady state crack growth rate is plotted as a function of $\bar{R}$

(Figure 4.6c) we can see that the full solution tends towards the unconstrained result with increasing damage zone size, a result that is in agreement with Thouless's observation, as is the general tendency for the crack growth rate to increase with increasing ϕ_0.

We can also see that both Figures 4.6a and c indicate that the intermediate linear model gives a better bound to the crack growth rate for the chosen combination of parameters, listed above.

4.7   Validity of the intermediate model.

The assumption in the preceding section that the displacement rate displays some form of variation through the damage zone would seem a natural one, if only for the fact that a *constant* rate, implying a uniform stress state, would seem unphysical. We can test the validity of our assumption of a displacement rate field of the form given in equation (4.48) by comparing it with the displacement rate field in the model of Thouless et. al.   In Thouless' model the form of the displacement rate field is not given explicitly, it is, however implied and can be determined by back-calculating from the stress field, which is given. This is done in Appendix 5 and it can be seen from Figure 4.7a that the displacement rate implied by Thouless' constrained model for the case of $l/\lambda = 20$ can be well approximated by

$$\dot{\delta} = 1.4 \, (1-\bar{x})^{0.7} \qquad\qquad (4.66)$$

and Figure 4.7b shows that for the case of $l/\lambda = 5$ a good approximation to the field is

$$\dot{\delta} = 0.7 \, (1-\bar{x})^{2.3} \qquad\qquad (4.67)$$

As has already been demonstrated l/λ is directly related to ϕ_0 and so is also

a measure of the degree of constraint in the damage zone. We can see from Figures 4.7a and 4.7b that a reduction in the constraint from $l/\lambda = 20$ to $l/\lambda = 5$ results in a change in the implied displacement field from the 'convex' field of equation (4.66) to the 'concave' field of equation (4.67). The obvious implication being that at some intermediate value of l/λ the behaviour will be approximately linear and that the crack growth rate will be approximated by equation (4.59) with $m = 1$.

Thus we can see that we have developed a model that when coupled with the constrained solution has general applicability. The choice of an appropriate m value together with the ability to specify ϕ_0 means that the two models can be used to describe creep crack growth over a wide range of combinations of $\overline{R}$, ϕ_0 and F_2. The model also has significant advantages over Thouless' in that the use of $\overline{R}$ means that the damage zone size is not prescribed and the model is not restricted to linear viscous behaviour.

4.8   Comparison of intermediate model with experimental results.

We will now compare the predictions of the intermediate model with some experimental data from the literature.

Thouless et. al[35]. present some unpublished data due to Blumenthal on crack growth in alumina; these data are reproduced in Figure 4.8. Using the material properties specified by Thouless we can plot equation (4.59) on these data. From this we can see that this equation is a good fit to the data, if we assume a damage zone size of 4.5×10^{-6}m. This value of R seems reasonable, though it would be unwise to read too much into this result as the exact value of R is unknown. In section 4.12 we argue that the damage zone size is not a material property like Young's modulus, fixed and independent of loading and geometry, we believe it to

be a variable paramter whose size is dictated by these very factors.

4.9   Presentation of crack growth models on creep crack growth map.

We will now demonstrate how the creep crack growth maps developed in the previous chapter may be used to determine the range of validity of the creep crack growth models developed earlier. Initially we will consider growth within that region of the creep crack growth map where C* is the controlling parameter. We will then consider the K controlled limit and demonstrate that, even though they were derived explicitly using C*, the models presented earlier may be easily modified for the case of K control. It will then be demonstrated that the map may be used to determine the range of applicability of the model in the K controlled limit.

C* controlled growth.

If we first consider growth entirely within the region of C* control and if we continue with our assumption of a displacement rate field of the form

$$\dot{\delta} = \dot{\delta}_t (1 - x/R)^m \qquad (4.68)$$

then it was shown in equation (4.55) that C* could be written in simplified form as

$$C^* = m \, \dot{\delta}_t \int_0^1 \sigma \, (1 - \bar{x})^{m-1} \, d\bar{x} \qquad (4.69)$$

Assuming for simplicity a linear variation of displacement rate through the damage zone, ie. m = 1, we arrived at the result that

$$\bar{a} = \frac{3\sqrt{3}}{8 \, (F_2 - F_1)} \left(\frac{\phi_0}{\bar{\lambda} \bar{A}_0} \right)^{\frac{1}{2}} \bar{R} \qquad (4.70)$$

ie. $$\bar{a} = c_1 \bar{R}$$ (4.71)

If we assume that $c_1 = 6.28 \times 10^5$ and $\bar{R} = 1/20\pi$ we can plot equation (4.71) on the map of Figure 4.9. The above mentioned normalising values are entirely contrived and are not meant to represent a specific real material, they have been chosen solely to demonstrate how the model can be represented on the map. In this instance we see that the model is valid for normalised reference stresses less than about 7×10^{-3}.

K controlled growth.

If we now consider creep crack growth wholly within the region of K control then by analogy to equation (4.69) we can see that J may be given by

$$J = \delta_t \int_0^1 \sigma \, d\bar{x}$$ (4.72)

If we apply the same principle as used to determine the above result for the C* limit, ie. making use of the path independence of, in this instance, the J integral we can equate equation (4.72) which determines J at the crack to its far field plane strain value, given by

$$J = \frac{K^2 (1 - v^2)}{E}$$ (4.73)

As usual the term $(1-v^2)$ is deleted for plane stress.

Now it is clear from the derivations of equations (4.19), (4.31) and (4.59) that the stress field ahead of the crack is modified by the presence of damage, which is itself a function of position within the damage zone. We may express this in a very general way as

$$\sigma = \sigma_0 \left(\frac{\dot{u}}{\dot{u}_0}\right) f(\delta) \tag{4.74}$$

Where $\dot{u}_0$ is a characteristic displacement rate. The displacement rate perpendicular to the damage zone, $\dot{u}$, on either side of the zone is, of course,

$$\dot{u} = \dot{\delta}/2 = \frac{\dot{\delta}_t}{2} (1-x/R) \tag{4.75}$$

Combining equations (4.72), (4.74) and (4.75) we find

$$J = \frac{\dot{\delta}_t \delta_t \sigma_0}{2\dot{u}_0} \int_0^1 f(\delta) (1-\bar{x}) \, d\bar{x} \tag{4.76}$$

The crack tip opening displacement rate, $\dot{\delta}_t$, is not generally a known quantity or easily measured. It can however, be expressed in terms of the crack tip opening displacement, δ_t, which can be measured. We can see from equation (4.75) that

$$\frac{d\dot{u}}{dx} = -\frac{\dot{\delta}_t}{2R} \tag{4.77}$$

If the crack grows at a constant rate then the critical crack tip opening displacement, δ_t, is simply

$$\delta_t = \int_0^{t_R} \dot{\delta} \, dt \tag{4.78}$$

where t_R is the time for an element to traverse the damage zone. Recalling that

$$\frac{dx}{dt} = -\dot{a} \tag{4.79}$$

we see that

$$\delta_t = \frac{\dot{\delta}_t R}{2\dot{a}} \tag{4.80}$$

If we now combine equations (4.71) and (4.80) we find

$$J = \frac{\delta_t^2 \sigma_0 \dot{a}}{\dot{u}_0 R} \int_0^1 f(\delta)(1-\bar{x}) \, d\bar{x}$$
(4.81)

Equating this result with equation (4.73) we see that

$$\dot{a} \propto K^2$$
(4.82)

Recalling equation (2.18)

$$K^2 = \sigma_0^2 \chi$$
(4.83)

leads to the final result that

$$\bar{a} = c_2 \frac{\sigma_0}{E} \frac{\bar{R}}{\delta_t^2} \bar{u}_0$$
(4.84)

If we assume this time that $c_2 = 2.61$, that $\bar{R} = 1/20\pi$; $\bar{u} = 100$ and $\bar{\delta}_t = 5 \times 10^{-5}$ we can also plot equation (4.84) on the map of Figure 4.9. As before these figures are not representative of a specific real material, they merely serve to illustrate the way in which the map may be used to determine the range of validity of equation (4.84), which we can see would be valid for normalised crack velocities greater than about 10^7. Thus By comparing the positions of equations (4.71) and (4.84) on Figure 4.9 we can readily see the range of validity of each of the models. We can see that at high stresses the K controlled model of equation (4.84) is appropriate but at lower stresses the rate of creep is too high and equation (4.71) gives a better description of component response.

We may extend this consideration of the K controlled regime by considering the unconstrained limit in which the stress field is given by the K field. The elastic stress field is given by

$$\sigma_{22} = \frac{K_I}{\sqrt{2\pi x}} \qquad (4.85)$$

If we combine this stress field with equations (4.23) and (4.24) we obtain the result

$$\bar{a} = \frac{3\phi_0 \bar{R}^{-\frac{1}{2}}}{2\sqrt{2\pi}\ G(F)} \qquad (4.86)$$

which is the same as equation (4.31) for n = 1 as the creep and elastic stress fields are identical for the linear viscous case.

4.10 Small scale damage.

We will now consider the range of validity of the assumption of small scale damage, an assumption implicit in all the work in this thesis.

From a consideration of the change in the surface energy of a void with principal radii r_1 and r_2 one can determine that the excess chemical potential, $\Delta\mu$, of an atom of volume Ω, on the surface of the void, is given by

$$\Delta\mu = -\gamma\Omega\left(\frac{1}{r_1} + \frac{1}{r_2}\right) \qquad (4.87)$$

where γ is the surface energy. When $r_1 = r_2 \to \infty$, $\Delta\mu = 0$, therefore atoms on the surface of a void are at a lower potential than an atom on a flat surface. Matter always tends towards as low a potential as possible and so, if the temperature is sufficiently high, atoms will diffuse from a flat surface, or other region of higher potential, down the potential gradient, into the void. This influx of material into the void must result in a decrease in the volume of the void and therefore a reduction in r_1 and r_2. This means that the potential of the void drops even further increasing the rate of diffusion which is proportional to the potential gradient. The end result of this is that eventually the void 'fills up' and vanishes. This

phenomenon is commonly called sintering. From a consideration of this process it is easy to see that once nucleated, and provided that the temperature is high enough, a void will begin immediately to sinter away. Thus void growth can only occur by diffusion if a tensile stress across the void (which for analytic tractability we will assume to be spherical with $r_1 = r_2 = r$) exceeds the capillarity (or sintering) stress, σ_γ given by

$$\sigma_\gamma = \frac{2\gamma}{r} \tag{4.88}$$

causing the potential on the grain boundary to drop below $-2\gamma\Omega/r$. It also follows from this that for a given stress voids can only grow if their radius on nucleation (and therefore their area fraction) exceeds a critical value, ie. $2\gamma/\sigma$.

The HRR stress field was defined in equation (3.3) as

$$\sigma_{ij} = \left(\frac{\sigma_0^n C^*}{\dot{\epsilon}_0 I_n r}\right)^{\frac{1}{n+1}} \tilde{\sigma}_{ij}(\theta) \tag{4.89}$$

where, for a plane strain crack, the stress directly ahead of the crack is given by recalling equation (4.32)

$$\sigma_{22}(0) = \frac{2}{\sqrt{3}} + \left(\frac{n-1}{n}\right)^2 \frac{\pi}{\sqrt{3}} \tag{4.90}$$

This means that equation (4.89) can be rewritten in the form

$$\frac{\sigma_{22}}{\sigma_0} = \left(\frac{C^*}{\dot{\epsilon}_0 \sigma_0 \chi} \frac{\chi}{I_n r}\right)^{\frac{1}{n+1}} \left[\frac{2}{\sqrt{3}} + \left(\frac{n-1}{n}\right)^2 \frac{\pi}{\sqrt{3}}\right] \tag{4.91}$$

Now, of course, the product $\dot{\epsilon}_0 \sigma_0 \chi$ is approximately equal to C^*, and if we recall equation (3.4)

$$I_n = \frac{n+1}{n} \pi \qquad (4.92)$$

and that χ is approximately equal to πa, we see that equation (4.91) reduces to

$$\frac{a}{r} = \left(\frac{\sigma_{22}}{\sigma_0}\right)^{n+1} \frac{n+1}{n \left[\frac{2}{\sqrt{3}} + \left(\frac{n-1}{n}\right)^2 \frac{\pi}{\sqrt{3}}\right]^{n+1}} \qquad (4.93)$$

Now at the far edge of the damage zone where r = R, σ_{22} is equal to the capillarity stress at nucleation, $\sigma_{\gamma n}$, which is related to the area fraction of the nucleated void, f_1, by

$$\sigma_{\gamma n} = \frac{2\gamma}{l\sqrt{f_1}} \qquad (4.94)$$

For the condition of small scale damage to be met we require R $\ll$ a. If we assume as before that the limit of small scale damage is given by a = 20R we can determine the reference stress, below which the damage will be small scale, as

$$\sigma_0 \leq \frac{2\gamma}{l\sqrt{f_1}} G(n) \qquad (4.95)$$

where G(n) is a dimensionless function of n given by

$$G(n) = \left(\frac{20n}{n+1}\right)^{\frac{1}{n+1}} \left[\frac{2}{\sqrt{3}} + \left(\frac{n-1}{n}\right)^2 \frac{\pi}{\sqrt{3}}\right] \qquad (4.96)$$

This function G(n) is quite insensitive to the value of n, and γ and l can be measured, the only term about which there is some uncertainty is f_1 and the result is not particularly sensitive to this term either, by virtue of the ½ power in equation (4.95). We can obtain a feel for the magnitude of this limiting stress below which damage is small scale by inserting the appropriate data for alumina in equation (4.95). For this material n is approximately 1[4] and γ = 2 Nm⁻¹. If we assume one

void per grain then l is typically about $3 \times 10^{-6} m$[22]; taking $f_1 = 10^{-3}$ gives a limiting stress of $77 Nmm^{-2}$. Cannon and Langdon[4] have reviewed the literature on the creep testing of alumina and this level of stress would appear to be, broadly speaking, in the middle of the range commonly used for this material.

This would indicate that over a practically useful range of stresses the assumption of small scale damage is reasonable.

4.11   The effect of the capillarity stress.

The approximate void growth law of equation (4.21),

$$\frac{dv}{dt} = \frac{2 \pi D_b \delta_b \sigma \Omega (1-f)}{kT \ln\left(\frac{1}{\sqrt{f}}\right)} \qquad (4.97)$$

does not include the effect of the capillarity stress mentioned earlier. The full equation[9]

$$\frac{dv}{dt} = \frac{2 \pi D_b \delta_b \Omega (1-f)}{kT} \left[\frac{\left(\sigma - \frac{2\gamma}{r}\right)(1-f)}{\ln\left(\frac{1}{\sqrt{f}}\right) - \frac{3}{4} + f\left(1 - \frac{f}{4}\right)} \right] \qquad (4.98)$$

does include this effect but its relative magnitude and hence its importance is not obvious.

The capillarity stress (ie. sintering) has been specifically neglected in the creep crack growth models developed so far in this thesis. In this section we will investigate the validity of this assumption by evaluating the change in the magnitude of C^*, determined by integration around the outside of the damage zone, when the effect of the capillarity stress is first ignored and then included. Assuming again a displacement rate field of the form

$$\dot{\delta} = \dot{\delta}_t (1 - x/R)^m \qquad (4.99)$$

we found that C^* was given by equation (4.55) as

$$C^* = m \dot{\delta}_t \int_0^1 \sigma (1 - \bar{x})^{m-1} d\bar{x} \qquad (4.100)$$

and σ can be obtained from equation (4.52) as

$$\sigma = \frac{\dot{\delta}_t \sigma_0 (1 - \bar{x})^m}{3 \lambda \phi_0 \dot{e}_0} \ln \left(\frac{1}{F_1 + (F_2 - F_1)(1 - \bar{x})^{m+1}} \right) \qquad (4.101)$$

and therefore

$$C^* = \frac{m \dot{\delta}_t^2 \sigma_0}{3 \lambda \phi_0 \dot{e}_0} \int_0^1 (1 - \bar{x})^{2m-1} \ln \left(\frac{1}{F_1 + (F_2 - F_1)(1 - \bar{x})^{m+1}} \right) d\bar{x} \qquad (4.102)$$

If we now consider the effect of sintering we can see that as the capillarity stress tries to 'close up' the damage zone the stress required to produce the displacement rate field of equation (4.99) is simply the stress, given by equation (4.101), plus the capillarity stress, ie. $\sigma + 2\gamma/r$ (assuming spherical voids). The void radius and the volume fraction are related by

$$r = \lambda F^{1/3} \qquad (4.103)$$

and the volume fraction, which is itself, of course, a function of position, was given by equation (4.51) as

$$F = F_1 + (F_2 - F_1)(1 - \bar{x})^{m+1} \qquad (4.104)$$

To simplify the analysis we shall assume that the area fraction at nucleation, $F_1 = 0$; that at failure $F_2 = 1$ and that $m = 1$. Therefore the capillarity stress as a function of position within the damage zone is given by

$$\sigma_\gamma = \frac{2\gamma}{\lambda (1-\bar{x})^{2/3}} \qquad (4.105)$$

and so C^* is now equal to that given by equation (4.102) plus the additional term ΔC^* given by

$$\Delta C^* = \frac{2\gamma \dot{\delta}_t}{\lambda} \int_0^1 (1-\bar{x})^{4/3} d\bar{x} = \frac{6\gamma \dot{\delta}_t}{7\lambda} \qquad (4.106)$$

Bearing in mind the simplifying assumptions made above, C^* can now be written as

$$C^* = \frac{\dot{\delta}_t^2 \sigma_0}{3\lambda \phi_0 \dot{e}_0} \int_0^1 (1-\bar{x}) \ln\left(\frac{1}{(1-\bar{x})^2}\right) d\bar{x} = \frac{\dot{\delta}_t^2 \sigma_0}{6\lambda \phi_0 \dot{e}_0} \qquad (4.107)$$

Obviously ΔC^* has a finite value and so (rigorously) cannot be neglected. However if $\Delta C^*/C^*$ is small then sintering may be neglected without significantly affecting the equivalence of the near and far field values of C^*.

$$\frac{\Delta C^*}{C^*} = \frac{36\gamma \phi_0 \dot{e}_0}{7\dot{\delta}_t \sigma_0} \qquad (4.108)$$

Now from equation (4.80)

$$\dot{\delta}_t = \frac{2\dot{a}\delta_t}{R} \qquad (4.109)$$

Taking a limiting value of $\Delta C^*/C^* < 0.1$ we find that the capillarity stress may be neglected provided that

$$\frac{18\phi_0}{7} \frac{\gamma}{\delta_t \sigma_0} \frac{\bar{R}}{\bar{a}} \leq \frac{1}{10} \qquad (4.110)$$

As in the previous section a feel for the size of this term, and hence whether it is reasonable to neglect sintering, can be obtained by inserting appropriate values in

this expression. Considering alumina again, $\gamma = 2\text{Nm}^{-1}$ and a value of σ_0 of 10^8Nm^{-2} seems reasonable. If the material is on the limit of small scale damage then $\overline{R} = 1/20\pi$ and we can see from the creep crack growth map of Figure 3.10 that a value of $\overline{a}$ of 10^0 is reasonable for alumina. Thouless' model[35] described earlier considers a degree of constraint represented by $l/\lambda = 20$, it can be seen from equation (A3.10) that this is equivalent to a ϕ_0 value of 424. This just leaves the crack tip opening displacement δ_t, for which Blumenthal and Evans[88] indicate that a reasonable minimum value is of the order of $5\mu\text{m}$. Inserting these values in equation (4.110) gives a value of 0.07 ie. ignoring the effect of sintering results in a difference between C^* in the far field and C^* determined at the crack tip of 7%. This is less than 10% which indicates that for this combination of properties the effect of sintering may reasonably be neglected. One can also see however that halving the stress may result in the effect of sintering becoming too large to ignore. This is what one would intuitively expect although the exact effect will of course depend on the relationship between σ_0 and the other terms.

4.12   Critical strain accumulation as a criterion for void nucleation.

As was mentioned in Chapter one there is experimental evidence[13,14] that up to 90% of the failure time of creep specimens is time required for voids to nucleate and that voids may only nucleate in an element of material after that element has undergone a critical plastic strain.

By considering a simple model of this process we can use this requirement for a critical plastic strain for void nucleation to determine the damage zone size. We can then combine this result with those of the void growth models, described earlier, to determine the relationship between the void growth rate and the loading parameter ie. C^*.

As a creep crack grows into a material the stress system acting on any element of that material, a distance x from the crack tip, changes. If we continue to take the crack tip as our reference point we can consider the element as moving towards the crack tip and if the damage zone is small we can reasonably assume steady state conditions and take both the crack velocity, $\dot{a}$, and C^* as being constant.

Cocks and Ashby[73] have demonstrated that the strain rate, $\dot{\epsilon}$, at distance x from a crack tip in a creeping solid is given by

$$\dot{\epsilon} = \left(\frac{\dot{\epsilon}_0}{I_n \sigma_0^n}\right)^{\frac{1}{n+1}} \left(\frac{C^*}{x}\right)^{\frac{n}{n+1}} \dot{\epsilon}(\theta) \qquad (4.111)$$

Noting that for a plane stress crack $\dot{\epsilon}(\theta)$ has a maximum value of unity when $\theta = 0$ we may write

$$\dot{\epsilon} = B C^{*\frac{n}{n+1}} x^{-\frac{n}{n+1}} \qquad (4.112)$$

If we denote the distance from the crack tip at which creep strains become appreciable, by R_s then

$$x = R_s - \dot{a}t \qquad (4.113)$$

where t is the time taken for the element of material to 'move' from R_s to the point x from the crack tip. Remembering that we are assuming C^* and $\dot{a}$ to be constant we can see that

$$\int_{\epsilon_{R_s}}^{\epsilon_n} d\epsilon = B C^{*\frac{n}{n+1}} \int_0^{(R_s - R)/\dot{a}} (R_s - \dot{a}t)^{-\frac{n}{n+1}} dt \qquad (4.114)$$

where the ϵ_{R_s} and ϵ_n are the accumulated strains at R_s and at nucleation respectively. Integrating, we find that

$$\epsilon_n - \epsilon_{R_s} = \frac{BC^{*\frac{n}{n+1}}(n+1)}{\dot{a}} \left(R_s^{\frac{1}{n+1}} - R^{\frac{1}{n+1}} \right) \qquad (4.115)$$

We are now left with the problem of deciding at what distance from the crack tip the creep strain becomes appreciable. From equation (4.112) $\dot{\epsilon} = 0$ at $x = \infty$; however, integrating up from $x = \infty$ to a finite value gives an infinite strain at that point. Clearly this is not the case and in fact equation (4.112) is only an approximate solution and there will, in practice, be a finite value at which $\epsilon_{Rs} = 0$.

For larger values of n, $R_s^{1/n+1}$ becomes relatively insensitive to the precise value of R_s. Therefore if we arbitrarily choose a value for R_s (unity, say) we can obtain a result which, though not exact, displays the main features of the true solution. Of course, by definition, $\epsilon_{Rs} = 0$, and so we may write

$$\epsilon_n = \frac{BC^{*\frac{n}{n+1}}(n+1)}{\dot{a}} \left(1 - R^{\frac{1}{n+1}} \right) \qquad (4.116)$$

From this we can see that if the nucleation strain is small then $R \rightarrow 1$ (ie. $R \rightarrow R_s$) and consequently cavitation is extensive, occurring over a much larger 'area' than strain accumulation leading to nucleation. Void growth is then the rate controlling mechanism. Conversely, if the nucleation strain is large then $R \rightarrow 0$ and there is only limited cavitation. Void growth therefore only occurs over a very small distance and consequently nucleation is the rate controlling mechanism.

For the case of nucleation controlling the crack growth we may rearrange equation (4.116) to find

$$\dot{a} = \frac{2BC^{*\frac{1}{2}}}{\varepsilon_n} (1 - R^{\frac{1}{2}}) \qquad (4.117)$$

Now in the steady state this crack growth rate must be equal to that predicted by the void growth models, so if we equate this expression to that predicted by the model of equation (4.58) we find, in the linear viscous case

$$\frac{2BC^{*\frac{1}{2}}}{\varepsilon_n} (1 - R^{\frac{1}{2}}) = ARC^{*\frac{1}{2}} \qquad (4.118)$$

ie.
$$x^2 + bx - b = 0 \qquad (4.119)$$

where
$$x = R^{\frac{1}{2}} \qquad \text{and} \qquad b = \frac{2B}{A\varepsilon_n} \qquad (4.120)$$

Solving equation (4.119) leads to the result that

$$R^{\frac{1}{2}} = \sqrt{\frac{b^2}{4} + b} - \frac{b}{2} \qquad (4.121)$$

from which we can see that if b is large, ie. if the nucleation strain is small then R → 1 (that is R → R_s) and consequently cavitation is extensive, taking place over a much larger 'area' than that taken for the strain to accumulate. Void growth is then the rate controlling mechanism. Conversely, if b is small then R → b and there is only limited cavitation. Void growth and coalescence takes place within a small region and nucleation is the rate controlling process. Now

$$B = \left(\frac{\dot{\varepsilon}_0}{2\pi\sigma_0}\right)^{\frac{1}{2}} \qquad (4.122)$$

and from equation (4.58), assuming F_2 is small

$$A = \frac{3}{8\lambda F_2} \left[\frac{3\lambda \phi_0 \dot{e}_0}{A_0 \sigma_0} \right]^{\frac{1}{2}} \tag{4.123}$$

therefore $$b = \frac{16}{3\sqrt{2\pi}} \frac{F_2}{\epsilon_n} \left(\frac{A_0 \lambda}{3\phi_0} \right)^{\frac{1}{2}} \tag{4.124}$$

Consider the form of equation (4.124). As discussed earlier the volume fraction at failure, F_2, is likely to have a rather small range in most practical materials. When this is combined with the fact that A_0 increases as F_2 decreases (see Figure 4.5) it is apparent that the size of the void at failure has limited influence on the rate controlling mechanism.

Typical values for a ceramic material may be $F_2 = 0.3$, giving $A_0 \approx 1.0$; $l = 10^{-5}$ and $l/\lambda = 2$ ($\therefore$ from equation (A3.10) $\phi_0 = 0.424$). Inserting these values into equation (4.124) gives $b = 0.0013/\epsilon_n$. A nucleation strain of 0.1%, gives R = 0.4, which means that void growth occurs over 40% of R_s and nucleation over the remaining 60% and neither mechanism dominates.

Metals however usually have many cavities per grain boundary. If we therefore consider a metal which has the same values as above, except that $l/\lambda = 20$, say, we find R = 0.002. This implies that growth occurs over a very small region and that nucleation is the rate controlling mechanism, a result in qualitative agreement with the experiments of Goods and Nix[13] and Dyson[14] mentioned above and described in Chapter one.

In the limiting case of linear viscosity described above the damage zone size, R, is independent of the loading characterised by C*. However, it is clear that this is not the case for all values of n as the crack growth rate based on the nucleation criterion is itself a function of n (through C* to a variable power of n) while the

crack propagation rate based on void growth is independent of n (in the model considered here). Thus in order for 'continuity' of growth rate the damage zone is 'forced' to a size that is a function of the loading, and is not therefore, as implied in some models, a material property that may be prescribed regardless of the loading conditions.

4.13   Summary.

In this Chapter we have developed models for the limiting cases of fully constrained and unconstrained crack growth. However as a crack grows it cannot instantaneously switch from one form of behaviour to the other. To model the behaviour during the transition we prescribe a displacement field ahead of the crack and from this determine the stress field and hence the crack growth rate. This model assumes conditions of small scale damage and neglects sintering: the validity of both these approximations is demonstrated. The partially constrained model is compared with a model due to Thouless et. al.[35] and it is shown that if similar void growth laws are used the models give similar results. The model presented here has the advantage over Thouless' model, however, that it is more general; not being limited solely to linear viscous materials.

The crack growth rate from the intermediate model is combined with that based on a criterion of a critical strain for void nucleation. From this the regions of dominance of void growth and cavity nucleation are determined in a semi-quantitative manner. It is demonstrated that the size of the damage zone is a function of the applied loading and not a material property.
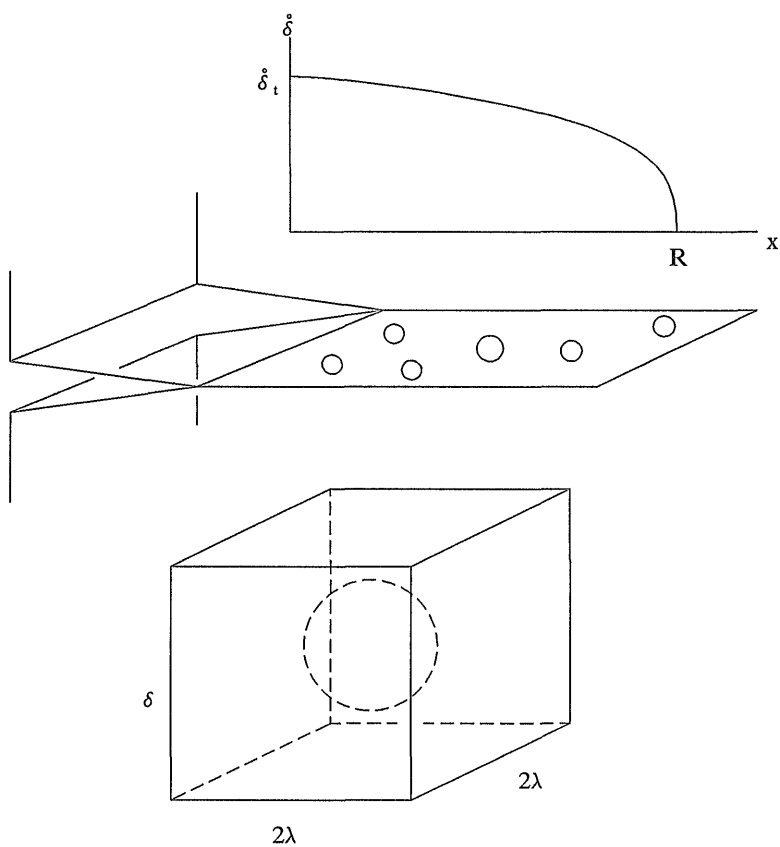
Figure 4.1. A damage zone of length R containing an array of voids, an average distance 2λ apart, is modeled by considering it to comprise several basic units of plan area $4\lambda^2$. At any instant in time the thickness perpendicular to the plane of the damage zone is δ. $\dot{\delta}$ is a function of position within the damage zone, x, and the increase in volume of the unit as it 'moves' towards the crack tip is entirely accommodated by an increase in volume of the void.
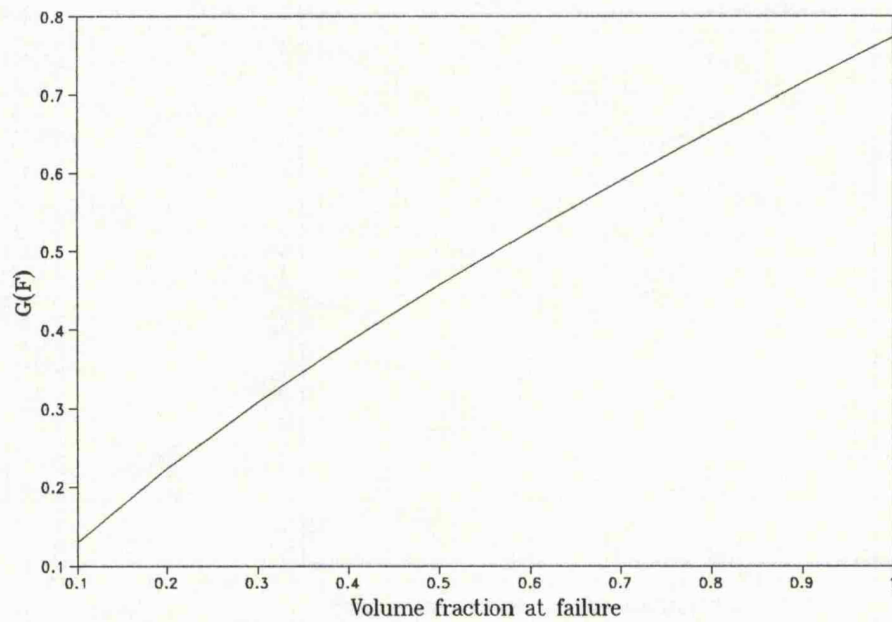
Figure 4.2. A plot of how the function G(F) varies with the volume fraction at failure, F_2, assuming a volume fraction at nucleation, F_1 of 0.
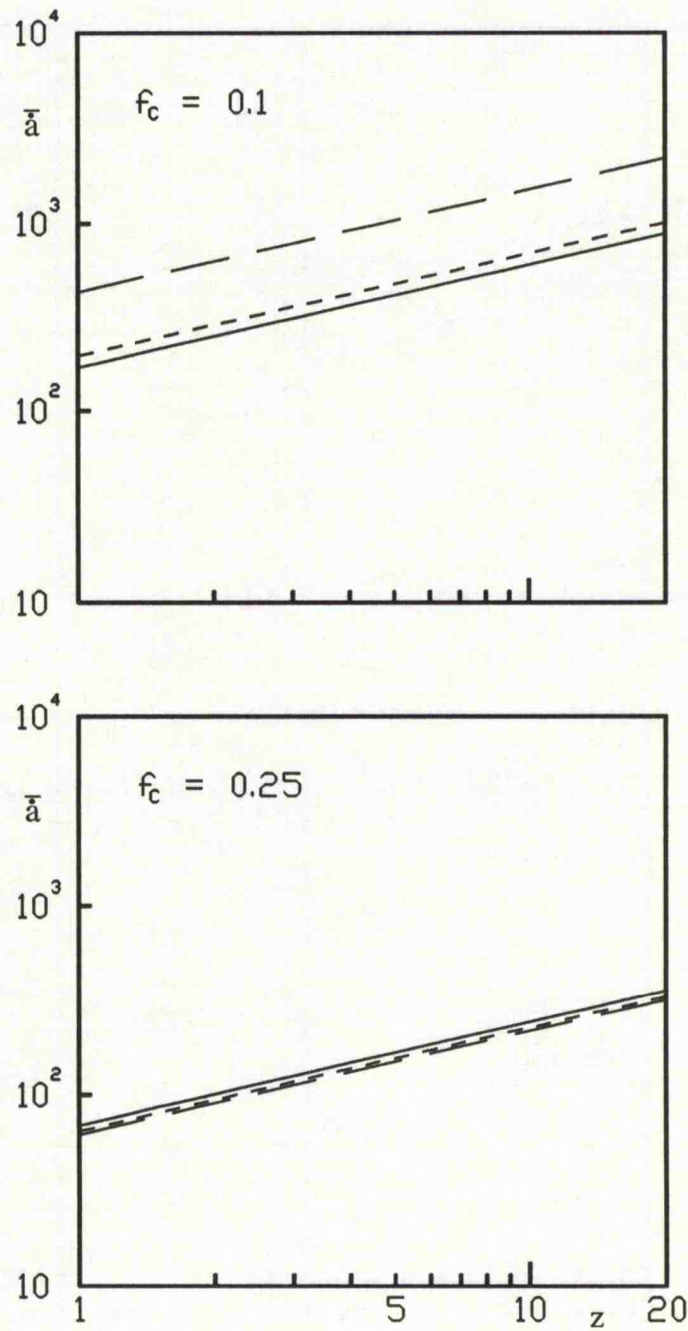
Figure 4.3a. Plots of normalised crack growth rate as a function of the damage zone size for two different values of the area fraction at failure, $f_c = 0.1$ and 0.25 (after Thouless et. al.[35]). In both plots l/λ is taken as 20. The solid line is the result due to Thouless; the longer dashed line is equation (4.31) with G(F) given by equation (4.29); the short dashed line is with G(F) given by equation (4.36). In Thouless' normalisation $\bar{a} = \eta \dot{a}/K\sqrt{l}$
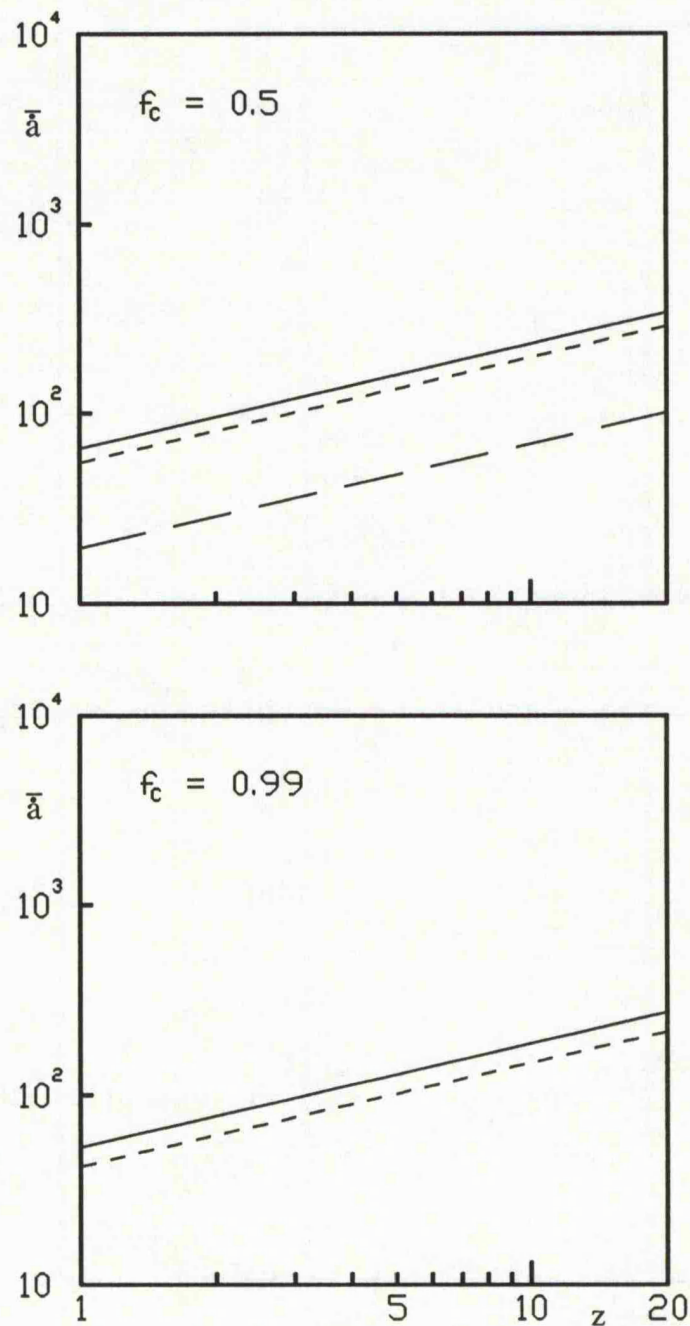
Figure 4.3b. Plots of normalised crack growth rate as a function of the damage zone size for $f_c = 0.5$ and 0.99. The longer dashed line is equation (4.31) with $G(F)$ given by equation (4.29) and the shorter dashed line is with $G(F)$ given by equation (4.36). By comparing this Figure with Figure 4.3a we can see that equation (4.29) is a reasonable approximation for small f_c but as f_c increases it becomes less accurate until when $f_c = 0.99$ equation (4.29) does not even appear on the graph. On the other hand, equation (4.36) remains a close fit for all values.
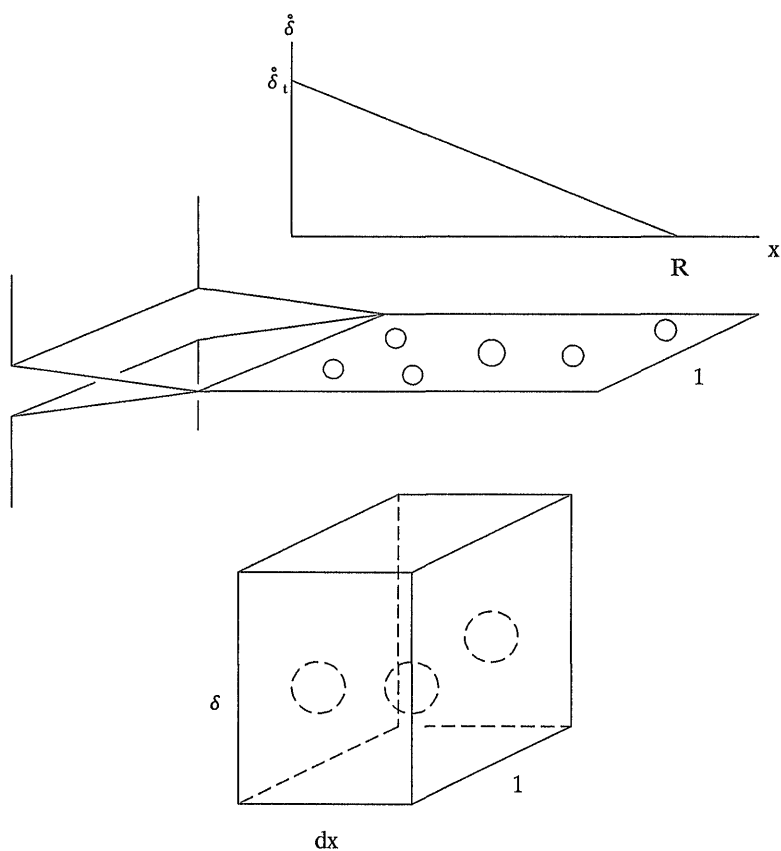
Figure 4.4. Void growth within a damage zone of length R is considered to occur so as to result in a linear variation of displacement rate through the damage zone. This process is modelled by considering the behaviour of a thin slice through the zone of unit width containing an arbitrary number of voids of mean separation 2λ. At any instant in time the thickness of this slice perpendicular to the plane of the damage zone is δ. The increase in volume of the unit as it 'moves' towards the crack tip is entirely as a result of the increase in volume of the void.
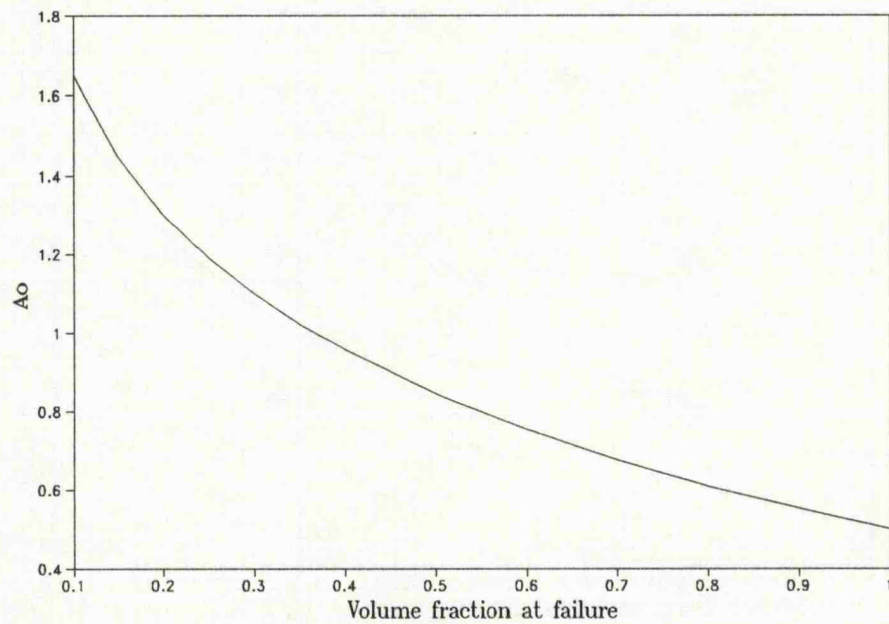
Figure 4.5. A plot of how the function A_0 varies with the volume fraction at failure, F_2, assuming a volume fraction at nucleation, F_1 of zero.
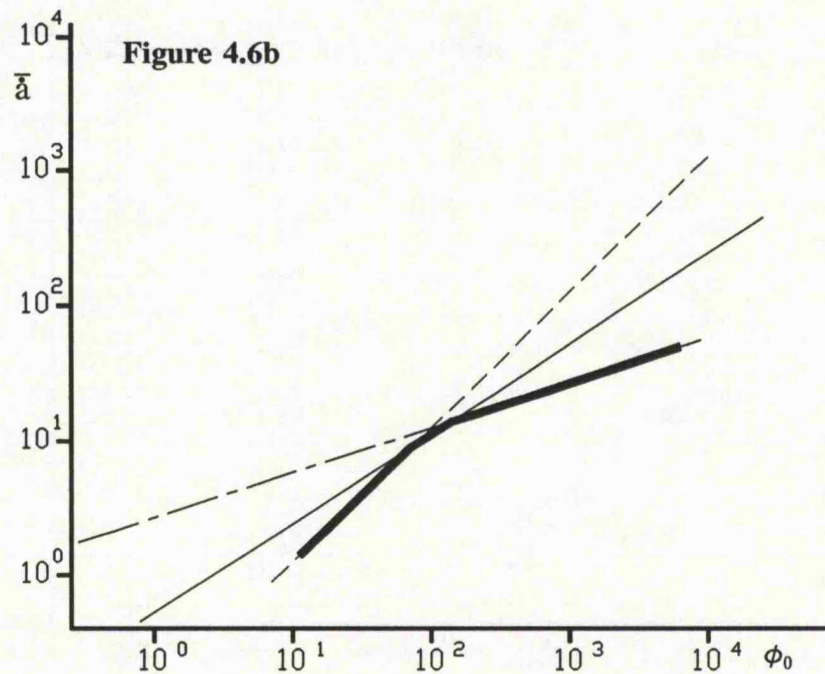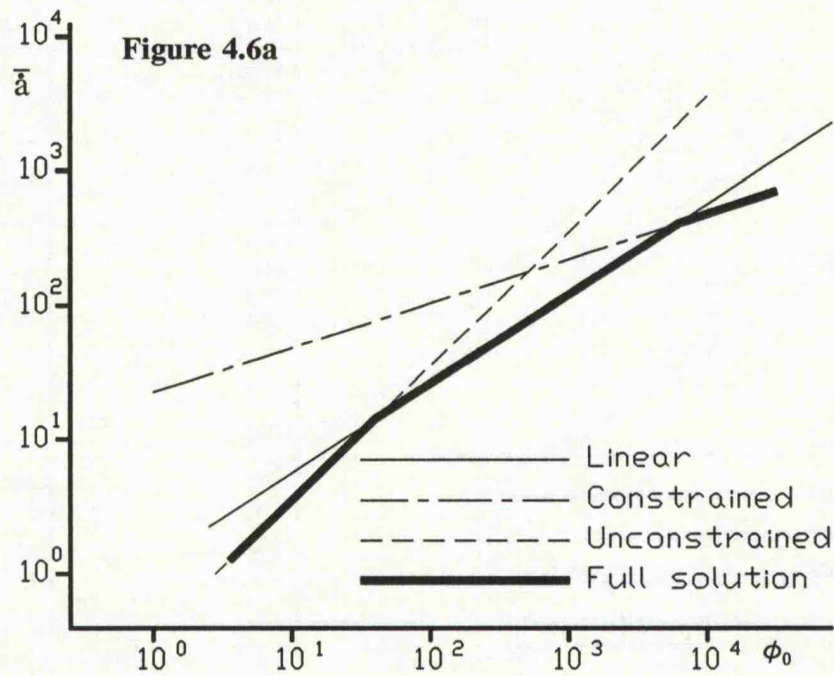
Figure 4.6a. Steady state crack growth rate as a function of ϕ_0 assuming $\overline{R}$ = $1/20\pi$ and F_2 = 0.3. Note that very high values of ϕ_0 are required for the crack growth rate to approach the full constrained value and that the full solution for all practical values is the unconstrained model at low ϕ_0 and the linear model for higher values.

Figure 4.6b. As Figure 4.6a but with F_2 = 0.8. Note that as the area fraction at failure, F_2, increases the range of ϕ_0 over which the linear model is applicable decreases.
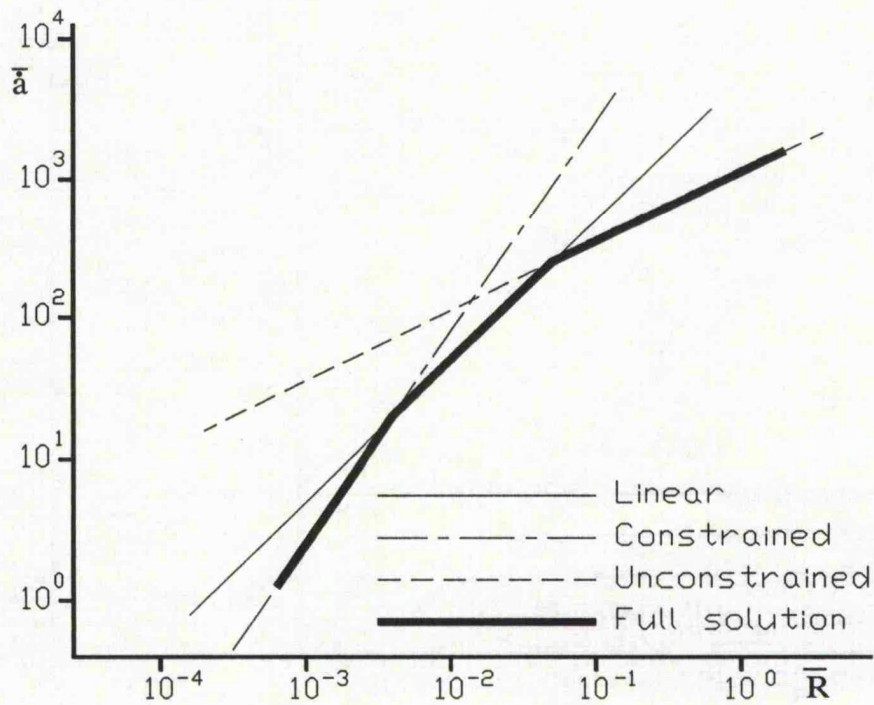
Figure 4.6c. A plot of how the crack growth rate increases with increasing damage zone size for $F_2 = 0.3$. Note that as $\overline{R}$ increases the crack growth rate approaches the unconstrained limit, a result in agreement with Thouless' model.
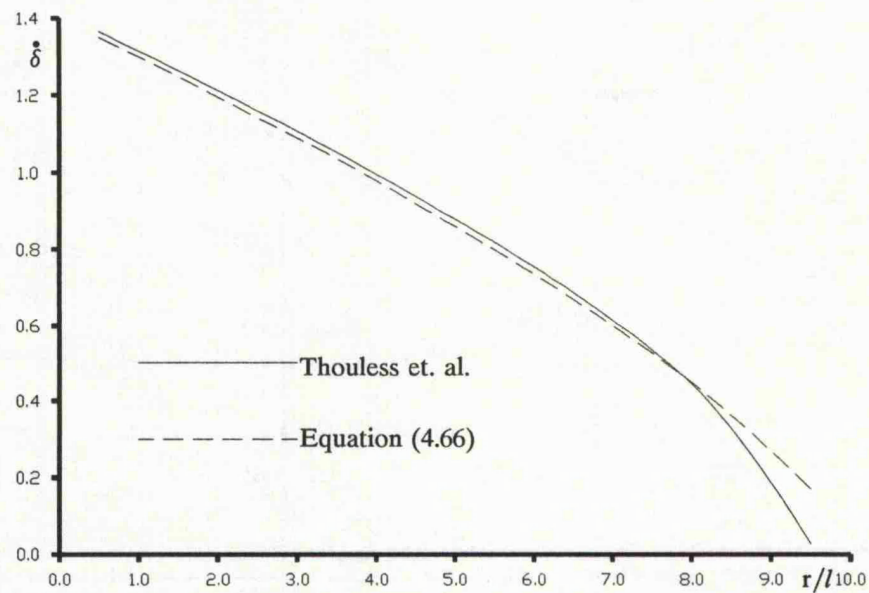
Figure 4.7a. Displacement rate fields ahead of a growing crack. The solid line represents the displacement rate implied by Thouless' model for the case of $l/\lambda = 20$, a damage zone of 10 grains and an area fraction at failure of 0.5. This result is well approximated by the partially constrained model with the variables defined in equation (4.66).
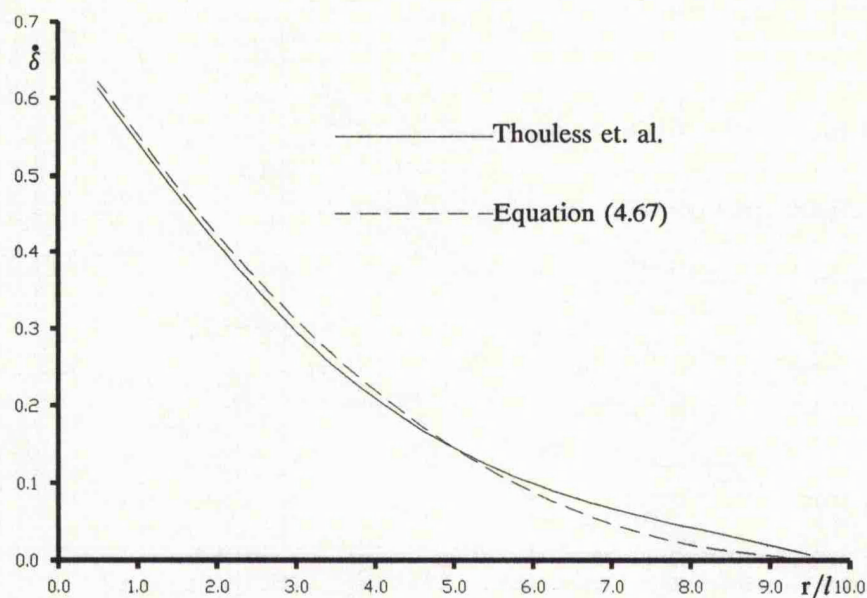
Figure 4.7b. The solid line is the displacement rate implied by Thouless' model for $l/\lambda = 5$, ie. a lesser degree of constrained. Again the damage zone is of 10 grains and the area fraction at failure is 0.5 This can also be well approximated by the partially constrained model, with the variables defined in equation (4.67).
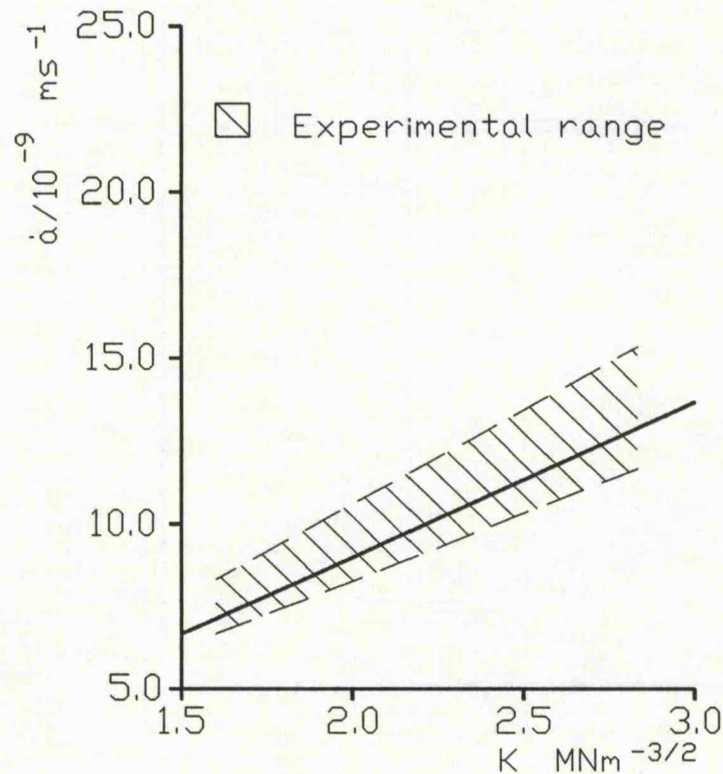
Figure 4.8 Crack growth data from Thouless et. al[35]. for alumina. The solid line represents equation (4.59), with the following parameters specified by Thouless: $l = 1.5 \times 10^{-6}$m, $F_2 = 0.125$, $l/\lambda = 5$. The following values have been shown to be applicable earlier: m = 2.3 (equation 4.67)), $A_0 = 1.5$ (Figure 4.5). We assume R $= 4.5 \times 10^{-6}$m.
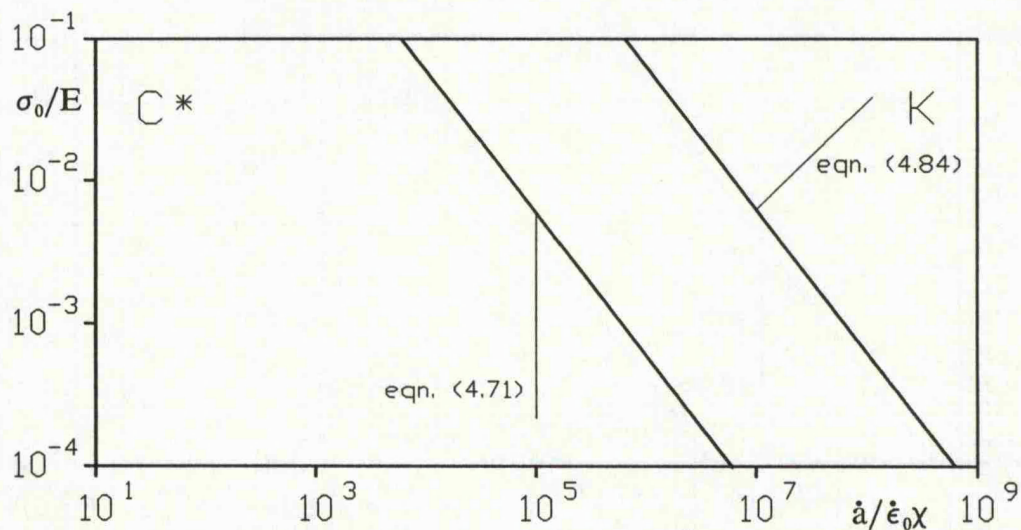
Figure 4.9. A creep crack growth map, assuming n = 9, showing the range of validity of crack growth models developed earlier for growth controlled by C* (equation (4.71)) and K (equation (4.84)).

CHAPTER FIVE: EXPERIMENTAL WORK

5.1   Introduction.

Before one can safely design with a new material one requires a sufficiently large database of the material's behaviour to enable reliable predictions to be made about a components in-service behaviour. The two basic testing techniques for obtaining such data when the material is tested within the creep range are flexural testing (whether 3-point or 4-point) and uniaxial tensile testing. Bi-axial, tri-axial, compression and pure shear tests are also carried out, but are less common.

Tensile testing can itself be subdivided into constant load testing which is the more common form and constant stress testing which typically assumes that the volume of the material does not change as it creeps and uses profiled weight hangers so that as the specimen creeps the lever arm shortens, reducing the load in proportion to the reduced cross-section.

The relevant British Standard for the tensile testing of metals is BS3500 (1969) "British Standard Methods for Creep and Rupture Testing of Metals"[98]. In this Standard advice is given on the selection and preparation of test pieces, and amongst other things the dimensions of notched test pieces are prescribed as are parallelism and specimen and load train co-axiality tolerances. However, as is apparent from its title, this standard was written specifically with the testing of metals in mind and there is no comparable standard for the testing of ceramic materials.

The main problem with tensile testing in the creep range is that the load train is also in tension and so the maximum operating temperature of the test rig is usually restricted to that of the load train. As ceramic grips to hold the specimen are, at the present time an impractical proposition, high temperature alloys are

generally used but this still means that maximum possible test temperatures are inevitably lowered, sometimes quite significantly. One way around this problem, which makes use of the unusual property of ceramics that, unlike metals, their thermal conductivity drops as they get hotter, is to use long specimens thereby removing the grips and the load train from the hot zone. Unfortunately this inevitably results in a variation of temperature along the specimen, and as, generally, the creep strain rate varies according to

$$\dot{e} \propto \sigma^n e^{-A/T} \qquad\qquad (5.1)$$

the creep rate then varies over the specimen's length which makes extracting the raw data difficult.

With flexural testing the whole of the specimen is at essentially the same temperature and as the load train is in compression those particular problems associated with tensile testing are removed. Flexural testing does however have one major drawback; as materials creep at different rates in tension and compression the stress distribution in a flexural specimen is statically indeterminate. One possible way around this problem would be to test an 'I beam' type section. If the flanges were thin then the stress in them could be assumed sensibly constant. However in order to limit the possibility of creep buckling the flanges would probably have to be sufficiently thick for the approximation of uniform stress to become unacceptably inaccurate.

Another drawback with flexural testing is that in creep ductile materials the geometry of the test can change appreciably with time which means that the stress distribution has the added complication of being time dependent as well.

To overcome these drawbacks, methods of analyses[eg. 99] have been developed

which enable tensile behaviour to be determined from flexural test data. These techniques assume that for a given material tested at the same stress in tension and compression that the ratio of tensile to compressive creep rate is constant. This assumption is also implied in the use of the reference stress technique and in this Chapter we extend the application of this technique to ceramic materials.

5.2   Definitions.

The Concise Oxford Dictionary[100] defines a ceramic as a substance "made of (esp.) clay and permanently hardened by heat" and the term itself comes from the Greek word $\kappa\epsilon\rho\alpha\mu\sigma\varsigma$ - Keramos, which means potter's clay.

It is, however, difficult to give a precise definition which allows a distinction to be made between for example, porcelain and the engineering ceramics which are the subject of this work. Therefore, instead of saying what constitutes an engineering ceramic, we will say what it is not. An engineering ceramic does not derive from clay. Unfortunately this contradicts the definition of a ceramic given above. To get around this we will offer a second definition encompassing both clay based and engineering ceramics, viz: Ceramics are non metallic inorganic solids.

5.3   Early uses of ceramics.

The rheological properties of clay are well known; if a vessel is thrown and allowed to dry most of the water is lost and the clay hardens. Below about 400°C this process is reversible; place the vessel in water and it collapses back to its original fluid state. Above this temperature the water that is lost from the clay cannot be replaced; immersing the article has no effect as the clay has permanently hardened to become an example of the earliest form of man made ceramic, pottery.

Ceramic materials, in the form of pottery, have been used by man for at least 9000 years, originally and primarily for more robust solid objects like loom weights

and net sinkers, and later and more commonly for drinking and storage vessels; their disadvantage of being extremely brittle being outweighed by their ease of replaceability. About 6000 years ago, in what is now Iraq, sand and straw was first added to clay to produce building bricks, and even today in some countries with low humidity mudbrick (also known as adobe) is still a widely used building material.

5.4   Uses and properties of engineering ceramics.

Despite developments in their manufacturing processes and refinements to raw materials, the principal uses of ceramics ie. pottery in its widest sense, and as a building material, did not change until the end of the last century when in 1891 an American, Edward Acheson, in an attempt to manufacture synthetic diamonds invented silicon carbide, the first of the so called engineering (or fine) ceramics.

Until the discovery of boron carbide in 1929 silicon carbide was, after diamond, the hardest material known and was used mainly as an abrasive, being better known by one of its trade names - Carborundum. Natural ceramics have also been widely used as abrasives for hundreds of years. Flint (a form of quartz) is the sand in sandpaper and emery (aluminium oxide in an iron oxide matrix) is so well known that its name has become synonymous with abrasives. Corundum (aluminium oxide) is used as a polish and diamonds are used in specialist grinding and polishing applications.

Typically, all ceramics demonstrate a combination of hardness, strength at high temperature, a high elastic modulus, chemical inertness and low density. Table 1.1 lists mechanical and thermal properties of some common engineering ceramics.

5.5 Designing with room temperature ceramics.

The typical properties of ceramics listed in section 5.4 would suggest numerous potential uses. Unfortunately, ceramics have two further characteristics which at present make them difficult to design with. Firstly, as has already been mentioned, they are very brittle. This is not a particular drawback with traditional ceramics as these materials are relatively cheap and easy to replace; however this

Material	Hot Pressed Si_3N_4	Reaction Bonded Si_3N_4	Sintered Si_3N_4	Hot Pressed SiC	Reaction Bonded SiC	Sintered SiC
Density, kgm^{-3}	3300	2400	3200	3300	3100	3200
Young's Modulus, GNm^{-2}	290	200	290	430	413	390
Yield stress, MNm^{-2}	8000	8000	8000	10,000	8000	8000
RT Flexural strength, MNm^{-2}	830	295	800	550	390	490
600 °C Flexural strength, MNm^{-2}	805	295	725	520	390	490
Thermal expansion coefficient, $10^{-6}K^{-1}$	2.7	3.1	3.1	4.6	4.3	4.2
RT Thermal conductivity, $Wm^{-1}K^{-1}$	29	10	33	80	225	71
600 °C Thermal Conductivity, $Wm^{-1}K^{-1}$	22	10	18	51	70	48

Table 5.1. Typical mechanical and thermal properties for common engineering ceramics.

is not the case with engineering ceramics.

Even though they have moderate to low coefficients of thermal expansion their extreme brittleness means that they are susceptible to failure due to thermal

shock. This brittleness also manifests itself in a very low strain to failure which in turn means that their short term stress strain relationship is linear from zero stress to failure. At first glance this linearity may appear advantageous but in practice the lack of any appreciable plastic deformation means that a more complex design method is required to avoid stress concentrations being built into the component.

Secondly the strength data of ceramics always exhibit a wide scatter resulting from the numerous random flaws introduced into the material of the test piece during fabrication. From this combination of inherent brittleness and variability it is easy to see that the key to designing with ceramics is designing for reliability.

The reliability of a component is the likelihood that it will not fail within its design life when operating under its design loading. Reliability prediction for brittle materials was largely a mixture of empiricism and guesswork until 1939 when Weibull[101] demonstrated that probability theory held the answer.

Weibull argued that just as a chain breaks when one link fails, a ceramic component will fail if one of its elements fails. He extrapolated this analogy to produce the elegant yet simple result that the reliability, R (one minus the probability of failure), of a brittle component of unit volume is given by

$$R = \exp\left[\int_V \left(\frac{\sigma_I}{\sigma_0}\right)^m dV\right] \qquad (5.2)$$

where σ_I is the maximum principal tensile stress acting on an element of material of volume dV; σ_0 is a normalising stress; V is the total volume of material and the Weibull modulus, m, is a material property. Materials with a high modulus demonstrate less scatter and are therefore more reliable. Though more sophisticated expressions for reliability prediction have been developed, Weibull's

original equation is still widely used in practice.

5.6   Designing with High Temperature Ceramics.

Despite their many useful low temperature applications, it is to the designer of high temperature components that engineering ceramics appeal the most.

The theoretical maximum efficiency, η , of all high temperature engines is limited by the ratio of the absolute ambient temperature, T_a, to the temperature at which their exhaust is discharged, T_e, ie.

$$\eta = 1 - \frac{T_a}{T_e} \qquad (5.3)$$

The high temperature components of modern gas turbines are traditionally made of nickel based alloys like Nimonic 80A and they have a maximum sustainable operating temperature of the order of 1400°C. Assuming the ideal case that this engine operated adiabatically then it would have an efficiency of 82%. Engineering ceramics offer the possibility of higher operating temperatures and therefore higher efficiencies. However it is easy to see that to achieve only a modest increase in efficiency say from 85% to 90% would require a large increase in T_e from 2000K to 3000K. Obviously engines do not operate adiabatically and these levels of efficiency are never achieved in practice. The point remains, however, that in terms of efficiency these engines are already operating well within the region of diminishing returns and there is not much to be gained by trying to increase their operating temperatures. The specific power output on the other hand, that is the power output per unit of consumed fuel, is proportional to T_e so from this point of view there is potentially much to be gained by running these engines at higher temperatures. However gas turbines already run at temperatures at which the nickel alloys used for their blades have almost zero operating life, this

only being possible by clever design in which air is forced out through holes at the root to flow over the blade and cool it. The obvious answer to this problem is to change the material and use one with a higher sustainable operating temperature. Putting this into practice is proving rather difficult. However two classes of components that are beginning to be effected by developments in ceramic technology include gas turbines; the other being the diesel engine.

An uncooled adiabatic diesel engine is a real possibility due to the ability of ceramics to withstand high temperatures without cooling. Such an engine has been produced and installed in a five ton truck which has done over 10,000 miles with a 50% increase in fuel efficiency[102].

The four most critical components in a gas turbine are the stators, rotor, regenerator and the housing. The housing must operate uncooled at temperatures greater than 1000°C; the chosen material must have low coefficients of thermal expansion and conductivity.

A regenerator uses energy from the exhaust gasses to increase fuel efficiency. It does this by heating and compressing the air which flows to the combustion chamber which then requires less fuel to raise the temperature of the pre-heated air for expansion through the turbine. Suitable materials for a regenerator must also have a low coefficient of thermal expansion and must be resistant to chemical attack from the hot exhaust gasses.

Rotors and stators are the most complex components in a turbine and they operate at the highest temperatures. As operating speeds of 80,000 r.p.m. are common they are also the most highly stressed components. As yet the reliability and durability problems associated with these components have not been solved. It is true that ceramic turbocharger rotors have been used for a number of years,

however the operating speeds of these devices are nowhere near those commonly used in gas turbines, nor are the temperatures as high. Ceramic rotors are used in this situation to reduce turbocharger lag by virtue of the low density of these materials.

5.7 Experimental objective.

In high temperature materials tests, specimens of known dimensions are subjected to either tensile or flexural loading over a range of different stresses and temperature levels with the aim of determining particular material properties such as the creep exponent or an activation energy for a particular mechanism.

However, high temperature structural components are rarely as simple as plain tensile or flexural specimens and it was thus the aim of our experimental programme to develop an understanding of the way in which a component's geometry affects its high temperature behaviour. To that end we decided to investigate the behaviour of specimens containing two similar notches of known dimensions. The object was to compare the behaviour of these notched specimens with that of similar specimens without notches, with the aim of determining whether there was any evidence of a transition at any point from failure due to a net section stress effect characterised by widespread continuum damage to failure due to the growth of a dominant crack (creep crack growth). The reason for having two notches was so that after the specimen had failed, which it was assumed would not occur simultaneously at both notches, the failure surface and a section through the 'unfailed' notch could both be examined.

5.8 Material selection and preparation.

As has already been mentioned creep crack growth occurs in an incremental manner due to the growth and coalescence of microvoids ahead of a crack tip. In

fully dense material these voids may take a considerable proportion of the failure time to nucleate. Given that only one test rig (to be described later) was available and that creep tests, by their very nature take a long time, it was decided to test a material with pre-existing 'voids'. There are many porous ceramics available and whilst connected porosity is usually on a larger scale than the voids we have been considering up to this point, there is no fundamental difference with regard to the applicability of the diffusive cavity growth models described earlier.

The decision of which particular material to use in the tests was effectively made for us when T&N Technology of Rugby, England offered to provide free reaction bonded silicon nitride (RBSN) specimens.

Silicon nitride exists in two crystallographic forms; alpha and beta, with alpha being the low temperature form. Above approximately 1450°C the alpha phase transforms irreversibly to the beta phase.

A number of different techniques exist for the preparation of silicon nitride. The most common being the direct nitridation of silicon according to the reaction

$$3Si + 2N_2 \rightarrow Si_3N_4 \qquad (5.4)$$

By nitriding below approximately 1450°C a coarse, grey, predominantly alpha phase powder is produced.

Alternatively fine silicon dioxide powder will react with carbon and nitrogen to produce silicon nitride according to

$$3SiO_2 + 3C + 2N_2 \rightarrow Si_3N_4 + 3CO_2 \qquad (5.5)$$
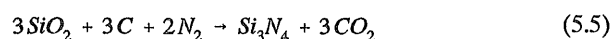
The excess carbon which inevitably remains is then removed by oxidising in air. Once produced the powders are milled to reduce them to the required particle size.

A reaction bonded silicon nitride component is produced by direct nitridation

of a green compact of pure silicon, which produces a structure with a connected porosity of typically 20-25%, see Plates 5.1a and 5.1b.

Green body preparation is usually by one of three methods. The simplest method of producing limited quantities of small components is die pressing in which the powders are pressed in steel dies at pressures of up to 30Mpa. The pressed component then has sufficient strength to be sealed in a rubber sleeve and cold isostatically pressed at up to 600Mpa after which careful machining, still in the green state, is possible.

Slip casting involves the preparation of an aqueous suspension (or slip) of the ceramic powder which is then poured into a plaster mould. The mould absorbs the liquid leaving a green body on the mould surface. By progressively adding more slip solid components can be formed, a technique known as solid casting. Hollow components are formed by draining off excess slip after a sufficient wall thickness has been deposited.

For producing large numbers of complicated components injection moulding is the preferred technique, in which the ceramic powders are mixed with a binder (of, for example, polystyrene or paraffin wax) and simply injected into the mould. The only significant drawback with this process is in the difficulty of removing the binder without causing internal cracking. For this reason injection moulding is particularly suited to the production of thin components.

The specimens used in the series of experiments reported here were prepared by die pressing.

The open structure of RBSN means that the finished component is significantly weaker at both room and elevated temperatures than *hot pressed* silicon nitride (HPSN), which is virtually fully dense (see Table 5.1). RBSN does however

have two major advantages over the fully dense form. Full densification of silicon nitride is impossible without the addition of sintering aids, which by definition must have a lower melting point than the nitride. These aids therefore have a deleterious effect on the creep properties of the finished component. Secondly densification obviously results in a change in volume. In the nitriding process no dimensional changes occur and large complex shapes can therefore be produced from RBSN to very high dimensional tolerances.

Machining in the green state introduces surface damage but if the machining is done carefully this will heal during nitriding. After nitriding, fine grains of α Si_3N_4 exist on the surface of the component. These may be ground away but grinding would introduce more damage, in the form of microcracks, in the surface of the component. It was therefore decided to test the specimens in the as received condition.

5.9 Furnace redesign.

The rig used for the testing programme was based on a Severn Science model HTTF2 furnace (serial 870804). This furnace was originally designed to test small specimens in 4-point bending, the specimens resting on supports 50mm apart and loaded by rollers, centred over the supports, 25mm apart.

For component testing rather than material testing it was felt, for two reasons, that a nominal gauge length of 25mm was rather limiting.

Firstly, whilst being of a known concentration the notches needed to be as large as possible. This is because the specimens were to be tested in the 'as received' state, and the geometry of a *very* small notch would be affected significantly by the surface finish of the specimen.

Secondly, structural components are likely to be larger than 25mm and a

bigger component will have a more realistic distribution of flaws. Therefore, comparing one with another, larger components made from a brittle material should show less statistical variation in their failure behaviour.

The total volume in the as bought furnace was approximately 130mm (wide) by 100mm (high) by 110mm (deep), with the elements reducing the effective depth to approximately 80mm. The hot zone, which we arbitrarily defined as the zone over which the temperature differed by no more than 1°C from that at the centre, was found by investigation to be sufficiently large to allow specimens in excess of 100mm to be tested. To facilitate testing specimens of this size the as bought rig (a drawing of which is shown in Figure 5.1) was modified as follows.

The existing stainless steel top and bottom plates, complete with cooling water jackets were swapped around so that the existing 60mm alumina tube, originally intended to support the specimens, now supported the loading platen. A stainless steel end cap was cemented to the 'cold' end of the tube to transfer the load uniformly to the alumina.

To ensure rotational alignment of the loading platen a system of bearings was designed that restrained the end cap from rotating about the axis of the alumina tube; vertical alignment was ensured using a linear bearing. The upper load train guide is shown in Figure 5.2 and Plate 5.2.

The bottom cooling water jacket was then removed and two 25mm diameter holes, 100mm apart, centred directly below the loading tube were drilled through the jacket and stainless steel bottom plate. New brass sleeves and high temperature bushes were fitted to the jacket in these holes. Two 190mm lengths were cut from a 25mm diameter alumina tube to use as the supports.

The initial design of the plain specimens was simply for chamfered 10mm x

10mm x 115mm rods. However during initial trials all of these specimens failed under one or other of the loading rollers, whereas ideally the failures would distribute themselves over the gauge length.

The reason for this was one of the major design faults with the as bought rig. Having two separate supports means that unless they are of exactly the same length the supports and loading platen will not be parallel. With a very stiff test material such as a ceramic this means that 4-point bending will probably never be achieved with the result that the specimen will fail at the location of maximum moment, ie. under one or other of the loading rollers. Obviously it is not possible to grind the support tubes to *exactly* the same length so to get around this problem a rocker arrangement was designed by which the support tubes automatically adjust their positions to restore parallelism and hence true 4-point loading.

With quite long supports passing through quite thin bushes, as was the case in the as bought rig, play at the bushes and consequent lack of parallelism between the supports is an obvious possibility. To overcome this, spring loaded bearings were positioned to hold the tubes vertically while still permitting vertical movement, to ensure 4-point contact. The lower guide and rocker assembly is shown in Figure 5.3 and Plate 5.3.

The loading platen, loading and support rollers and support tube heads were manufactured, also by T&N Technology, from reaction bonded silicon carbide (RBSC). These components, particularly the rollers are very highly stressed, and RBSC is a stronger material than RBSN. Details of the loading head and support tube geometries are shown in Figure 5.4 and the modified rig is shown in full in Figure 5.5.

It also became apparent during initial testing that the loading assembly was

seizing in the bearings when the rig was at its working temperature of 1500°C. This was caused by expansion of the upper bearing assembly due to the 60mm alumina tube acting as a chimney. To reduce this effect the tube was filled with insulating fibre and a housing containing two cooling fans was constructed to sit over the complete upper bearing assembly.

5.10   Specimen design.

Before designing any test component it is necessary to consider the procedures that will be adopted to analyse the results one is expecting to obtain and, most importantly, the way in which the component is expected to behave during the test.

On initial loading at high temperature a body behaves elastically and the stress distribution may be determined by linear elastic analysis. For example when a rectangular beam of width b and depth d is subjected to a moment M the stress distribution, a distance y from the neutral axis, is

$$\sigma = \frac{6M}{bd^2} \frac{2y}{d} \qquad\qquad (5.6)$$

and the maximum stress, which occurs at y = ½d, is

$$\sigma_{max} = \frac{6M}{bd^2} \qquad\qquad (5.7)$$

In the steady state these stresses are

$$\sigma = \sigma_{max}^{ss} \left(\frac{2y}{d}\right)^{\frac{1}{n}} \qquad\qquad (5.8)$$

where

$$\sigma_{max}^{ss} = \frac{4M}{bd^2} \frac{2n+1}{2n} \qquad\qquad (5.9)$$

Now, if a notch of stress concentration k_t is present in the specimen then on initial

Page 135

loading the peak stress is given by

$$\sigma_{peak} = k_t \, \sigma_{max} \qquad (5.10)$$

which, with time will redistribute to the steady state value

$$\sigma_{peak}^{ss} = k_t^{ss} \, \sigma_{max}^{ss} \qquad (5.11)$$

where
$$k_t^{ss} \approx 1 + \frac{1}{n}(k_t - 1) \qquad (5.12)$$

During this redistribution a crack may nucleate and begin to grow, stably at first, and then when it reaches a critical size, unstably, Alternatively a pre-existing flaw may grow in the same manner, leading to a brittle failure.

This type of catastrophic brittle failure is usually described using Weibull statistics where the reliability, R (the probability of survival), of a brittle *elastic* component of unit volume was given by equation (5.2)

$$R = \exp\left[\int_V \left(\frac{\sigma_I}{\sigma_0}\right)^m dV\right] \qquad (5.13)$$

Generalising equation (5.13) to the creep regime is not easy as the stress distribution within a creeping body is both non-linear (if n > 1) and time dependent. In addition to this a large number of specimens need to be tested to provide valid data (at least 20 to roughly determine the Weibull parameters; 100 for statistically valid results). As such a large number of specimens was not available (we had approximately 20 of each) the specimen design had to be such that brittle failure could be clearly identified.

Though no attempt was made to use Weibull statistics directly, examination of the form of equation (5.13) can provide clues as to how to interpret the results

of the tests. For an elastic failure, for both types of specimen, equation (5.13) must be integrated to determine the probability of failure. Now it is evident from equation (5.13) that the smaller the volume of material at a given stress, the less likely is the component to fail. Thus the notched components, by virtue of having most of the stress concentrated in a small area, will appear stronger (ie. less likely to fail) for a given maximum stress than the plain specimens. Therefore it is conservative (in terms of predicting the response of a notched component from the behaviour of a plain component) to use a failure criterion based on the peak stress.

As an alternative to brittle failure, general continuum damage in the form of voids or microcracks may develop during the redistribution process. This damage will grow most rapidly in regions of high stress leading to further stress redistribution.

If the components were to show extensive creep resulting from continuum damage it was anticipated that reference stress techniques might be useful for analysing the results.

As was mentioned earlier, materials generally creep at a higher rate in tension than in compression, and this effect must be taken into consideration when considering the definition of the reference stress. Consider a material that yields in tension when

$$\sigma = \sigma_y \tag{5.14}$$

and yields in compression when

$$\sigma = \alpha \sigma_y \tag{5.15}$$

The limit moment for a rectangular beam specimen made from this material is

$$M_L = \frac{\alpha \sigma_y b d^2}{2(1+\alpha)} \qquad (5.16)$$

Now, if this material creeps in tension according to the law

$$\dot{e} = \dot{e}_0 \left(\frac{\sigma}{\sigma_0} \right)^n \qquad (5.17)$$

and in compression according to

$$\dot{e} = \frac{\dot{e}_0}{\alpha} \left(\frac{\sigma}{\alpha \sigma_0} \right)^n \qquad (5.18)$$

and if we assume a stress field of the form shown if Figure 5.6a then by analogy the moment, M, is given by

$$M = \frac{\alpha \sigma_0 b d^2}{2(1+\alpha)} \qquad (5.19)$$

ie.

$$\sigma_0 = \frac{M}{M_L} \sigma_y \qquad (5.20)$$

This is the flexural form of the reference stress for deformation given in equation (2.16).

As well as that for deformation, there is a different reference stress for failure. The definition of this reference stress is "that stress in a uniaxial tensile test that fails after the same time as the structural component". Consider a material that does not fail in compression but fails in uniaxial tension according to

$$t_f = A \sigma^{-v} \qquad (5.21)$$

For such a material, the reference stress for failure is given by the expression[103]

$$\sigma_0^F = \left[\frac{\int_V d\epsilon^p \ \psi^v(\sigma_{ij}^\infty) \ dV}{\int_V d\epsilon^p \ dV} \right]^{\frac{1}{v}} \qquad (5.22)$$

where $d\epsilon^p$ is the increment in plastic strain at collapse, see Figure 5.6b. $\psi(\sigma_{ij}^\infty)$ is the maximum principal tensile stress determined from the stress distribution obtained from a limit load (reference stress for deformation) calculation.

Now, in our specimen, in the tensile portion

$$\psi(\sigma_{ij}^\infty) = \sigma_0 \qquad (5.23)$$

and in the portion of the specimen in compression

$$\psi(\sigma_{ij}^\infty) = 0 \qquad (5.24)$$

therefore

$$\sigma_0^F = \sigma_0 \left[\frac{\int_{V_T} d\epsilon^p \ dV}{\int_V d\epsilon^p \ dV} \right]^{\frac{1}{v}} \qquad (5.25)$$

where V_T is the volume of the beam in tension. From Figure 5.6b we can easily see that for a rectangular specimen

$$\sigma_0^F = \sigma_0 \left[\frac{\alpha^2}{1 + \alpha^2} \right]^{\frac{1}{v}} \qquad (5.26)$$

Now, under conditions of plane stress, the stress distribution and mechanism of collapse across the minimum section of the notched specimen would be the same as that for the plain specimen, ie.

$$\sigma_0^F = \sigma_0 \left[\frac{\alpha^2}{1 + \alpha^2} \right]^{\frac{1}{v}} \frac{2M(1 + \alpha)}{\alpha \, bd^2} \qquad (5.27)$$

ie., for both specimen types

$$\sigma_0^F \propto \frac{M}{d^2} \qquad (5.28)$$

Thus under conditions of continuum damage, specimens with the same depth and subject to the same bending moment have the same reference stress for failure and will fail after the same time. Obviously with a variable material like a ceramic individual tests may differ from this expectation but on average the failure times should be equal.

From the above we can see that in conditions where failure is governed by the maximum elastic stress (brittle failures) we have the following situation

Plain	Notched

$$\sigma_{peak} = c_1 \frac{M}{d^2} \qquad\qquad \sigma_{peak} = k_t c_1 \frac{M}{d^2} \qquad (5.29)$$

and in conditions where failure is governed by the reference stress (continuum damage) we have

$$\sigma_0^F = c_2 \frac{M}{d^2} \qquad\qquad \sigma_0^F = c_2 \frac{M}{d^2} \qquad (5.30)$$

The ratio of the failure times for the two specimens, t_R, which we defined as the time to failure of a notched specimen divided by that of a profiled specimen, for the same applied bending moment may be expected to have a maximum value of unity when failure is as a result of continuum damage. When failure is the result of creep crack growth this ratio will be less than unity by a factor depending, through the constitutive law, on the magnitude of k_t, see Figure 5.7.

In designing the notches it was decided that the ratio of the peak elastic stress at the notch root to that in a plain specimen for the same applied moment,

k_c, should be 2.0. This value was chosen somewhat arbitrarily but it was hoped that it was high enough for brittle failures of the two specimen geometries to be clearly differentiated, but low enough that failure of the plain specimens would occur within a reasonable length of time.

The section of the plain specimens had already been determined as 10mm by 10mm and so the stress in the outermost fibres (ie. not at the root) of the notched specimen would be $(10/d)^2$ times that in the plain specimen; where d is the overall depth of the notched specimen. By an iterative process a notch with a depth of 3.0mm and a root radius of 2.0mm was decided upon, giving an overall depth of specimen of 13.0mm. A notch with this geometry has an elastic stress concentration factor, k_t of 3.32 which gives a ratio of peak stress at the notch to peak stress in a plain specimen under similar moments, k_c, of 3.32 x $(10/13)^2$ ie. 1.96. This was considered satisfactorily close to 2.0 and the specimens were ordered from T&N Technology on this basis. The dimensions of the notched specimens are given in Figure 5.8 and an untested specimen is shown in Plate 5.4.

Despite extensive efforts to ensure a reasonable distribution of failures along the gauge length, by far the majority of the first plain specimens tested continued to fail under one or other of the loading rollers. To try to eliminate this tendency the section of the plain specimens was reduced to 7.5mm by 10.0mm over a 47mm length by grinding off 2.5mm with a diamond wheel. Several of these new *profiled* specimens were tested, with the machined surface in compression, and the failures were found to be reasonably evenly distributed over the gauge length see Plate 5.5. The dimensions of the profiled specimens are shown in Figure 5.9. and an untested specimen is shown in Plate 5.4.

Our original aim was to test notched specimens with a cross-section at the

root equal to that of the plain (ie. non-profiled 10mm x10mm) specimens. However, the double notched specimens were machined in the green state by T&N Technology and were therefore supplied with the notches already present. The subsequent need to redesign the plain specimens meant that this initial aim was no longer possible.

Upon receipt from T&N Technology the plain specimens (the profile had yet to be ground) were measured for their dimensional accuracy, weighed to determine their porosity and numbered on one end with a diamond engraver.

The RBSN was found to have a mean density of 2.500 gcm^{-3} which, indicates a porosity by volume of 24%, which is at the high end of the range. This value, though high, was fairly consistent displaying a variation about the mean of -1.6% to +0.84%.

None of the principal dimensions of the specimens was found to vary by more than 0.04mm from its nominal value.

The notched specimens were also numbered and measured upon receipt. The notches were designed a root radius of 2.0mm and a depth of 3.0mm to give a K_t of 3.32. Using a shadowgraph both notches on five specimens (nos. 8 to 12 inclusive) were accurately measured. The depths of the notches were found to be very close to the required 3.0mm having an average value of 3.01mm and displaying a variation range of -1.8% to +1.5%. The mean root radius of 2.03mm was also close to the required value and displayed a similar range.

5.11 Design of the extensometry.

In designing the extensometry it was a prime requirement to separate the deformation behaviour of the specimens from that of the load train or the supports. This was achieved in the as bought rig by using two alumina rods which were sprung

against the underside of the specimen (see detail in Figure 5.1). There are two major problems with this arrangement. Firstly, as the rods were flat ended, the exact position at which the deformation is measured is unknown. Secondly, as creep in tension is more rapid than in compression, contact with the tensile surface of the specimen, with its attendant risk of contamination, should be avoided.

These problems were circumvented in the redesigned rig by drilling three holes through the stainless steel end cap of the 60mm alumina tube, in the plane of the axis of the specimen, one in the centre and the others 20mm on either side. Matching holes were then spark eroded in the silicon carbide loading platen and alumina guide tubes were inserted through the insulation in the 60mm diameter loading tube and held in place at the cool end by circlips. Solid alumina rods with their bottom ends ground to a 'blunt point' were then lowered through the guides to rest on the specimen. The outer rods were fixed to each other by a clamp which also held the body of a displacement transducer over the central hole. The shuttle of the transducer rested on the top of a third shorter alumina rod so that strain in the specimen would be measurable as a displacement of the centre with respect to the outer points. Global translations however, due for example, to creep of the supports, would not register as all three rods would respond to the deformation. In this way the desired creep of the specimen was isolated from the inevitable creep of the load train. The output from the displacement transducer was recorded continuously by a chart recorder and every hour by an automatic data logger.

The prime function of the extensometry was to measure the deformation rate of the profiled specimens, as it was envisaged that any measurable deformation of the notched specimens would occur primarily at the notch roots. In testing the notched specimens the main function of the extensometry was, via the chart

recorder, to measure the precise time to failure of the notch.

If we assume that the gauge length of a profiled specimen deforms to the arc of a circle (an accurate assumption for small deflections) then the strain can easily be found from the deformation.

If the mid point deflection of a rectangular four-point bend specimen relative to two outer reference points, 2D apart, is δ, then from the theorem of perpendicular chords the radius of curvature R, and δ are related by

$$2R\delta - \delta^2 = D^2 \qquad (5.31)$$

and as δ is always small we can say

$$R \approx \frac{D^2}{2\delta} \qquad (5.32)$$

In pure bending the strain, ϵ, at a hypothetical fibre, a distance y from the neutral axis of the section in question, is related to the radius of curvature of the neutral axis at that section by

$$\epsilon = y/R \qquad (5.33)$$

The largest value of D that could be accommodated in the redesigned loading head was 20mm, so for our profiled specimens, where the peak strain occurs at y = 3.75mm

$$\epsilon = \frac{15\delta}{800} \qquad (5.34)$$

5.12   Experimental procedure.

The numbered profiled (P type) and notched (N type) specimens are referred to as, say, N10 or P23. For the notched specimens the numbered end was considered to be the left end for the purpose of distinguishing between the notches

and the specimens were placed in the rig accordingly. Precise, repeatable alignment was achieved using a small jig machined from a block of aluminium.

To get a feel for the level of bending moment at which to test, 6 notched specimens were heated to 1500°C and loaded rapidly to failure, the load being applied via a load cell. The peak moments and times to failure are listed in Table 5.2, the notch which failed is also indicated. The mean maximum moment was found to be 16.11Nm and, given the low number of specimens tested, there was a reasonable distribution of failures between the left and right notches.

Specimen No.	Maximum bending moment (Nm)	Failed notch
N2	15.66	L
N3	14.89	L
N4	17.02	L
N13	16.25	R
N20	15.74	L
N21	17.10	R

Table 5.2. Peak elastic stresses at failure under rapid loading in six double-notched specimens. The mean maximum moment was 16.11 Nm.

The basic procedure for creep testing both the profiled and notched specimens was the same, namely:

1) The specimen was positioned using the jig.

2) The cooling fans were turned on.

3) The furnace temperature was ramped up to 1500°C at 200°C per hour. This ramp rate was fixed by the susceptibility of the heating elements and alumina tubes to thermal shock.

4)   The temperature was held at 1500°C.

5)   After soaking for 2 hours to achieve thermal equilibrium within the specimen, the loading head and the supports, the weight hanger was slowly lowered until all the load was transferred to the specimen.

6)   After failure the furnace was ramped down at a nominal 200°C per hour. As the furnace contained no cooling equipment other than the water jackets it was not possible, below about 500°C, to force the furnace to cool down at this rate.

Constant ramp rates during the ramp up phase were achieved using a Eurotherm 818P programmable temperature controller (serial M00869.001) and after initial testing a microswitch was positioned under the loading arm so that when the specimen failed and the lever arm dropped the switch was depressed automatically toggling the controller to the ramp down phase of the program. Below about 500°C the controller effectively switched the furnace off and it cooled down at its own rate.

5.13   Results of the creep tests.

Over a period of approximately eighteen months twelve notched and eleven profiled specimens were tested, all at 1500°C, at bending moments ranging from 5.11Nm to 12.76Nm. Full results for the profiled specimens, of creep strain as a function of time (as captured by the data logger), are listed in Appendix 6. These results are summarised below in Table 5.3. Specimen P23 is not included in Table 5.3 as when the test was abandoned after 594 hours it was discovered that one of the bearings in the guide system of the loading platen had seized and that therefore for an unknown proportion of the test the applied load was also unknown.

The failure times of the notched specimens are summarised in Table 5.4.

Specimen No.	M_p (Nm)	M' (Nm)	Elastic strain (μ)	Creep strain (μ)	Time to failure (h)
P4	8.44	15.00	506	1088	44.75
P6	8.44	15.00	619	1284	55.7
P19	8.44	15.00	731	1116	17.6
P8	9.38	16.68	-	-	46.5
P10	9.38	16.68	750	-	58.1
P1	9.84	17.49	750	544	1.8
P17	9.84	17.49	750	900	31.75
P24	9.84	17.49	750	628	5.2
P7	10.31	18.33	806	647	12.4
P14	11.25	20.00	-	-	8.5
P18	11.25	20.00	844	609	11.2

Table 5.3. Bending moments and failure times for the eleven profiled specimens which were tested successfully. The elastic and creep strains of P8 and P10 were not recorded due a temporary failure of the pen recorder. M' is defined later in equation (5.33).

Specimen No.	M_n (Nm)	Time to failure (h)	Failed notch
N8	5.11	>400	-
N17	8.51	2.80	R
N5	10.21	0.55	R
N6	10.21	87	L
N19	10.21	1.3	L
N22	10.21	4.9	R
N24	10.21	2.25	R
N25	10.21	23.2	L
N9	12.76	0.08	L
N10	12.76	2.23	L
N11	12.76	0.08	R
N12	12.76	0.03	R

Table 5.4. Bending moments and failure times for the twelve notched specimens which were tested successfully. The test on specimen N8 was abandoned due to a short power failure over a weekend causing the temperature controller to toggle to ramp down.

5.14 Interpretation of the results.

Were both the notched and profiled specimens of the same minimum depth, d, then we could simply compare failure times resulting from the application of similar bending moments; however, d is not the same in both specimens. Recall from equations (5.29) and (5.30) that σ_{peak} and the reference stress for failure display the same dependence on bending moment and d^2 for both specimen types. If we define an equivalent moment, M', for the profiled specimens as

$$M' \equiv M_p \, x \, (10/7.5)^2 \qquad (5.35)$$

we can evaluate M' and compare the times to failure at this load level with the times to failure of the notched specimens under the applied moment M_n.

If a failure criterion based on the reference stress holds, ie. if we have a ductile failure, then we would expect the times to failure to be equal for the case of M_n = M'. On the other hand if the failure criterion is based on the maximum elastic stress, ie. when the failure is more brittle, we would expect equal failure times when

$$\frac{M'}{M_n} = k_c = 2 \qquad (5.36)$$

Consider the data for the profiled specimens P1, P17 and P24 for which M = 9.84Nm and from equation (5.33) M' = 17.49Nm. These specimens displayed failure times ranging from 1.8 to 31.75 hours. If the failure of these specimens was governed by a maximum elastic stress effect then the failure times of the notched specimens would be over the same range if M_n = 17.49Nm / 2 ie. if M_n = 8.75Nm. If failure was as a result of a reference stress effect then the failure times of the notched specimens would be over the same range if M_n = 17.49Nm.

Notched specimens N5, N6, N19, N22, N24 and N25 when tested at M_n = 10.21Nm displayed failure times of between 0.55 and 87 hours, a similar range to the above. In this instance M' / M_n = 1.71. Thus we can see that these results lie closer to the maximum elastic stress criterion than to the reference stress criterion of M' / M_n = 1.

Notched specimens N9, N10, N11 and N12 were subjected to a bending moment of 12.76Nm and three of the four tests lasted less than 5 minutes. All of the profiled specimens listed in Table 5.3 were tested at reference stresses higher than these specimens (note, though, that we do not determine this reference stress which would require an assumption to be made as to the value of α in equation (5.15)) and all displayed a longer failure time. This would indicate that failure was probably not the result of continuum damage. A value of M' of 25.52Nm would produce equal failure times if failure was definitely the result of a maximum elastic stress effect. No profiled specimens were tested at a bending moment as high as this, however we can see from the general trend of the results in Table 5.3 that an applied bending moment of this magnitude would result in a failure time significantly less than the 8.5 hours of P14.

The specimens listed in Table 5.2 were deliberately failed in a brittle manner and the failed notch of one of these specimens is shown in Plates 5.6a and 5.6b. This type of failure surface is characteristic of a flexural failure in a brittle material. Failed notches from some of the long term tests listed in Table 5.4 are shown in Plates 5.7, 5.8, and 5.9 and it can be seen that these failure surfaces, which are typical of all those examined, are similar in form to the short term failure surface supporting the above conclusion that the notch failures were creep brittle.

In all of the notched specimens tested there was no measurable creep

deformation before failure. There was also little creep deformation in the profiled specimens; in only three of the nine specimens for which the initial elastic strain was measured did the accumulated creep strain exceed the elastic strain plus 20%. This would seem to rule out the presence of large scale continuum damage in either type of specimen as, typically, strains greater than 8% may be observed in conditions of continuum damage[22]. The profiled specimens also displayed the same brittle type failure surface as the notched specimens, see Plate 5.10.

Examination by electron microscope, of both the failed and unfailed notches, was however, inconclusive.

A porous material was chosen to shorten the testing time by removing the need for void nucleation. This inevitably means that continuum damage even if it were present would be very difficult to recognise against the background of pre-existing porosity. It is simply a case of not being able to see the wood for the trees. Similarly a creep crack on the microscopic level would appear as connected porosity, and as the porosity in RBSN is not discrete, the crack would again be unrecognisable. For a creep crack to be large enough to be recognisable as such on the *macroscopic* level it may well have to exceed its own critical size for the load level tested.

On a failed surface the evidence of void growth in the form of 'half voids' often reported in fully dense materials such as alumina would also be indistinguishable from the pre-existing porosity.

Electron micrographs of a section through an unfailed notch are shown in Plates 5.11a-d and electron micrographs of a failed surface are shown in Plate 5.12a and 5.12b. These micrographs, which are typical of all those obtained, clearly illustrate the problem; although we believe these failures to be as a result of creep

crack growth there is no recognisable evidence from the micrographs, either for or against this conclusion.

5.15 Summary.

We have conducted a series of 4-point bend tests on plain and notched reaction bonded silicon nitride specimens with the aim of investigating whether there is any evidence of a transition from failure due to the growth of continuum damage at low load levels to failure due to the growth of a dominant crack at higher load levels. To that end we have designed and manufactured a series of modifications to an 'off the shelf' furnace which we believe result in a significant improvement in the performance of the rig.

Through a careful consideration of the likely behaviour of the test material we have designed two specimen geometries; one plain within the gauge length, and one notched. The notch geometry was chosen so that failure could be easily identified as either brittle or ductile.

Twenty three specimens were creep tested and are believed to have failed in a brittle manner as a result of creep crack growth. This belief is supported by the low levels of creep ductility observed. A lack of time and being restricted to one test rig meant that we were unable to test at load levels low enough for continuum damage possibly to develop. In the specimens tested there is no evidence of any failures as a result of continuum damage and consequently there is no evidence of a brittle/ductile transition.
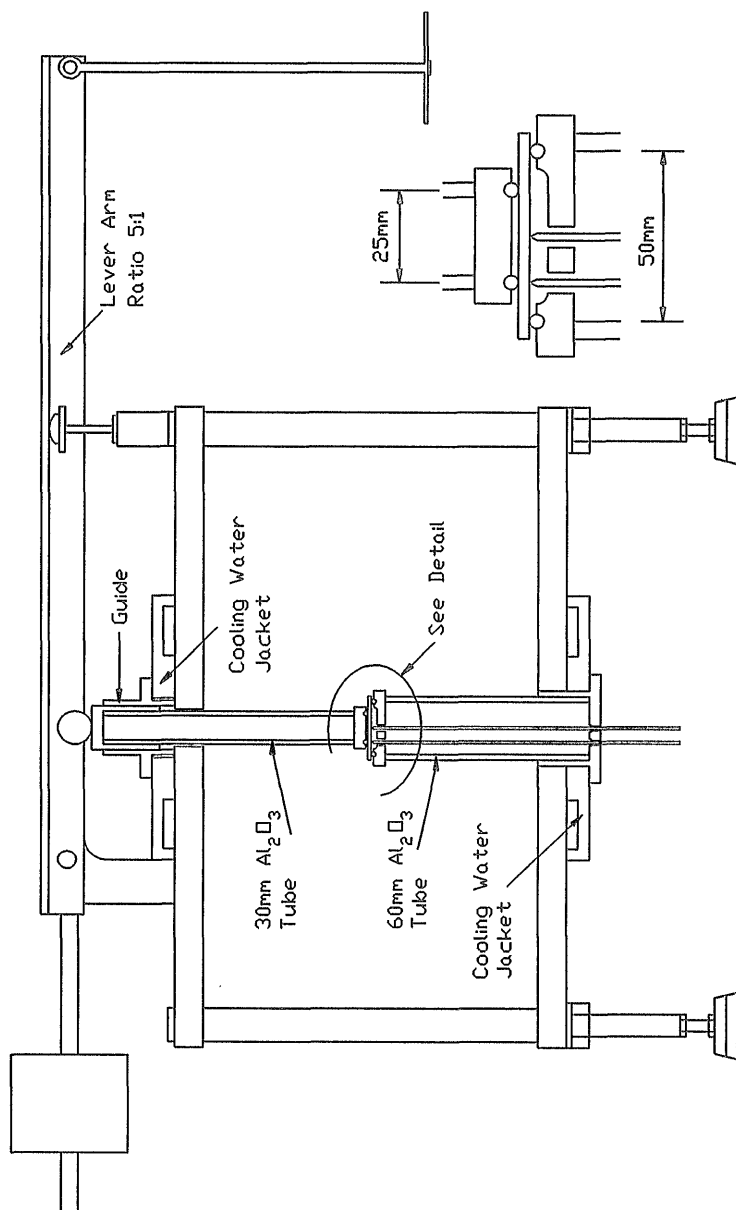
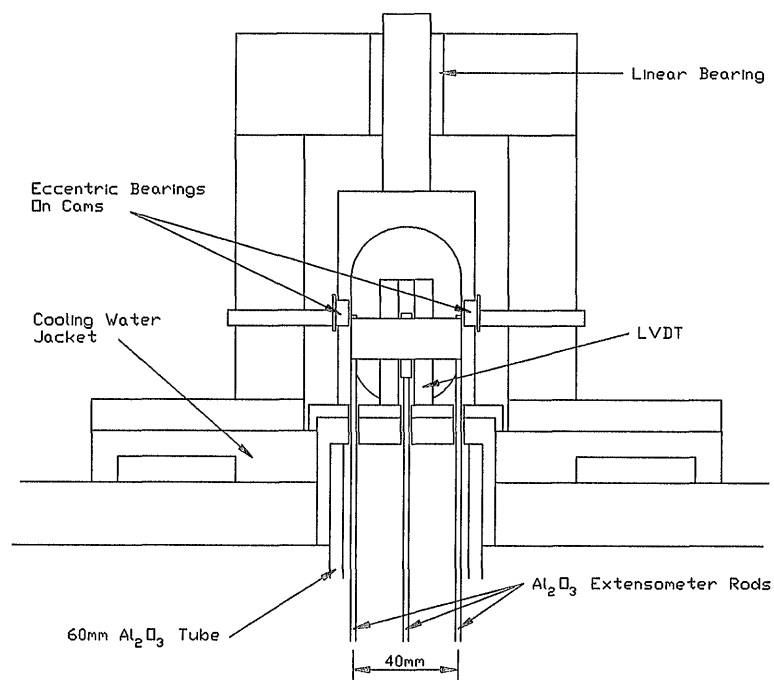**Figure 5.1.**   Part section through Severn Science four-point bend rig - as bought.

Figure 5.2. Upper guide and extensometry assembly. The linear bearing ensures that the load train moves perpendicular to the specimen in both planes. The eccentric bearings, after being rotated into position on their cams and locked off ensure that the loading platen can not rotate about the linear bearing.
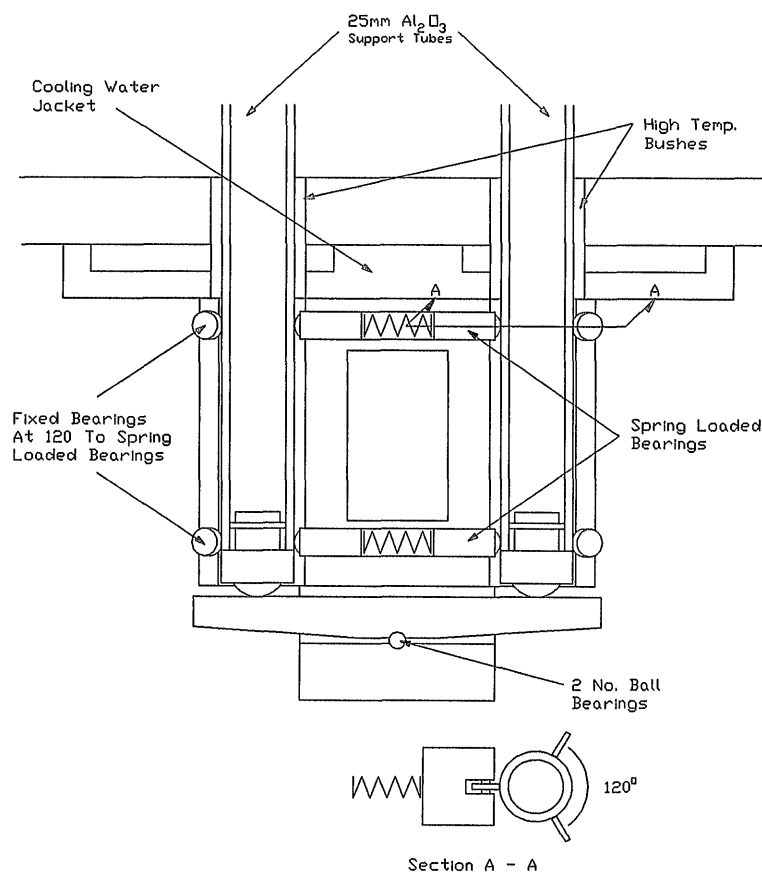
Figure 5.3. Lower guide assembly. The fixed bearings ensure that the support tubes are both initially parallel and constrained to displace along parallel axes. Friction at the sprung bearings prevents the support tubes from rotating about their own axes. The rocker assembly, which rests on ball bearings, ensures initial parallelism between the specimen and the supports and thus ensures also that four-point rather than three-point contact is maintained.
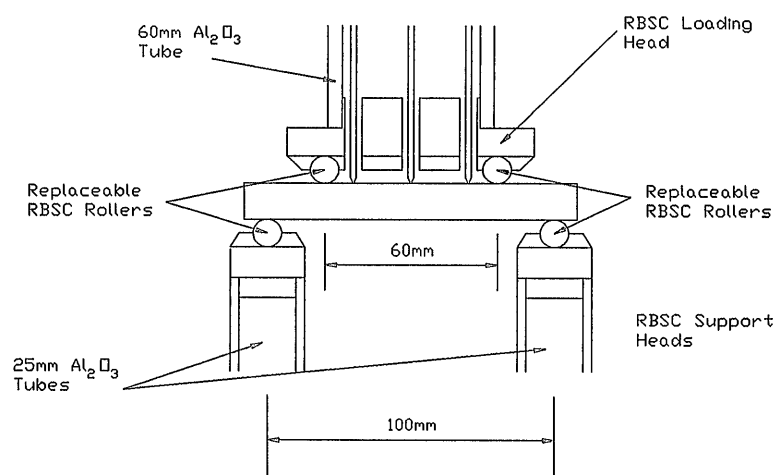
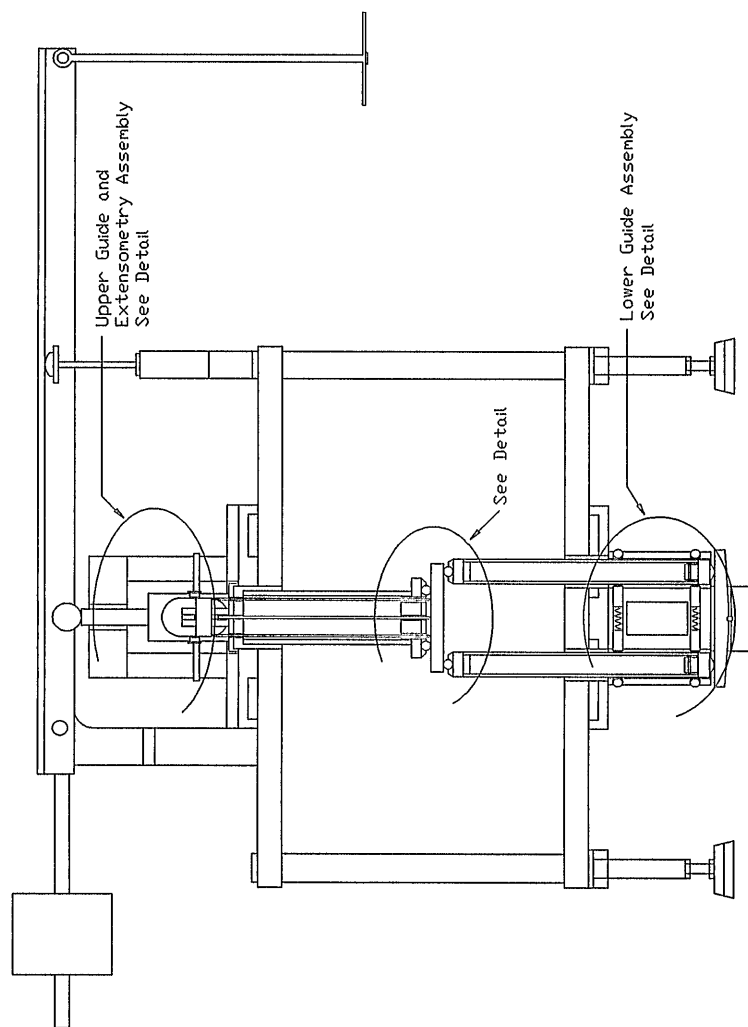**Figure 5.4.**   Loading head and support tube geometry.

Figure 5.5. Part section through redesigned four-point bend rig, based on as bought Severn Science four-point bend rig shown in Figure 5.1. The rig is shown, for clarity, with the cooling fans removed.
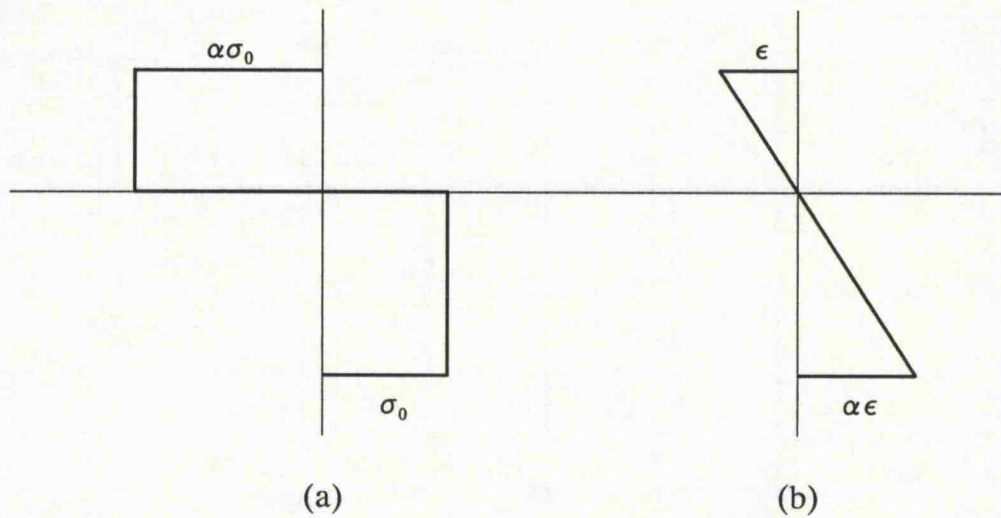
Figure 5.6a. The assumed stress distribution in a rectangular beam specimen subject to an applied bending moment M. **Figure 5.6b.** The strain increment at collapse.
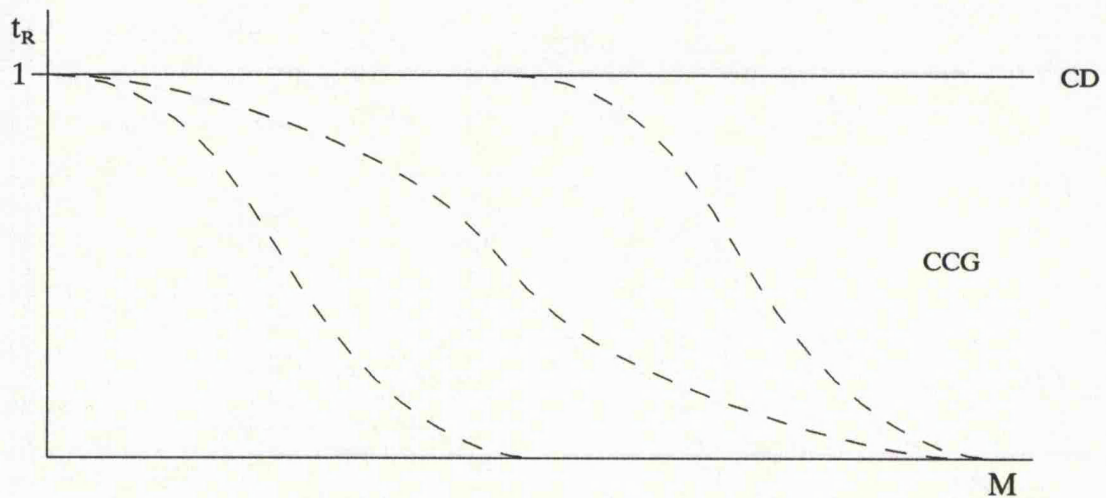
Figure 5.7. A Schematic representation of how the failure time ratio, t_R would be expected to vary with applied bending moment, M. At low moments the failure is by continuum damage (CD) and the failure time ratio is asymptotic to unity. At higher moments failure is by creep crack growth (CCG) until at the ultimate moment the specimen fails instantaneously upon loading.

The precise shape of the transition curve from CD to CCG would vary from one material and test configuration to another.

PLAN

115.0

10.0

13.0

42.5   30.0

ELEVATION

R 2.0mm

1.0mm

NOTCH DETAIL
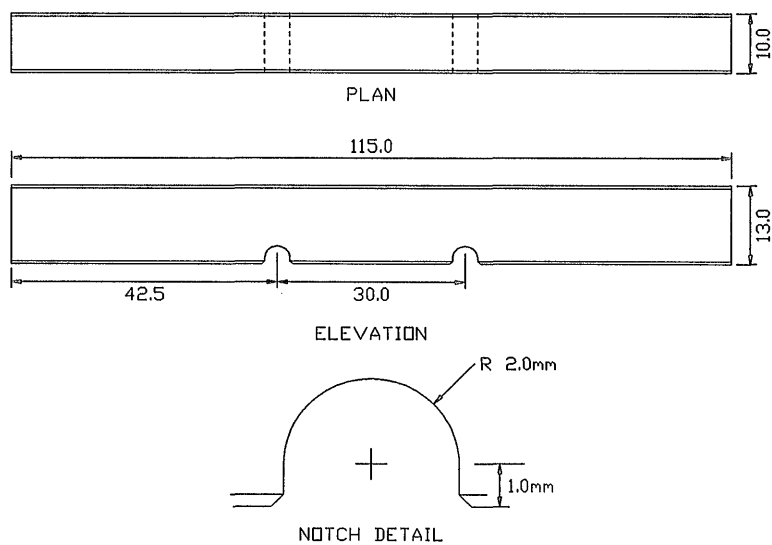
Figure 5.8. Notched specimen ('N type' specimen) geometry. The specimen is shown in the orientation used in testing.

PLAN

10.0

47.0

115.0

10.0

R 5.0mm

ELEVATION
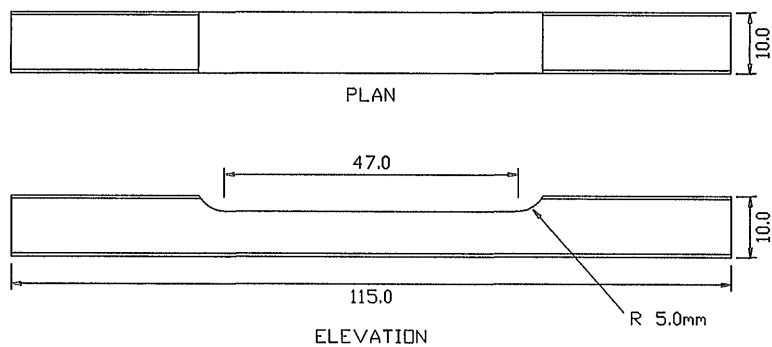
Figure 5.9. Profiled specimen ('P type' specimen) geometry. The profile was achieved by diamond grinding 10mm x 10mm chamfered bars. The specimen is shown in the orientation used in testing. The machined surface is in compression so that the critical tensile surface is in the same as received state as the notched specimens.
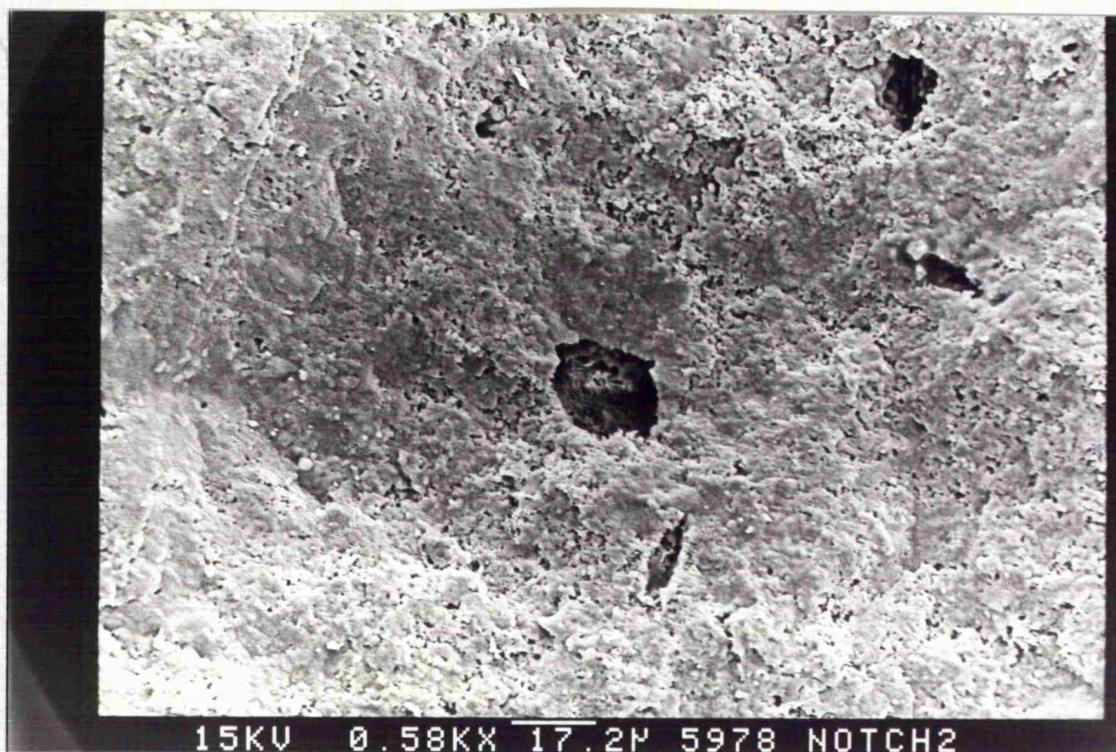
Plate 5.1a. An electron micrograph at 580x magnification of a typical fracture surface of a RBSN specimen (no. N2). This specimen was bent in 3-point bending at the notch at room temperature.

Plate 5.1b. A close-up of the pre-existing cavity in the same specimen at 1770x magnification. Note the partially crystalline partially amorphous structure.
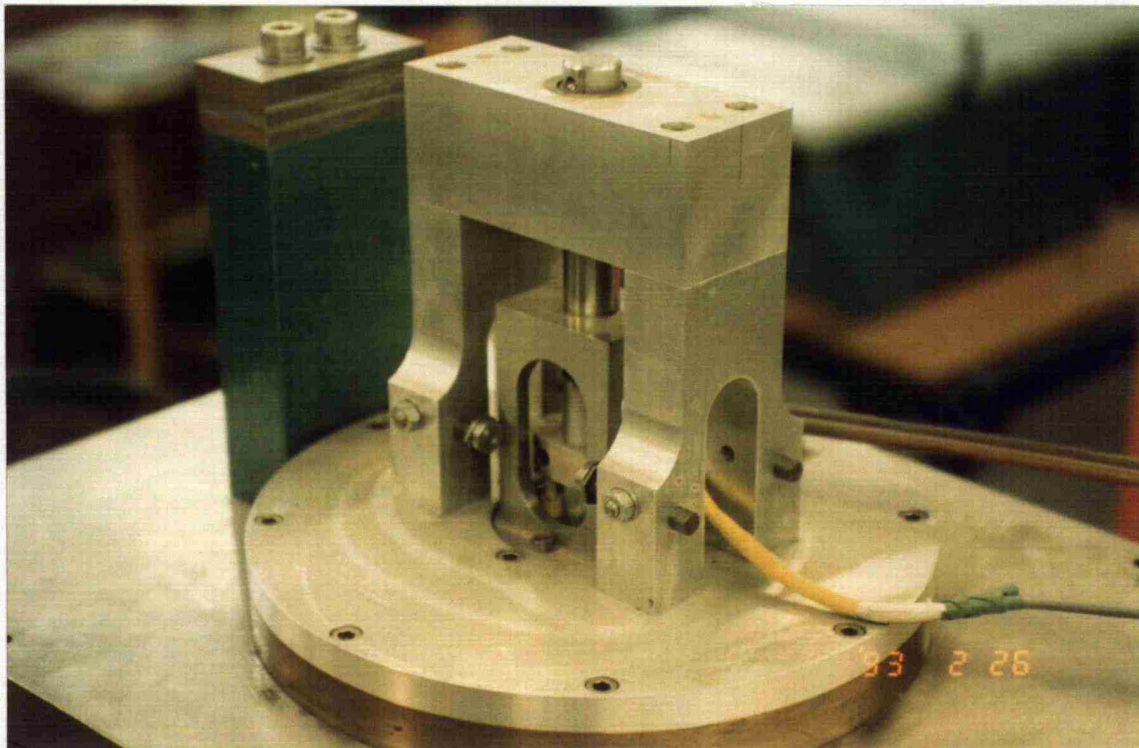
Plate 5.2. The upper load train and guide, note the outer alumina extensometer rods just visible in the LVDT holder.
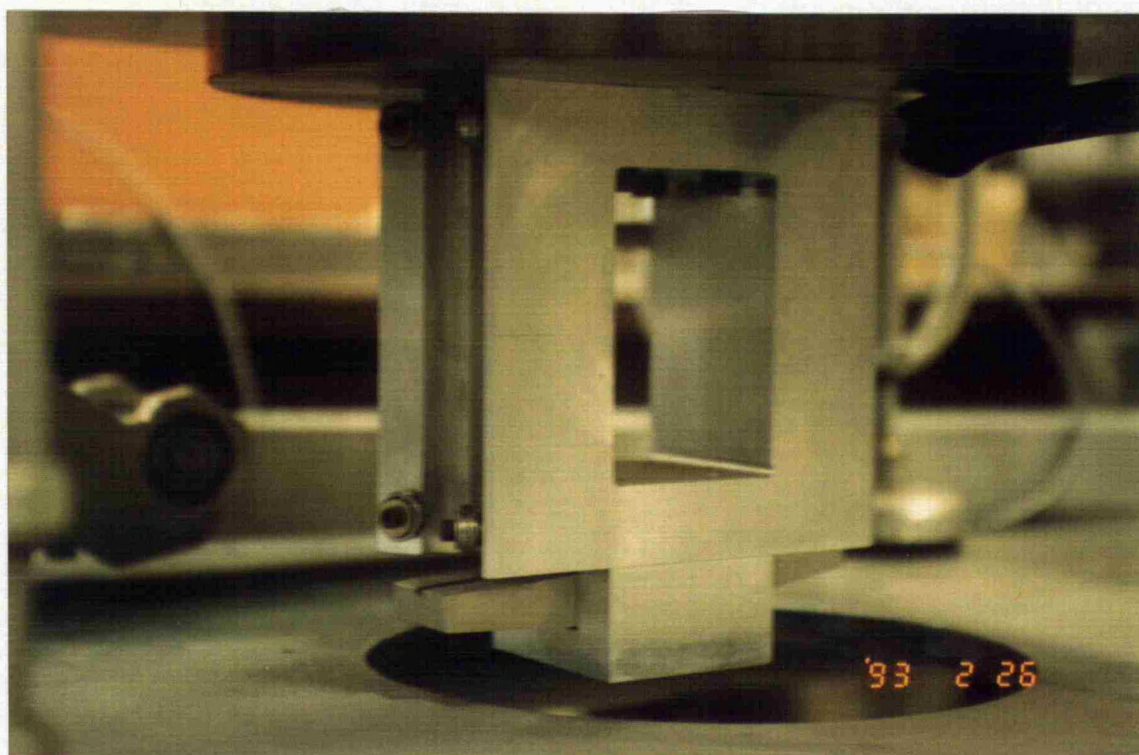
Plate 5.3. The lower rocker assembly.
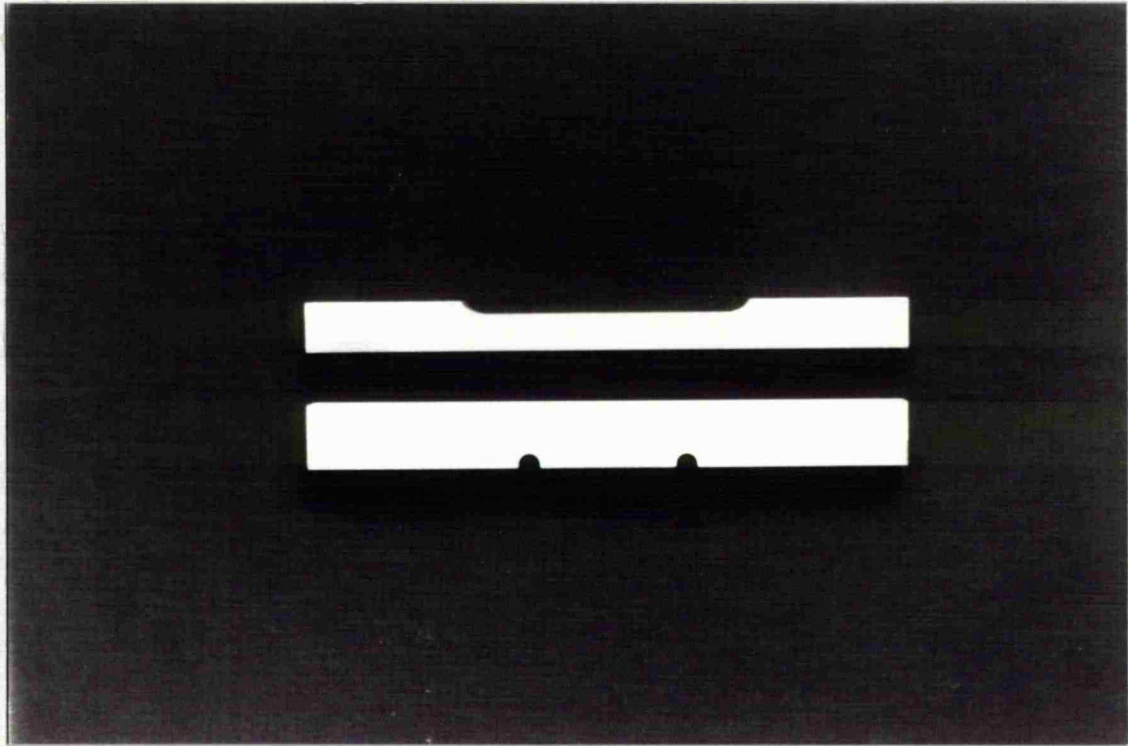
Plate 5.4. Untested profiled and notched specimens. The dimensions of these specimens are given in Figures 5.8 and 5.9.
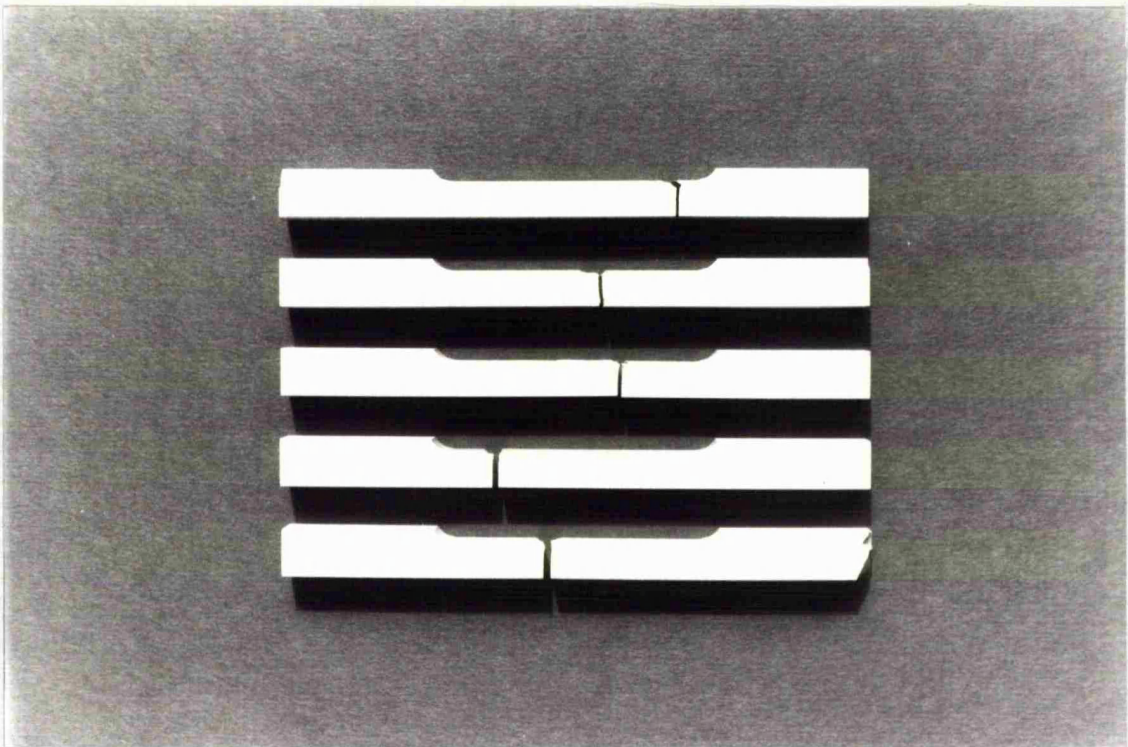
Plate 5.5. From the top specimens P7, P24, P10, P18, and P19 showing a reasonably even distribution of failure location over the gauge length.
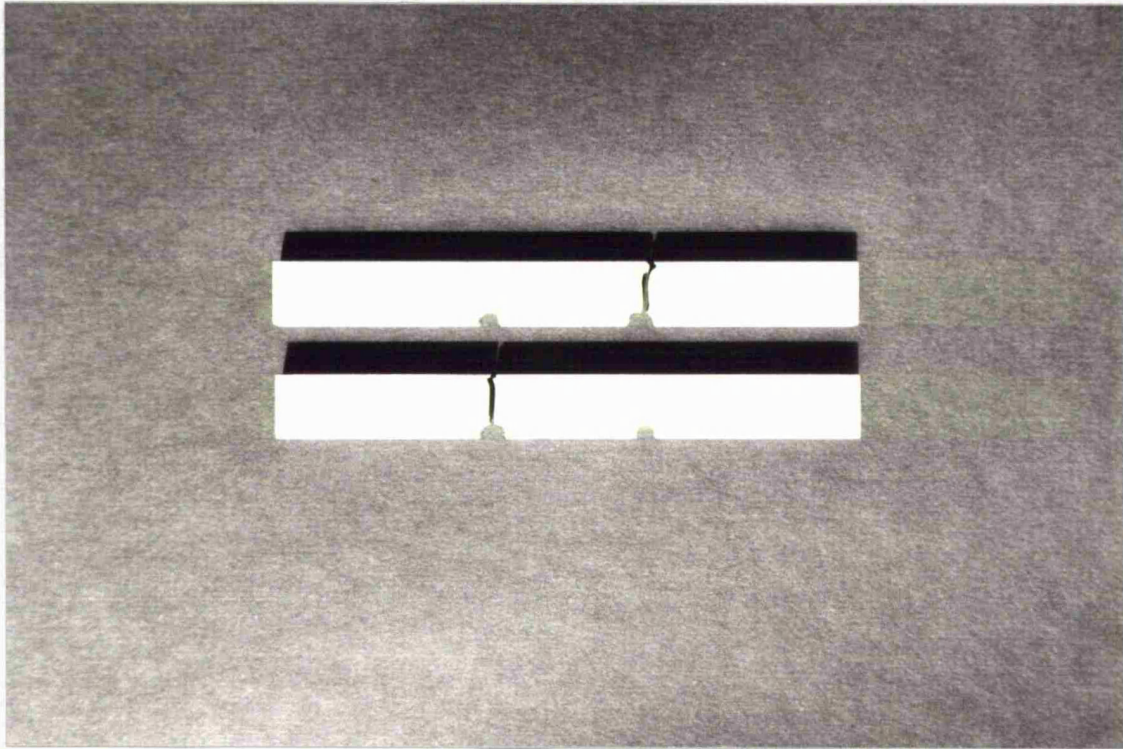
Plate 5.6a. From the top specimens N21 and N20. These specimens were rapidly loaded to failure to determine the ULS capacity of a notched specimen.
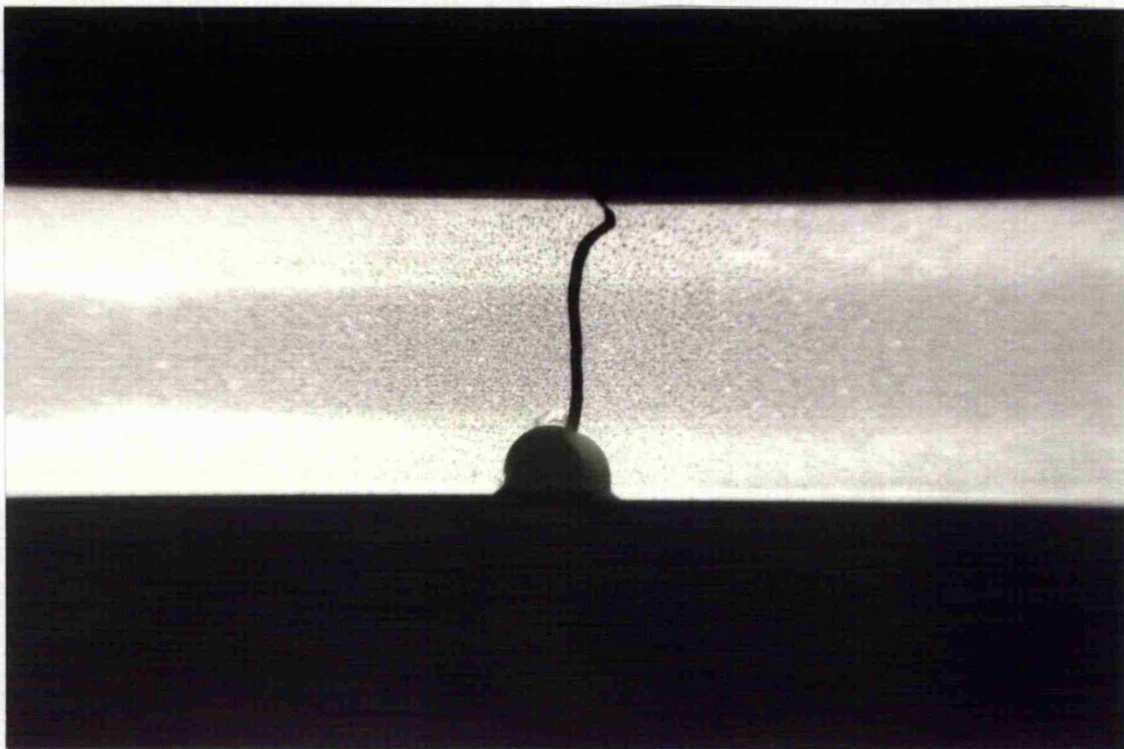
Plate 5.6b. A close-up of the failure of N20 seen from behind, as viewed in the rig. This 'tongue and groove' failure is typical of a brittle flexural failure.
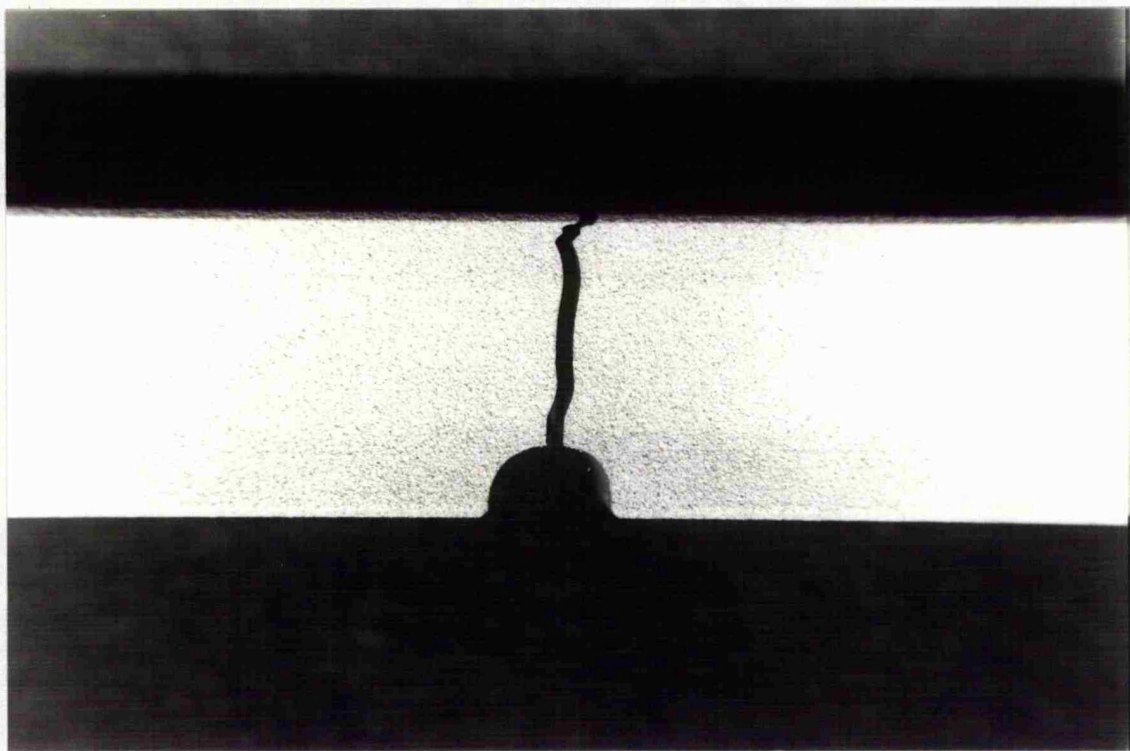
Plate 5.7. A close-up of the failure of N11. This specimen failed after 4.8 minutes.
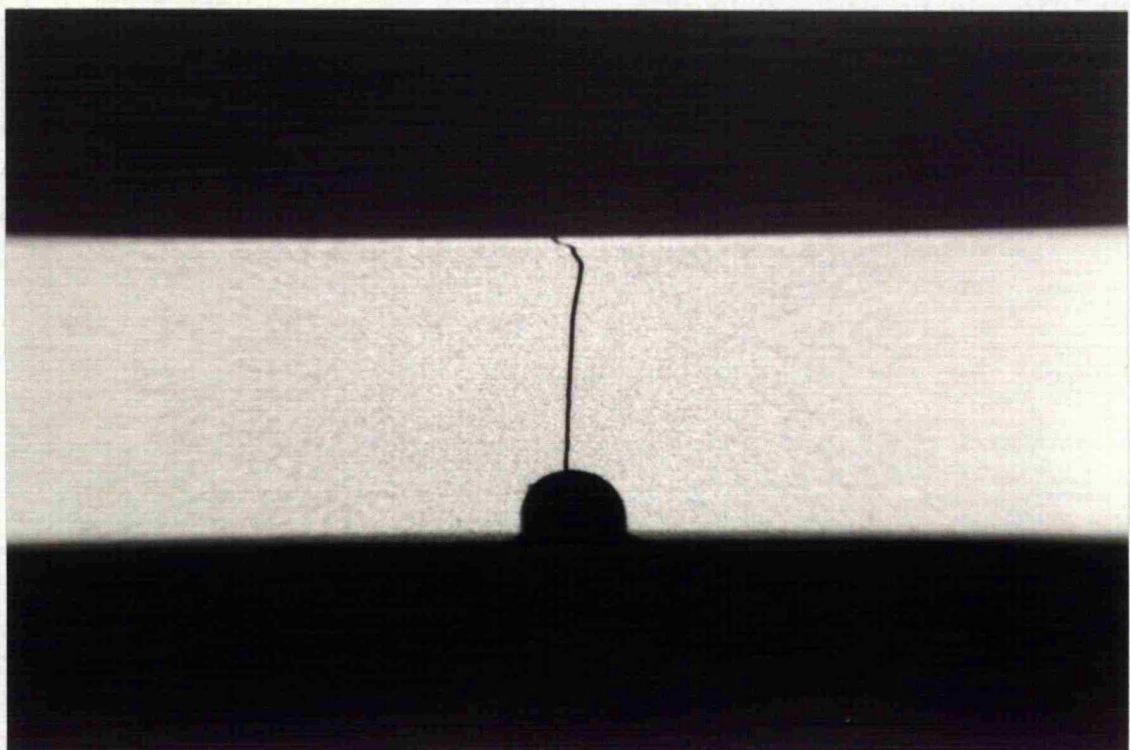
Plate 5.8. A close-up of the failure of N17 which failed after 2.80 hours.
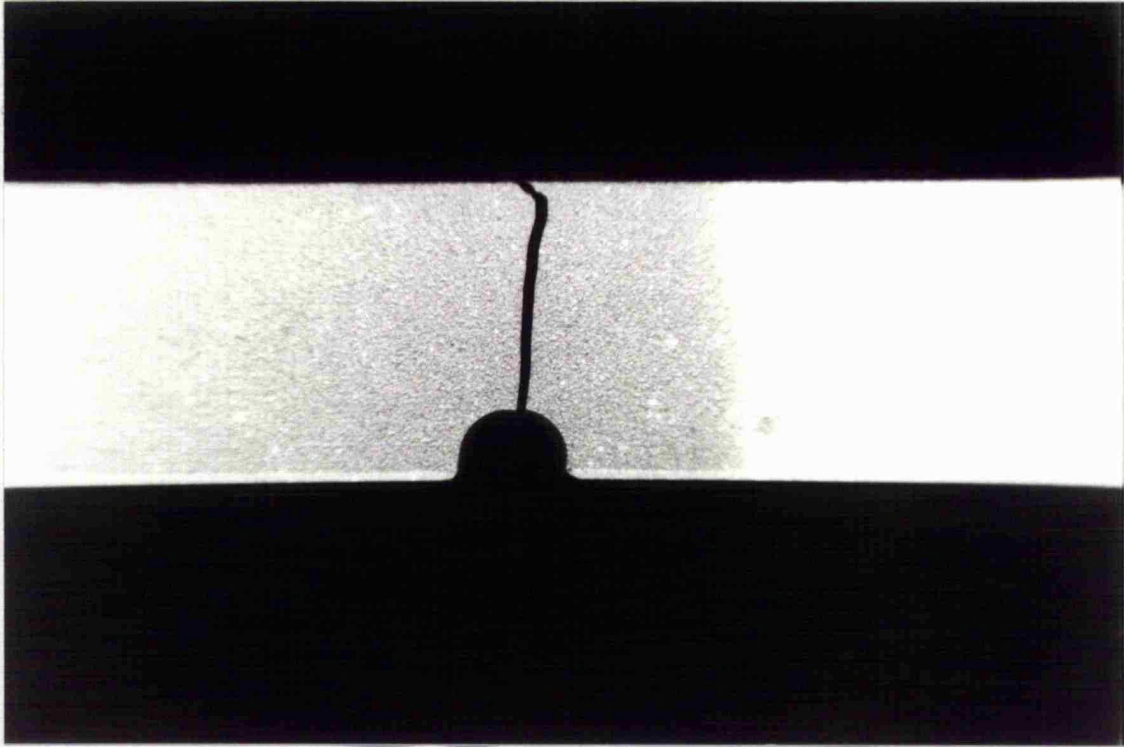
Plate 5.9. A close-up of the failure of N19 which failed after 1.3 hours. Plates 5.7, 5.8 and 5.9 all represent different failure times but they are all similar to the instantaneous failure of Plate 5.6b.
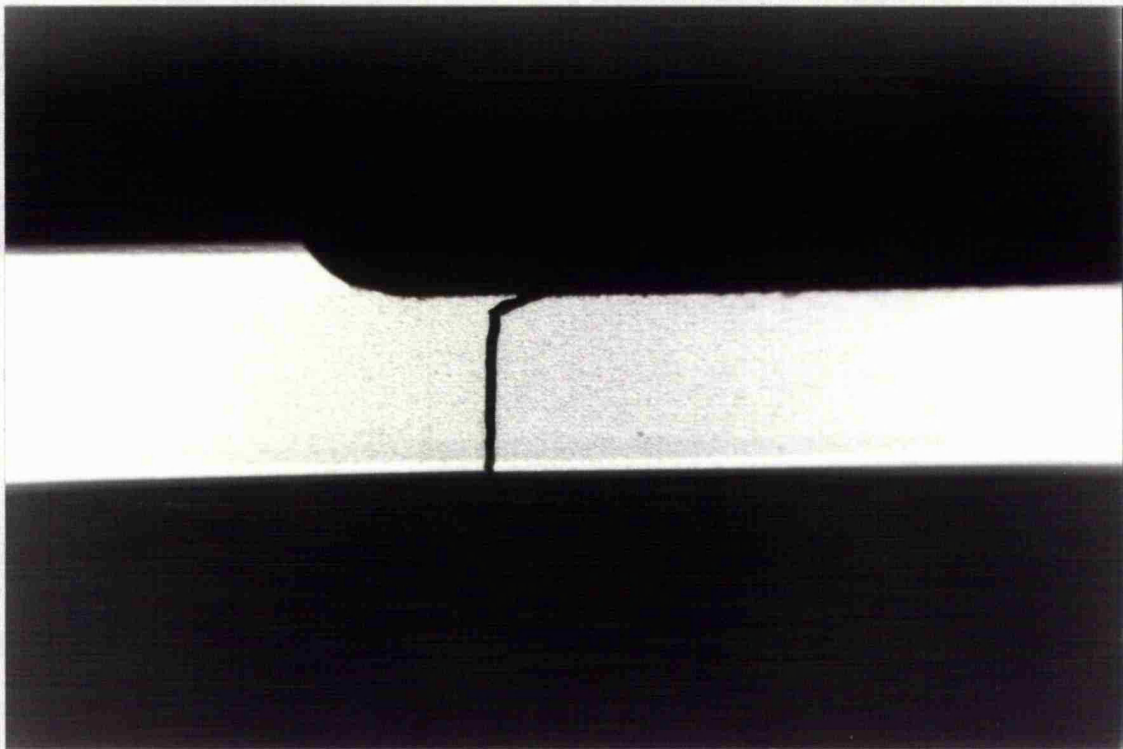
Plate 5.10. A close-up of a typical failure in a profiled specimen (this one is of P7) also displaying the characteristic brittle failure.
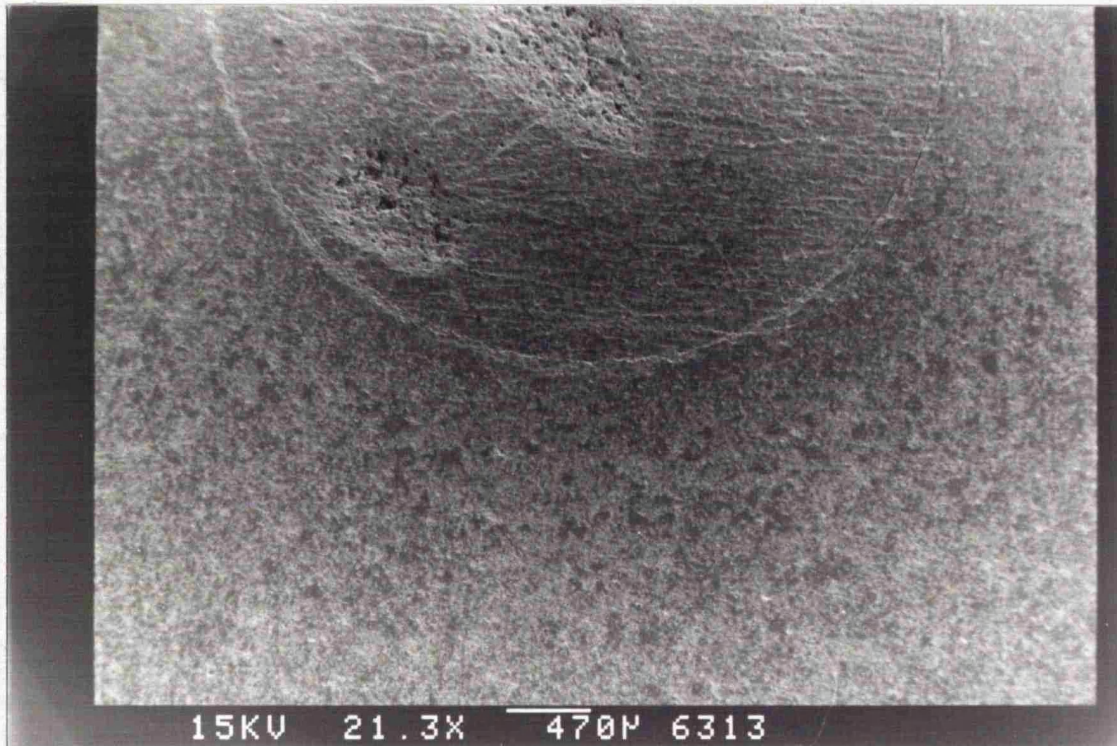
Plate 5.11a. An electron micrograph at 21x magnification of the unfailed notch of N8. The notch is clearly visible in the centre of the picture.
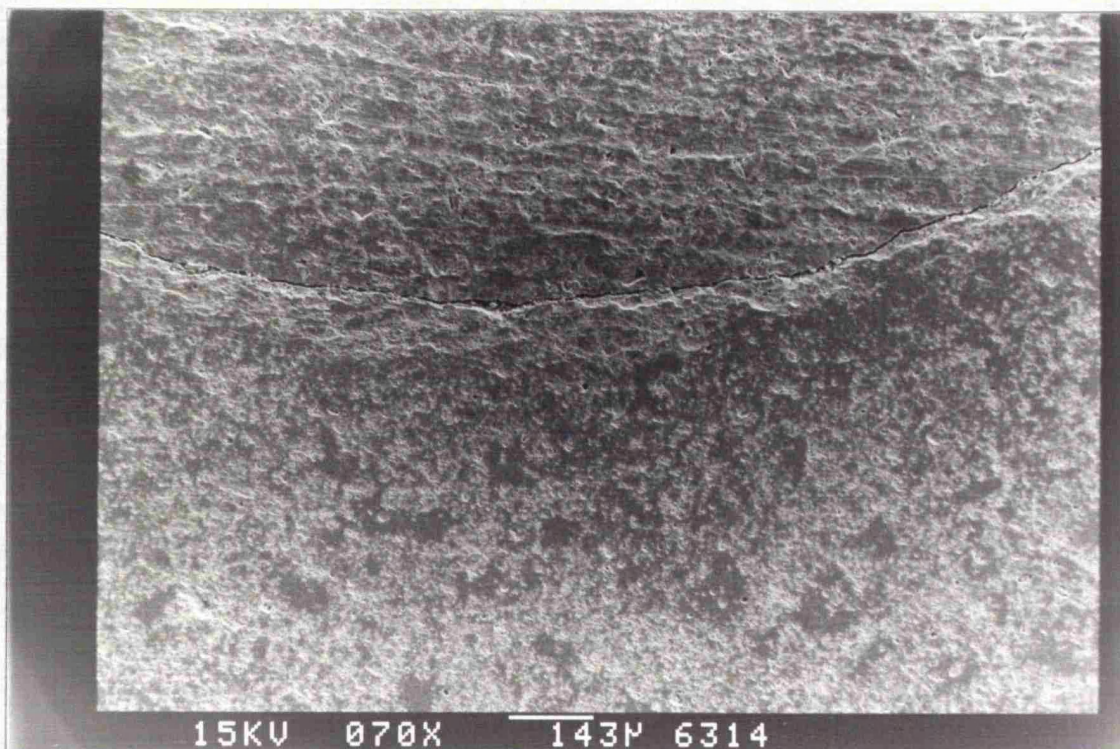
Plate 5.11b. The same notch at 70x magnification.
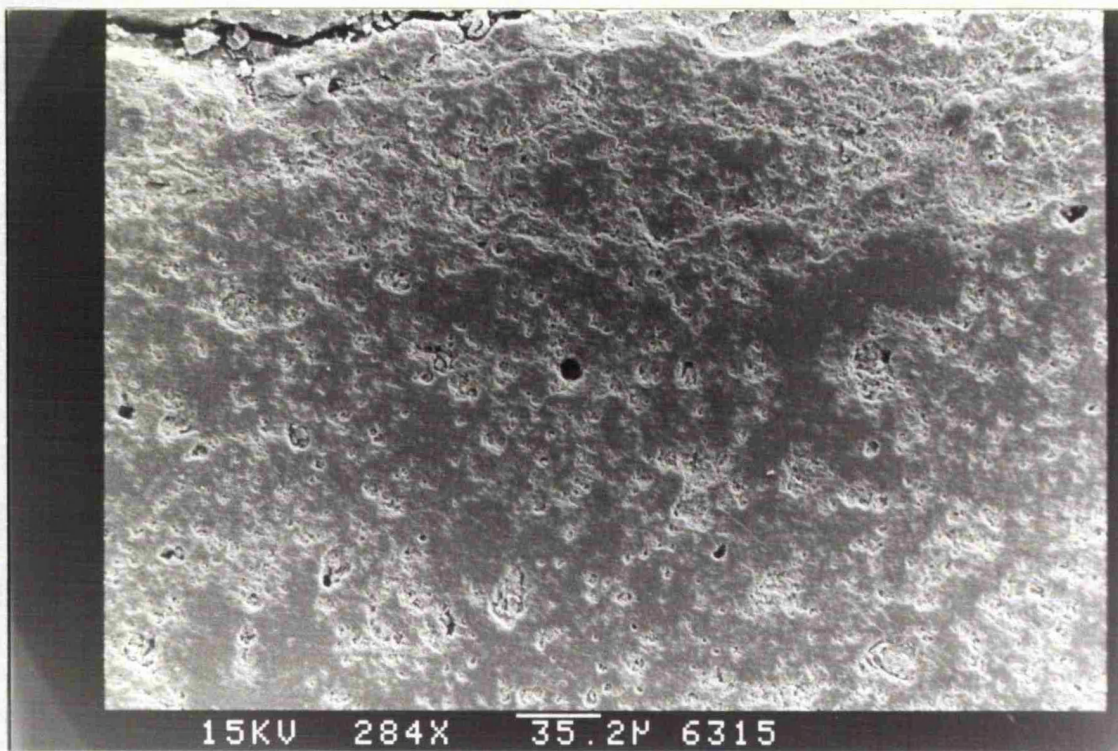
Plate 5.11c. The same notch at 284x magnification.
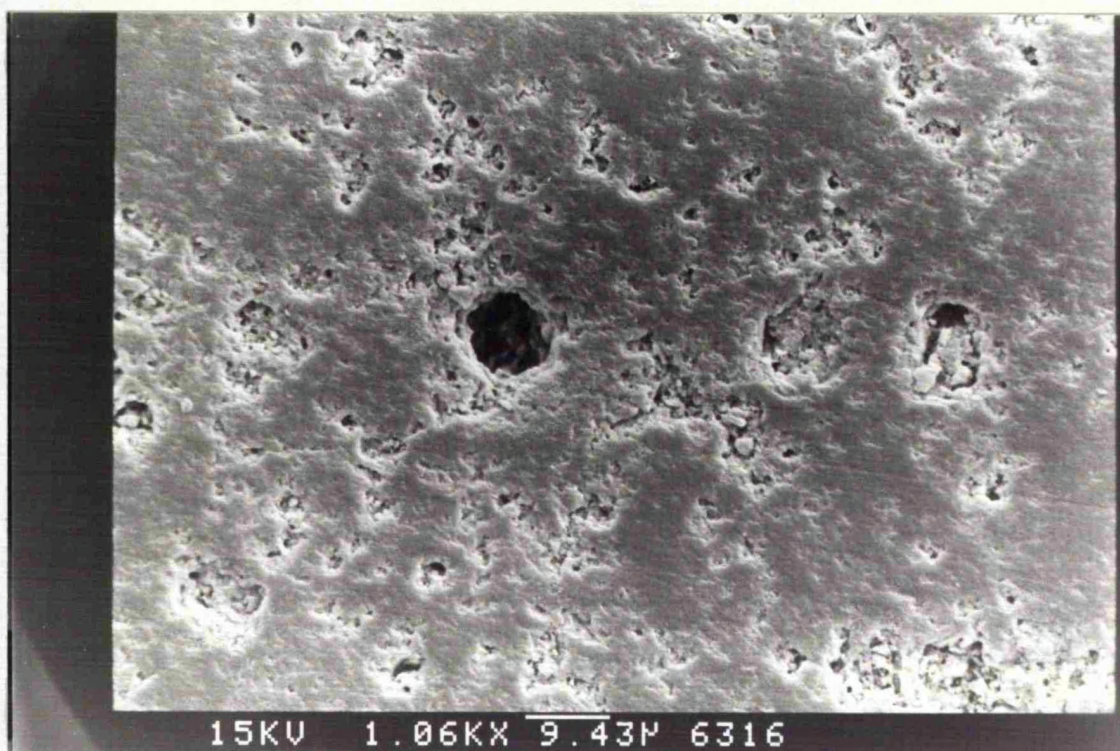
Plate 5.11d. The same notch at 1060x magnification. In an originally fully dense material the void in the centre of the picture would be proof of diffusive cavitation. However this void is similar to the pre-existing void shown in Plate 5.1b. There is no apparent difference between the porosity of this specimen which was tested for 400 hours and the as received material.
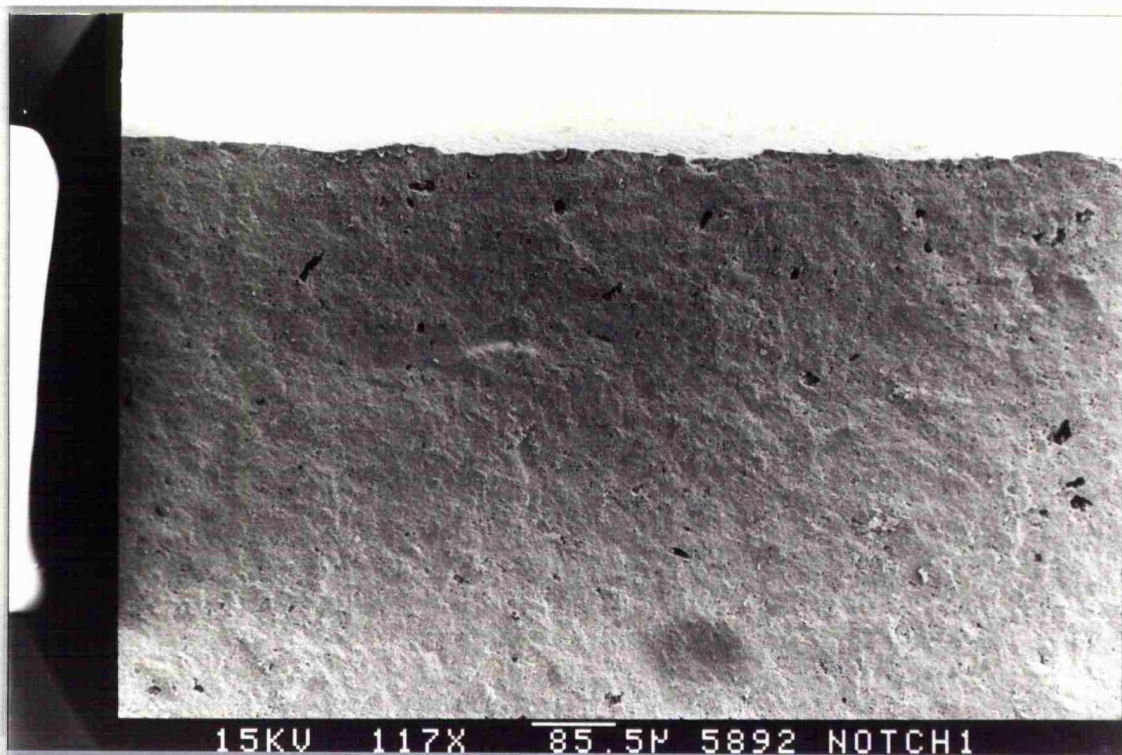
Plate 5.12a. An electron micrograph at 117x magnification of the failure surface at the top of the notch of N24. This specimen failed after 2.25 hours.
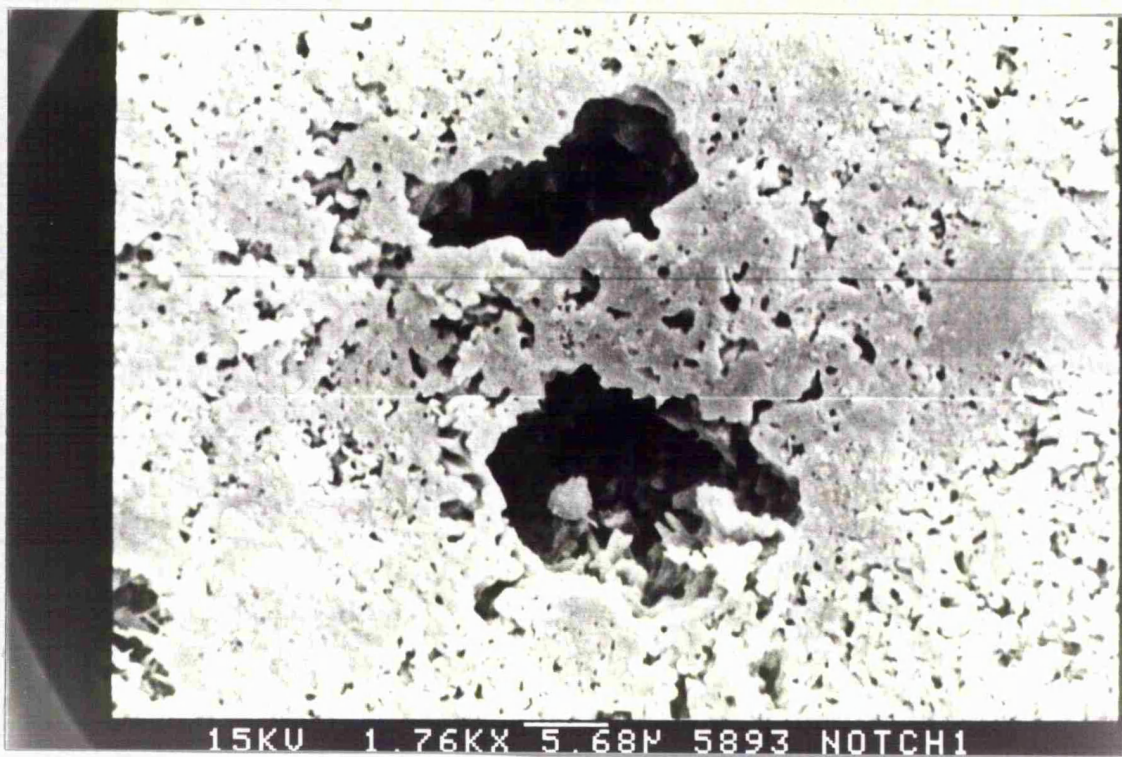
Plate 5.12b. A close-up at 1760x magnification of the centre right of the previous Plate. The structure appears to be rather less crystalline than the as received material. This is probably due to the effect of sintering.

APPENDIX 1

In this Appendix we demonstrate the validity of the approximation to the HR field given in equation (3.5).

Consider a bar of elastic/creeping material loaded in uniaxial tension to an initial stress σ_i and then rigidly restrained. The total strain in the bar at any time is the sum of the elastic and creep strains, ie.

$$\varepsilon_T = \varepsilon_e + \varepsilon_c \tag{A1.1}$$

Since the total strain is constant, by virtue of the rigid restraint, then

$$\frac{d\varepsilon_T}{dt} = \frac{d\varepsilon_e}{dt} + \frac{d\varepsilon_c}{dt} = \frac{1}{E}\frac{d\sigma}{dt} + \left(\frac{\sigma}{\sigma_0}\right)^n \frac{d\dot{\varepsilon}_o}{dt} = 0 \tag{A1.2}$$

and so

$$\frac{d\sigma}{dt} = \frac{-\dot{\varepsilon}_0 E}{\sigma_0^n} \sigma^n \tag{A1.3}$$

Integrating between $\sigma = \sigma_i$ at time $t = 0$, and $\sigma = \sigma$ at $t = t$ we find

$$\frac{1}{(n-1)}\left[\frac{1}{\sigma^{n-1}} - \frac{1}{\sigma_i^{n-1}}\right] = \frac{\dot{\varepsilon}_0 E t}{\sigma_0^n} \tag{A1.4}$$

Now it is apparent from equation (A1.4) that σ need be only slightly less than σ_i for the first term in the square brackets to dominate, and so we may write

$$\sigma \approx \left[\frac{(n-1)\dot{\varepsilon}_0 E t}{\sigma_0^n}\right]^{\frac{1}{n-1}} \tag{A1.5}$$

Hui and Riedel[55] have demonstrated that for a growing crack in a material for which $n > 3$ the stress field ahead of the crack is of the form

$$\sigma = B r^{-\frac{1}{n-1}} \qquad\qquad (A1.6)$$

now if we consider a distance δa from the crack tip, the stress is (assuming a coordinate system that moves with the crack tip)

$$\sigma = B(\delta a)^{-\frac{1}{n-1}} \qquad\qquad (A1.7)$$

Initially the stress at δa increases above that predicted by equation (A1.7) due to elastic effects. The time taken for the stress to relax to this predicted value can be calculated from equation (A1.5) as

$$\delta t = \frac{\sigma_0^n}{(n-1)\dot{e}_0 E \sigma^{n-1}} \qquad\qquad (A1.8)$$

If we now substitute for σ from equation (A1.7) we see that B is given by

$$B = \left[\frac{\sigma_0^n}{(n-1)\dot{e}_0 E} \frac{da}{dt} \right]^{\frac{1}{n-1}} \qquad\qquad (A1.9)$$

so
$$\sigma = \left(\frac{1}{n-1}\right)^{\frac{1}{n-1}} \left[\frac{\sigma_0^n}{\dot{e}_0 E} \frac{da}{dt} \right]^{\frac{1}{n-1}} r^{-\frac{1}{n-1}} \qquad\qquad (A1.10)$$

This is the same expression as that derived by Hui and Riedel, except for the first term. They present a constant α_n which they determine numerically; this takes the value 0.815 for $n=4$ (compared with 0.693 for the above) and 1.064 for $n=6$ (compared with 0.725).

APPENDIX 2

In this Appendix we determine the characteristic lengths, χ, of four specimen geometries commonly used in creep testing: the compact tension specimen, double edge cracked plate, centre cracked plate and double cantilever beam.

A)   The Compact Tension Specimen; (a/W = ½); specimen thickness = B.
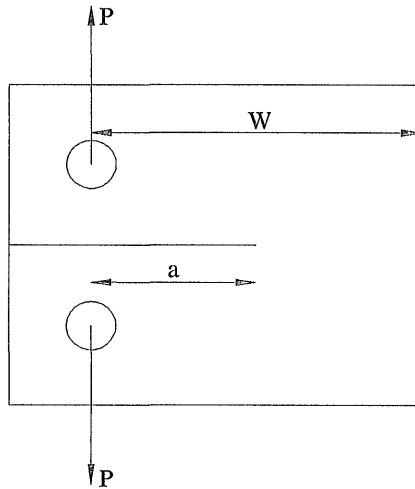
The plane strain limit load, P_L, is given by

$$P_L = 0.129\, B W \sigma_y \qquad \text{(A2.1)}$$

From equation (2.16) it is therefore apparent that the reference stress σ_0 is given by

$$\sigma_0 = \frac{P}{0.129\, B W} \qquad \text{(A2.2)}$$

The mode one stress intensity factor, K_I is given by[104]

$$K_I = \frac{P}{B\sqrt{W}} \left[29.6 \left(\frac{a}{w}\right)^{\frac{1}{2}} - 185.6 \left(\frac{a}{w}\right)^{\frac{3}{2}} + etc. \right] \approx \frac{9.61 P}{B\sqrt{W}} \qquad \text{(A2.3)}$$

Therefore from equation (3.25)

$$\chi = 2.31\, a \qquad \text{(A2.4)}$$

B) The Double Edge Cracked Plate; (a/W = ¼); plate thickness = B.
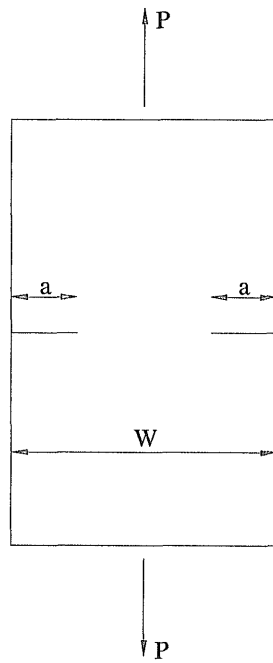
The plane strain limit load, P_L, is given by

$$P_L = 0.8\,BW\sigma_y \qquad \text{(A2.5)}$$

Therefore, from equation (2.16), the reference stress, σ_0, is

$$\sigma_0 = \frac{P}{0.8\,BW} \qquad \text{(A2.6)}$$

The mode one stress intensity factor, K_I is given by[104]

$$K_I = 2.0775\,\frac{P\sqrt{a}}{BW} \qquad \text{(A2.7)}$$

Therefore from equation (3.25)

$$\chi = 2.07\,a \qquad \text{(A2.8)}$$

C) Centre Cracked Plate; (a/W = ¼); plate thickness = B.
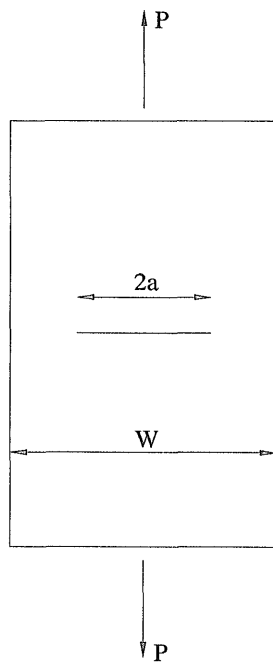
The plane strain limit load, P_L, is given by

$$P_L = \frac{2}{\sqrt{3}}\,\sigma_y B W \left(1 - \frac{2a}{W} \right) \tag{A2.9}$$

Therefore, from equation (2.16), the reference stress, σ_0, is

$$\sigma_0 = \frac{\sqrt{3}\,P}{BW} \tag{A2.10}$$

The mode one stress intensity factor, K_I is given by[104]

$$K_I = \frac{P}{BW}\sqrt{\pi a}\left(\sec \frac{\pi a}{W} \right)^{\frac{1}{2}} \tag{A2.11}$$

Therefore from equation (3.25)

$$\chi = 1.11\,a \tag{A2.12}$$

D) The Double Cantilever Beam; specimen thickness = B.
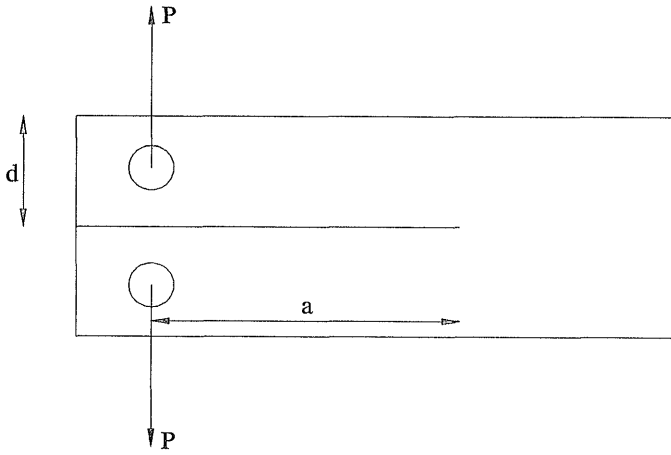
The plane strain limit load, P_L, is given by

$$P_L = \frac{2}{4\sqrt{3}} \frac{Bd^2 \sigma_y}{a} \tag{A2.13}$$

Therefore, from equation (2.16), the reference stress, σ_0, is

$$\sigma_0 = \frac{2\sqrt{3}\,P\,(a/d)}{Bd} \tag{A2.14}$$

The mode one stress intensity factor, K_I is given by[104]

$$K_I = \frac{2\sqrt{3}\,P}{B\sqrt{d}} \left(\frac{a}{d} + 0.7 \right) \tag{A2.15}$$

Therefore from equation (3.25)

$$\chi = \frac{0.75 \left(\dfrac{(a/d) + 0.7}{\sqrt{d}} \right)^2}{\left(\dfrac{(a/d)}{d} \right)^2} \tag{A2.16}$$

APPENDIX 3

In this Appendix we convert the results derived in Chapter four to a form for comparison with those of a model due to Thouless et. al.[35].

A) Constrained Creep.

Recall equation (4.19), we have

$$\bar{a} = \frac{3(n+1)f_3^{\frac{-n}{n+1}} \bar{R}^{\frac{n+2}{n+1}}}{(n+2)\pi\bar{\lambda}(F_2^2-F_1^2)} \tag{A3.1}$$

Thouless' model is only valid for the case of linear viscosity, ie. n = 1. for which $f_3 = \pi/3$[50] and so in full form, noting the definitions of the nondimensional groups given in equations (4.16), (4.17) and (4.18)

$$\frac{\dot{a}\sigma_0}{C^*} = \frac{6\left(\frac{\pi}{3}\right)^{-\frac{1}{2}}\left(\frac{R\sigma_0\dot{e}_o}{C^*}\right)^{\frac{3}{2}}}{3\pi\left(\frac{\lambda\sigma_0\dot{e}_0}{C^*}\right)(F_2^2-F_1^2)} \tag{A3.2}$$

Remembering that the material viscosity, $\eta = \sigma_0/\dot{\epsilon}_0$ and also remembering that we are assuming Thouless' form of the equation, $K^2 = \eta C^*$, we can see that

$$\frac{\eta\dot{a}}{K\sqrt{l}} = \frac{6\left(\frac{\pi}{3}\right)^{-\frac{1}{2}}\left(\frac{R\sigma_0\dot{e}_o\eta}{K^2}\right)^{\frac{3}{2}}}{3\pi\left(\frac{\lambda\sigma_0\dot{e}_0\eta}{K^2}\right)(F_2^2-F_1^2)}\frac{K}{\sigma_0\sqrt{l}} \tag{A3.3}$$

and therefore
$$\frac{\eta\dot{a}}{K\sqrt{l}} = \frac{2(\pi/3)^{-\frac{1}{2}}}{\pi}\frac{R^{\frac{3}{2}}}{\lambda\sqrt{l}(F_2^2-F_1^2)} \tag{A3.4}$$

If we assume a constant grain size, l, then the damage zone size R = zl, where z is the number of grains in the damage zone. If we further assume that the voids are very small at nucleation then

Page 177

$$\frac{\eta \dot{a}}{K\sqrt{l}} = \frac{2(\pi/3)^{-\frac{1}{2}}}{\pi} \frac{(l/\lambda)}{F_2^2} z^{\frac{3}{2}} \qquad (A3.5)$$

B) Linear variation of diplacement rate through the damage zone.

From equation (4.51) we have

$$\dot{a} = \frac{3R}{8\lambda(F_2 - F_1)} \left[\frac{3C^* \lambda \phi_0 \dot{e}_0}{A_0 \sigma_0} \right]^{\frac{1}{2}} \qquad (A3.6)$$

Recalling equation (4.24)

$$\phi_0 = \frac{2\Omega D_b \delta_b \sigma_0}{kT\lambda^3 \dot{e}_0} \qquad (A3.7)$$

ie.

$$\phi_0 = \frac{2\Omega D_b \delta_b}{kT\lambda^3} \eta \qquad (A3.8)$$

Now it is known that[105]

$$\eta = \frac{kTl^3}{12\pi\Omega D_b \delta_b} \qquad (A3.9)$$

therefore

$$\phi_0 = \frac{(l/\lambda)^3}{6\pi} \qquad (A3.10)$$

Making the same substitutions as before for the material viscosity and C^*, and again assuming that at nucleation the voids are small, we find

$$\frac{\eta \dot{a}}{K\sqrt{l}} = \frac{3\sqrt{3}}{8F_2\sqrt{6\pi A_0}} \left(\frac{l}{\lambda}\right)^2 z \qquad (A3.11)$$

C) Unconstrained creep growth.

From equation (4.30) we have

$$\dot{a} = \frac{3\,\phi_0}{4\,G(F)} \; \frac{n+1}{n} \left(\frac{\dot{e}_0^n C^*}{I_n \sigma_0} \right)^{\frac{1}{n+1}} \sigma_{ij}(\theta) \, R^{\frac{n}{n+1}} \qquad (A3.12)$$

recall from equation (3.4) that

$$I_n = \frac{(n+1)\,\pi}{n} \qquad (A3.13)$$

under both plane stress and plane strain. Combining equations (A3.12) and (A3.13) and making the usual substitutions for viscosity and C^* we find that

$$\frac{\eta\,\dot{a}}{K\sqrt{l}} = \frac{(l/\lambda)^3}{4\,\pi\,\sqrt{2\,\pi}\,G(F)} \; \sigma_{ij}(\theta) \, z^{\frac{1}{2}} \qquad (A3.14)$$

Under plane stress conditions $\qquad \sigma_{ij}(\theta) = 1 \qquad (A3.15)$

whereas we can see from equation (4.32) that in plane strain, if n = 1, then

$$\sigma_{ij}(\theta) = 2/\sqrt{3} \qquad (A3.16)$$

APPENDIX 4

In this Appendix we prove that in a damaged material C* *is* path dependent. Recall the definition given earlier of the nominally path independent integral C*

$$C^* = \oint_\Gamma \left(\bar{W} dx_2 - \tilde{T}_i \frac{d\dot{u}_i}{dx_1} ds \right) \qquad (A4.1)$$

where

$$\bar{W} = \int \sigma_{ij} d\dot{e}_{ij} \qquad (A4.2)$$

Consider a closed contour Γ around a crack tip enclosing undamaged material (see Figure A4.1). When evaluated around this contour, by definition, C* = 0. Along the surfaces of the crack (along a-b and c-d) the traction, normal to the surface, is zero ie. $\tilde{T}_i$ = 0, dx_1 also equals zero. This means that the contribution to C* along these two elements of the contour is zero. Now consider two separate contours Γ_1 and Γ_2 which follow the same path as Γ (see Figure A4.2). It follows from what has gone before that values of C* determined by integrating in the *same direction* around the two different contours will be equal. We will now show that this is not the case if the region enclosed by the contour Γ contains damaged material.

If $\overline{W}$ is some function of the damage, F, as well as of strain rate, i.e.

$$\bar{W} = \bar{W}(F, \dot{e}) \qquad (A4.3)$$

then

$$d\bar{W} = \frac{\partial \bar{W}}{\partial F} dF + \sigma_{ij} d\dot{e}_{ij} \qquad (A4.4)$$

The difference in the values of C^* evaluated on the two different contours is

$$C_1^* - C_2^* = \oint_{\Gamma_1-\Gamma_2} \left(\bar{W} dx_2 - \tilde{T}_i \frac{\partial \dot{u}_i}{\partial x_1} ds \right) \qquad (A4.5)$$

Now, for a continuous function $G(x)$, whose first and second derivatives are also continuous, Gauss' theorem states that

$$\int_A \frac{\partial G}{\partial x_1} dx_1 dx_2 = \int_\Gamma G dx_2 \qquad (A4.6)$$

Applying Gauss' law to the first term in equation (A4.5) yields the result

$$\int_{\Gamma_1-\Gamma_2} \bar{W} dx_2 = \int_A \frac{\partial \bar{W}}{\partial x_1} dx_1 dx_2 \qquad (A4.7)$$

Consider the second term in equation (A4.5) remembering that $\tilde{T}_i = \sigma_{ij} n_j$ and remembering that

$$\int_{\Gamma_1-\Gamma_2} \tilde{T}_i \frac{\partial \dot{u}_i}{\partial x_1} ds = \int_{\Gamma_1-\Gamma_2} \sigma_{ij} n_j \frac{\partial \dot{u}_i}{\partial x_1} ds \equiv I \qquad (A4.8)$$

From similar triangles it is apparent that $n_j ds = dx_j$. Applying Gauss' law gives

$$\therefore \quad I = \int_A \left(\frac{\partial \sigma_{ij}}{\partial x_j} \frac{\partial \dot{u}_i}{\partial x_1} + \sigma_{ij} \frac{\partial^2 \dot{u}_i}{\partial x_1 \partial x_j} \right) dx_1 dx_2 \qquad (A4.9)$$

but from equilibrium

$$\frac{\partial \sigma_{ij}}{\partial x_j} = 0 \qquad (A4.10)$$

so we obtain

$$I = \int_A \sigma_{ij} \frac{\partial}{\partial x_1} \left[\frac{\partial \dot{u}_i}{\partial x_j} \right] dx_1 dx_2 \qquad (A4.11)$$

The term in the square brackets in equation (A4.11) is effectively the strain rate tensor, $\dot{\varepsilon}_{ij}$ so

$$\therefore \quad I = \int_A \sigma_{ij} \frac{\partial \dot{e}_{ij}}{\partial x_1} dx_1 \, dx_2 \qquad (A4.12)$$

Combining equations (A4.7) and (A4.12) with (A4.5) gives

$$C_1^* - C_2^* = \int_A \left(\frac{\partial \overline{W}}{\partial x_1} - \sigma_{ij} \frac{\partial \dot{e}_{ij}}{\partial x_1} \right) dx_1 \, dx_2 \qquad (A4.13)$$

We can see from this that for an undamaged material where $\sigma_{ij} \, \partial \dot{\varepsilon}_{ij} = \partial \overline{W}$ equation (A4.13) equals zero, as it should. However if equation (A4.4) holds then we obtain the result that

$$C_1^* - C_2^* = \int_A \frac{\partial \overline{W}}{\partial F} \frac{dF}{dx_1} dx_1 \, dx_2 \qquad (A4.14)$$

and from this we can see that the C^* integral is only path independent provided that the damage within the contour around which it is evaluated is constant ie.

$$\frac{dF}{dx_1} = 0 \qquad (A4.15)$$
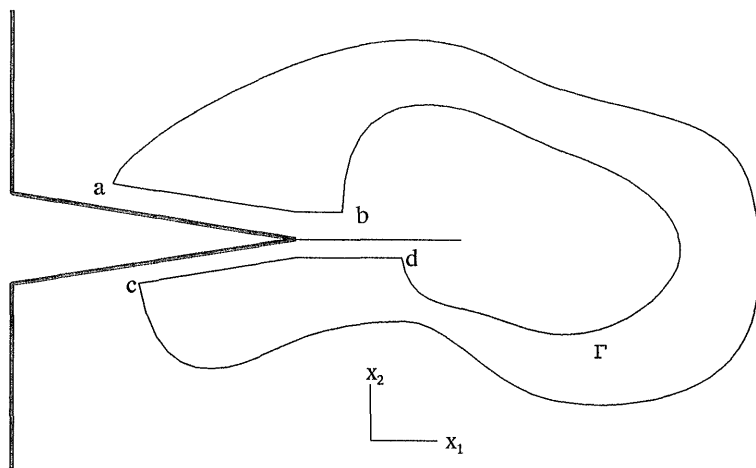
Figure A4.1 A closed contour Γ around a crack tip (the distance from the crack of a-b and c-d is exaggerated for clarity) in a body subjected to a stress field σ_{ij}. The contributions towards C* along a-b and c-d are both zero.
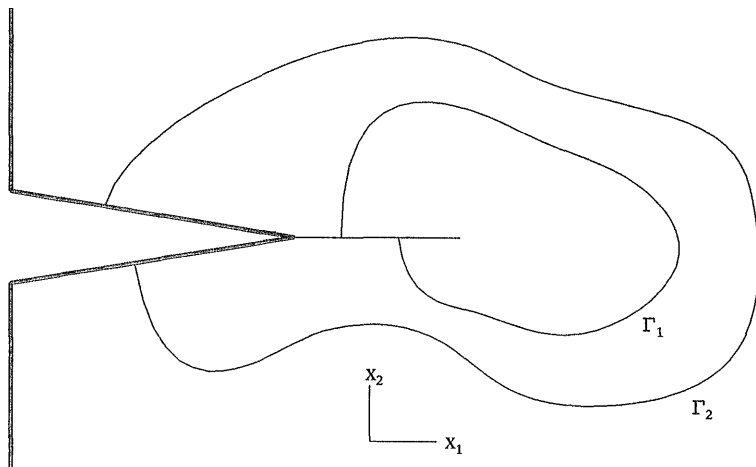
Figure A4.2 Two discrete contours Γ_1 and Γ_2 following the same path as b-d and a-c respectively. C* evaluated along both contours is the same provided that any damage enclosed by the contours is constant with x_1.

APPENDIX 5

In this Appendix we determine the form of the displacement rate field which is implied in the model of Thouless et. al[35]. Thouless derives an expression for the constraining stress on the mth grain in a damage zone of z grains, $\sigma_{c,m}$ as

$$\sigma_{c,m} = \frac{2\eta}{3\pi l\sqrt{2m-1}} \sum_{n=1}^{z} \dot{u}_n \left(\frac{\sqrt{2n}}{2n-(2m-1)} - \frac{\sqrt{2(n-1)}}{2(n-1)-(2m-1)} \right) \quad (A5.1)$$

ie.
$$\sigma_{m,c} = B \sum_{n=1}^{z} \dot{u}_n f(n,m) \quad (A5.2)$$

Thouless presents plots of normalised stress, $\sigma\sqrt{l}/K$, as a function of position within the damage zone (which he arbitrarily assumes to be of 10 grains) for various values of l/λ. This stress, σ, is the applied elastic stress minus the constraint and is given by

$$\sigma = \sigma_{a,m} - \sigma_{c,m} \quad (A5.3)$$

where
$$\sigma_{a,m} = \frac{K}{\sqrt{\pi(2m-1)l}} \quad (A5.4)$$

Now if we denote normalised stresses by the presence of a superscripted bar then obviously

$$\bar{\sigma}_{c,m} = \bar{\sigma}_{a,m} - \bar{\sigma} \quad (A5.5)$$

and if we define

$$B' \equiv B\sqrt{2m-1} \quad (A5.6)$$

then it follows from equation (A5.1) that

$$[\bar{\sigma}_{c,m}] = B'[f(n,m)] [I'] [\dot{u}_n] \quad (A5.7)$$

where [I'] is the modified identity matrix thus

$$
[I'] = \begin{bmatrix} 1 & 0 & 0 & & \\ 0 & 1/\sqrt{3} & 0 & & \\ 0 & 0 & 1/\sqrt{5} & & \\ & & & & \\ & & & & \dfrac{1}{\sqrt{2m-1}} \end{bmatrix}
\qquad\qquad (A5.8)
$$

and so

$$
\dot{u}_n = \frac{1}{B'} \left[f_{n,m} I' \right]^{-1} \bar{\sigma}_{c,m}
\qquad\qquad (A5.9)
$$

In order to obtain the displacement rate field the z by z matrix $[f_{n,m}I']$ must first be formed and then inverted. The normalised stress distribution within the damage zone can be read from the graph and by simple matrix multiplication the displacement rate distribution can be obtained. The values of $[f_{n,m}I']$ and $[f_{n,m}I']^{-1}$ are given on the following pages.

$$[f_{n,n} I^l] = \begin{bmatrix}
1.414 & -0.747 & -0.177 & -0.086 & -0.053 & -0.036 & -0.027 & -0.021 & -0.017 & -0.014 \\
-0.816 & 1.917 & -0.648 & -0.145 & -0.066 & -0.039 & -0.026 & -0.018 & -0.014 & -0.012 \\
-0.211 & -0.684 & 1.990 & -0.674 & -0.139 & -0.062 & -0.035 & -0.023 & -0.017 & -0.013 \\
-0.107 & -0.145 & -0.674 & 1.995 & -0.671 & -0.136 & -0.060 & -0.034 & -0.022 & -0.016 \\
-0.067 & -0.066 & -0.139 & -0.671 & 1.997 & -0.669 & -0.135 & -0.059 & -0.033 & -0.022 \\
-0.047 & -0.039 & -0.062 & -0.137 & -0.669 & 1.998 & -0.668 & -0.135 & -0.058 & -0.033 \\
-0.036 & -0.026 & -0.036 & -0.060 & -0.135 & -0.668 & 1.999 & -0.668 & -0.135 & -0.058 \\
-0.028 & -0.019 & -0.023 & -0.034 & -0.059 & -0.135 & -0.668 & 1.999 & -0.668 & -0.134 \\
-0.023 & -0.015 & -0.017 & -0.022 & -0.033 & -0.058 & -0.134 & -0.668 & 1.997 & -0.667 \\
-0.019 & -0.011 & -0.013 & -0.016 & -0.022 & -0.033 & -0.058 & -0.134 & -0.667 & 1.999
\end{bmatrix}$$

(A5.10)

$$[f_{n,n} I'^l]^{-1} = \begin{bmatrix} 1.334 & 0.791 & 0.616 & 0.510 & 0.430 & 0.364 & 0.304 & 0.274 & 0.189 & 0.122 \\ 0.882 & 1.171 & 0.732 & 0.573 & 0.472 & 0.393 & 0.325 & 0.263 & 0.200 & 0.128 \\ 0.709 & 0.745 & 1.120 & 0.692 & 0.537 & 0.435 & 0.354 & 0.283 & 0.214 & 0.136 \\ 0.569 & 0.590 & 0.697 & 1.081 & 0.655 & 0.499 & 0.395 & 0.310 & 0.231 & 0.146 \\ 0.507 & 0.489 & 0.543 & 0.658 & 1.042 & 0.616 & 0.457 & 0.348 & 0.255 & 0.159 \\ 0.433 & 0.410 & 0.442 & 0.503 & 0.617 & 1.000 & 0.570 & 0.406 & 0.288 & 0.176 \\ 0.364 & 0.341 & 0.362 & 0.399 & 0.459 & 0.571 & 0.950 & 0.515 & 0.340 & 0.200 \\ 0.298 & 0.276 & 0.290 & 0.314 & 0.350 & 0.407 & 0.515 & 0.887 & 0.440 & 0.240 \\ 0.229 & 0.211 & 0.219 & 0.234 & 0.257 & 0.289 & 0.340 & 0.440 & 0.789 & 0.319 \\ 0.147 & 0.134 & 0.139 & 0.148 & 0.159 & 0.176 & 0.200 & 0.240 & 0.319 & 0.637 \end{bmatrix} \tag{A5.11}$$

For $l/\lambda = 20$

$$
[\bar{\sigma}_{c,m}] = \begin{bmatrix} 0.574 \\ 0.303 \\ 0.224 \\ 0.179 \\ 0.148 \\ 0.124 \\ 0.104 \\ 0.088 \\ 0.073 \\ -0.417 \end{bmatrix} \quad \therefore \quad B'\dot{U}_n = \begin{bmatrix} 1.366 \\ 1.264 \\ 1.161 \\ 1.053 \\ 0.940 \\ 0.820 \\ 0.689 \\ 0.542 \\ 0.359 \\ 0.027 \end{bmatrix} \qquad (A5.12)
$$

and for $l/\lambda = 5$

$$
[\bar{\sigma}_{c,m}] = \begin{bmatrix} 0.414 \\ 0.141 \\ 0.034 \\ -0.016 \\ -0.037 \\ -0.042 \\ -0.044 \\ -0.036 \\ -0.024 \\ -0.079 \end{bmatrix} \quad \therefore \quad B'\dot{U}_n = \begin{bmatrix} 0.613 \\ 0.473 \\ 0.346 \\ 0.245 \\ 0.171 \\ 0.118 \\ 0.080 \\ 0.053 \\ 0.031 \\ 0.007 \end{bmatrix} \qquad (A5.13)
$$

Plots of the displacement rate distribution described by equations (A5.12) and (A5.13) are given in Figures (4.5a) and (4.5b).

The accuracy with which these fields have been extracted can be determined by evaluating C^* around the damage zone. In closed form

$$
C^* = \oint_R \sigma \, d\dot{u} \qquad (A5.14)
$$

but as Thouless only presents discrete values of σ and hence $\dot{u}$ we must write

$$C^* = \Sigma \ \sigma \frac{d\dot{u}}{dx} dl = \Sigma \ \sigma_{mean}(\dot{u}_n - \dot{u}_{n+1}) \qquad (A5.15)$$

where
$$\sigma_{mean} = \frac{\sigma_n + \sigma_{n+1}}{2} \qquad (A5.16)$$

Thouless plots the stresses at the mid points of the grains and the displacements, for $l/\lambda = 20$ and $l/\lambda = 5$, are given in equations (A5.12) and (A5.13) respectively. Using linear interpolation to determine σ_{mean} and summing over a damage zone of 10 grains we obtain, for $l/\lambda = 20$,

$$C^* = 0.170 \frac{3\pi}{2\eta} K^2 = 0.80 \frac{K^2}{\eta} \qquad (A5.17)$$

If this procedure is repeated for the case where $l/\lambda = 5$ then we find

$$C^* = 0.1342 \frac{3\pi}{2\eta} K^2 = 0.63 \frac{K^2}{\eta} \qquad (A5.18)$$

Recall from equation (4.34) that for the purpose of comparing our results with Thouless' we are assuming

$$K^2 = \eta \ C^* \qquad (A5.19)$$

under plane strain conditions this becomes

$$K^2 = \frac{\eta C^*}{(1 - v^2)} \qquad (A5.20)$$

which means that, as $v = 0.5$ for a linear viscous material,

$$C^* = 0.75 \frac{K^2}{\eta} \qquad (A5.21)$$

By comparing equations (A5.17), (A5.18) with (A5.21) we can see that the fields depicted in Figures (4.5a) and (4.5b) are quite accurate.

APPENDIX 6

Specimen no: P1   Bending moment: 9.84Nm

Initial elastic strain = 750μ

time (h)	creep strain (μ)	time (h)	creep strain (μ)	time (h)	creep strain (μ)
1	356				
1.8*	544*				

* Strain / Time to failure

Specimen no: P4   Bending moment: 8.44Nm

Initial elastic strain = 506μ

time (h)	creep strain (μ)	time (h)	creep strain (μ)	time (h)	creep strain (μ)
1	169	30	788		
2	224	31	797		
3	263	32	835		
4	300	33	853		
5	328	34	872		
6	366	35	891		
7	394	36	928		
8	422	37	928		
9	441	38	938		
10	460	39	947		
11	478	40	975		
12	507	41	994		
13	525	42	1013		
14	535	43	1050		
15	553	44	1069		
16	572	44.75*	1088*		
17	582				
18	600				
19	610				
20	628				
21	638				
22	647				
23	666				
24	685				
25	703				
26	713				
27	732				
28	750				
29	760				

* Time / Strain to failure

Specimen no: P6   Bending moment: 8.44Nm

Initial Strain = 619μ

time (h)	creep strain (μ)	time (h)	creep strain (μ)	time (h)	creep strain (μ)
1	159	30	806		
2	206	31	816		
3	234	32	834		
4	272	33	853		
5	281	34	863		
6	300	35	881		
7	319	36	891		
8	338	37	909		
9	366	38	919		
10	394	39	938		
11	403	40	956		
12	422	41	956		
13	459	42	984		
14	478	43	1003		
15	497	44	1041		
16	488	45	1059		
17	497	46	1088		
18	516	47	1116		
19	534	48	1163		
20	572	49	1181		
21	591	50	1191		
22	609	51	1209		
23	628	52	1228		
24	656	53	1238		
25	713	54	1256		
26	741	55	1275		
27	759	55.7*	1284*		
28	778				
29	797				

* Strain / Time to failure

Specimen no: P7   Bending moment: 10.31Nm

Initial elastic strain = 806μ

time (h)	creep strain (μ)	time (h)	creep strain (μ)	time (h)	creep strain (μ)
1	122				
2	206				
3	272				
4	345				
5	384				
6	413				
7	441				
8	488				
9	525				
10	572				
11	600				
12	638				
12.4*	647*				

* Strain / Time to failure

Specimen no: P17   Bending moment: 9.84Nm

Initial elastic strain = 750μ

time (h)	creep strain (μ)	time (h)	creep strain (μ)	time (h)	creep strain (μ)
1	188	30	872		
2	272	31	881		
3	309	31.75*	900*		
4	347				
5	366				
6	384				
7	413				
8	441				
9	422				
10	431				
11	459				
12	450				
13	478				
14	506				
15	544				
16	553				
17	572				
18	591				
19	609				
20	628				
21	647				
22	656				
23	722				
24	741				
25	778				
26	806				
27	825				
28	844				
29	863				

Strain / Time to failure

Specimen no: P18   Bending moment: 11.25Nm

Initial elastic strain = 844μ

time (h)	creep strain (μ)	time (h)	creep strain (μ)	time (h)	creep strain (μ)
1	197				
2	244				
3	309				
4	356				
5	384				
6	422				
7	469				
8	506				
9	534				
10	572				
11	609				
11.1*	609				

Strain / Time to failure

Specimen no: P19   Bending moment: 8.44Nm

Initial elastic strain = 731μ

time (h)	creep strain (μ)	time (h)	creep strain (μ)	time (h)	creep strain (μ)
1	347				
2	450				
3	525				
4	582				
5	638				
6	741				
7	732				
8	788				
9	807				
10	844				
11	882				
12	919				
13	1013				
14	985				
15	1022				
16	1097				
17	1144				
17.6*	1116*				

* Time / Strain to failure

Specimen no: P23   Bending moment: Unknown due to bearing seizure

Initial elastic strain unknown

time (h)	creep strain (μ)	time (h)	creep strain (μ)	time (h)	creep strain (μ)
1	113	30	984	59	1275
2	225	31	1003	60	1294
3	319	32	1013	61	1303
4	394	33	1031	62	1313
5	450	34	1041	63	1322
6	544	35	1050	64	1331
7	544	36	1050	65	1341
8	563	37	1069	66	1350
9	600	38	1088	67	1359
10	619	39	1097	68	1369
11	656	40	1116	69	1378
12	713	41	1116	70	1397
13	731	42	1125	71	1397
14	806	43	1144	72	1406
15	713	44	1153	73	1425
16	825	45	1153	74	1434
17	788	46	1163	75	1444
18	825	47	1172	76	1453
19	844	48	1191	77	1453
20	881	49	1200	78	1463
21	891	50	1209	79	1463
22	919	51	1219	80	1463
23	928	52	1228	81	1472
24	928	53	1238	82	1481
25	938	54	1238	83	1491
26	947	55	1256	84	1491
27	966	56	1266	85	1500
28	975	57	1266	86	1509
29	984	58	1275	87	1519

Specimen no: P23 Continued   Bending moment: Unknown

time (h)	creep strain (μ)	time (h)	creep strain (μ)	time (h)	creep strain (μ)
88	1556	117	1856	146	2063
89	1556	118	1875	147	2081
90	1575	119	1875	148	2081
91	1575	120	1884	149	2091
92	1594	121	1894	150	2119
93	1613	122	1894	151	2119
94	1622	123	1903	152	2119
95	1650	124	1913	153	2109
96	1650	125	1922	154	2119
97	1641	126	1922	155	2119
98	1641	127	1931	156	2119
99	1650	128	1931	157	2128
100	1669	129	1941	158	2138
101	1678	130	1941	159	2147
102	1688	131	1931	160	2166
103	1697	132	1931	161	2184
104	1688	133	1941	162	2203
105	1688	134	1950	163	2194
106	1697	135	1959	164	2213
107	1706	136	1988	165	2231
108	1706	137	1997	166	2231
109	1725	138	2006	167	2241
110	1725	139	2025	168	2241
111	1734	140	2025	169	2250
112	1763	141	2025	170	2250
113	1772	142	2044	171	2259
114	1791	143	2044	172	2269
115	1800	144	2053	173	2269
116	1819	145	2063	174	2278

Specimen no: P23 Continued   Bending moment: Unknown

time (h)	creep strain (μ)	time (h)	creep strain (μ)	time (h)	creep strain (μ)
175	2269	204	2484	233	2616
176	2278	205	2484	234	2616
177	2278	206	2494	235	2616
178	2288	207	2494	236	2616
179	2278	208	2503	237	2625
180	2288	209	2503	238	2644
181	2288	210	2513	239	2653
182	2306	211	2513	240	2653
183	2316	212	2522	241	2663
184	2325	213	2522	242	2653
185	2344	214	2531	243	2644
186	2363	215	2541	244	2644
187	2363	216	2550	245	2644
188	2372	217	2550	246	2644
189	2381	218	2550	247	2663
190	2400	219	2559	248	2663
191	2400	220	2550	249	2663
192	2400	221	2550	250	2672
193	2409	222	2569	251	2663
194	2419	223	2550	252	2681
195	2419	224	2559	253	2681
196	2438	225	2569	254	2681
197	2438	226	2588	255	2691
198	2456	227	2588	256	2691
199	2456	228	2588	257	2700
200	2466	229	2606	258	2709
201	2475	230	2606	259	2719
202	2475	231	2606	260	2719'
203	2475	232	2625	261	2719

Specimen no: P23 Continued   Bending moment: Unknown

time (h)	creep strain (μ)	time (h)	creep strain (μ)	time (h)	creep strain (μ)
262	2738	291	2888	320	3019
263	2738	292	2897	321	3019
264	2738	293	2906	322	3028
265	2756	294	2906	323	3019
266	2766	295	2916	324	3019
267	2766	296	2925	325	3019
268	2775	297	2897	326	3028
269	2784	298	2897	327	3028
270	2794	299	2897	328	3038
271	2803	300	2897	329	3047
272	2813	301	2897	330	3047
273	2794	302	2916	331	3056
274	2784	303	2916	332	3056
275	2784	304	2934	333	3066
276	2784	305	2944	334	3075
277	2794	306	2944	335	3056
278	2794	307	2935	336	3056
279	2813	308	2963	337	3028
280	2831	309	2963	338	3019
281	2831	310	2972	339	3019
282	2841	311	2972	340	3009
283	2831	312	2981	341	3028
284	2841	313	3000	342	3028
285	2859	314	3000	343	3028
286	2859	315	3009	344	3028
287	2869	316	3000	345	3038
288	2869	317	3009	346	3056
289	2869	318	3009	347	3038
290	2878	319	3009	348	3047

time (h)	creep strain (μ)	time (h)	creep strain (μ)	time (h)	creep strain (μ)
349	3047	378	3169	407	3263
350	3056	379	3178	408	3263
351	3075	380	3169	409	3244
352	3075	381	3188	410	3263
353	3084	382	3188	411	3263
354	3094	383	3178	412	3272
355	3094	384	3188	413	3272
356	3094	385	3169	414	3272
357	3094	386	3178	415	3281
358	3113	387	3178	416	3281
359	3113	388	3188	417	3291
360	3084	389	3178	418	3281
361	3094	390	3188	419	3281
362	3094	391	3188	420	3281
363	3113	392	3206	421	3291
364	3113	393	3197	422	3291
365	3113	394	3197	423	3300
366	3113	395	3206	424	3338
367	3113	396	3216	425	3338
368	3131	397	3206	426	3347
369	3131	398	3216	427	3375
370	3131	399	3225	428	3356
371	3141	400	3234	429	3375
372	3141	401	3234	430	3375
373	3150	402	3244	431	3413
374	3159	403	3244	432	3413
375	3169	404	3253	433	3394
376	3178	405	3244	434	3375
377	3188	406	3263	435	3366

time (h)	creep strain (μ)	time (h)	creep strain (μ)	time (h)	creep strain (μ)
436	3384	465	3478	494	3591
437	3394	466	3478	495	3591
438	3375	467	3488	496	3619
439	3375	468	3488	497	3619
440	3384	469	3497	498	3609
441	3394	470	3488	499	3619
442	3394	471	3506	500	3628
443	3394	472	3544	501	3628
444	3413	473	3534	502	3638
445	3394	474	3544	503	3647
446	3394	475	3553	504	3666
447	3394	476	3572	505	3619
448	3450	477	3581	506	3619
449	3450	478	3600	507	3619
450	3469	479	3581	508	3581
451	3469	480	3572	509	3563
452	3469	481	3553	510	3563
453	3469	482	3563	511	3581
454	3478	483	3563	512	3572
455	3488	484	3563	513	3581
456	3488	485	3572	514	3581
457	3469	486	3581	515	3572
458	3459	487	3581	516	3581
459	3459	488	3581	517	3591
460	3459	489	3591	518	3591
461	3469	490	3581	519	3600
462	3469	491	3591	520	3628
463	3469	492	3591	521	3628
464	3469	493	3591	522	3638

Specimen no: P23 Continued   Bending moment: Unknown

time (h)	creep strain (μ)	time (h)	creep strain (μ)	time (h)	creep strain (μ)
523	3628	552	3656	581	3722
524	3638	553	3656	582	3713
525	3638	554	3656	583	3731
526	3656	555	3675	584	3741
527	3638	556	3666	585	3731
528	3647	557	3656	586	3750
529	3628	558	3666	587	3750
530	3619	559	3675	588	3741
531	3638	560	3675	589	3769
532	3628	561	3675	590	3797
533	3638	562	3675	591	3778
534	3628	563	3675	592	3788
535	3638	564	3675	593	3788
536	3638	565	3684	594	3797
537	3638	566	3675		
538	3638	567	3684		
539	3638	568	3694		
540	3638	569	3694		
541	3638	570	3694		
542	3647	571	3694		
543	3638	572	3694		
544	3638	573	3694		
545	3647	574	3694		
546	3647	575	3694		
547	3647	576	3703		
548	3647	577	3713		
549	3647	578	3713		
550	3647	579	3713		
551	3656	580	3713		

Specimen no: P24   Bending moment: 9.84Nm

Initial elastic strain = 750μ

time (h)	creep strain (μ)	time (h)	creep strain (μ)	time (h)	creep strain (μ)
1	244				
2	366				
3	459				
4	544				
5	609				
5.2*	628*				

* Time / Strain to failure

REFERENCES

1   PHILLIPS, P. (1903-05) *Proc. Phys. Soc.* **19** 491.

2   EVANS, R. W., PARKER, J. D. and WILSHIRE, B. (1982) In: *Recent Advances in Creep and Fracture of Engineering Materials and Structures.* (eds. WILSHIRE, B. and OWEN, D. R. J.) Pineridge Press, Swansea. 135.

3   NORTON, F. H. (1929) *Creep of Steel at High Temperatures.* Mc Graw Hill, New York.

4   CANNON, R. W. and LANGDON, T. G. (1983) *J. Mat. Sci.* **18** 1.

5   COBLE, R. L. (1963) *J. Appl. Phys.* **34** 1679.

6   COCKS, A. C. F. and SEARLE, A. A. (1990) *Acta Metall. Mater.* **12** 2493.

7   NABARRO, F. R. N. (1948) In: *Proc. Conference on Strength of Solids.* Physical Society, London. 75.

8   HERRING, C. (1950) *J. Appl. Phys.* **21** 437.

9   RAJ, R. and ASHBY, M. F. (1975) *Acta Met.* **23** 653.

10   ARGON, A. S. (1983) *Scripta Met.* **17** 5.

11   ARGON, A. S., CHEN, I. -W. and LAU, C. W. (1981) In: *Three - Dimensional Constitutive Relations and Ductile Fracture.* (ed. Nemat-Nasser, S.) North Holland Publishing Company, Amsterdam New York Oxford. 23.

12   GRANT, N. J. and MULLENDORE, A. W. (1965) *Deformation and Fracture at Elevated Temperatures.* M. I. T. Press, Cambridge, Mass.

13   GOODS, S. H. and NIX, W. D. (1978) *Acta Met.* **26** 739.

14   DYSON, B. F. (1983) *Scripta Met.* **17** 31.

15   HULL, D. and RIMMER, D. E. (1959) *Phil. Mag.* **4** 673.

16   SPEIGHT, M. V. and HARRIS, J. E. (1967) *Metal Sci.* **1** 83.

17   COCKS, A. C. F. and ASHBY, M. F. (1982) *Metal Sci.* **16** 465.

18   CHUANG, T. -J., KAGAWA, K. I., RICE, J. R. and SILLS, L. B. (1979) *Acta Met.* **27** 265.

19   EDWARD, G. H. and ASHBY, M. F. (1979) *Acta Met.* **27** 1505.

20   BEER, W. and SPEIGHT, M. V. (1978) *Metal Sci.* **12** 172.

21   COCKS, A. C. F. and ASHBY, M. F. (1980) *Metal Sci.* **14** 395.

22   DALGLEISH, B. J., SLAMOVICH, E. B. and Evans, A. G. (1985) *J. Am. Ceram. Soc.* **68** 575.

23   SIVERNS, M. J. and PRICE A. T. (1970) *Nature.* **228** 760.

24   LEEUWEN, H. P. VAN (1977) *Eng. Fracture Mech.* **9** 951.

25   RIEDEL, H. (1985) In: *Flow and Fracture at Elevated Temperatures.* (ed. Raj, R.) American Society for Metals, Metals Park, Ohio. 149.

26   GRIFFITH, A. A. (1921) *Proc. R. Soc. Lond.* A **221** 163.

27   INGLIS, C. E. (1913) *Trans. Inst. Naval Architects* **55** 219.

28   IRWIN, G. R. (1960) *Proc. 7th Sagamore Conf.* iv.

29   DUGDALE, D. S. (1960) *J. Mech. Phys. Sol.* **8** 100.

30   RICE, J. (1968) In: *Fracture. An Advanced Treatise.* (ed. Liebowitz, H., Vol. 2) Academic Press, New York. 191.

31   HOFF, N. J. (1954) *Quart. Appl. Math.* **12** 49.

32   LANDES, J. D. and BEGLEY, J. A. (1976) In: *Mechanics of Crack Growth, ASTM STP 590.* American Society for Testing and Materials. 128.

33   NIKBIN, K. M., WEBSTER, G. A. and TURNER, C. E. (1975) In: *Cracks and Fracture - Proceedings of the Ninth National Symposium on Fracture Mechanics.* (Chairmen Swedlow, J. L. and Williams, M. L.) ASTM Special Technical Publication 601. ASTM. Philadelphia.

34   AINSWORTH, R. A. (1982) *Int. J. Fracture.* **20** 147.

35   THOULESS, M. D., HSEUH, C. H. and EVANS, A. G. (1983) *Acta Met.* **31** 1675.

36   ASHBY, M. F., GANDHI, C. and TAPLIN, D. M. R. (1979) *Acta Met.* **27** 699.

37   GHANDI, C. and ASHBY, M. F. (1979) *Acta Met.* **27** 1565.

38   ANDRADE, E. N. (1910) *Proc. Roy. Soc.* A**84** 1.

39   LARSON, F. R. and MILLER, J. (1952) *Trans. ASME* **74** 765.

40   ORR, R. L., SHERBY, O. D. and DORN, J. E. (1954) *Trans. ASME* **76** 113.

41   MONKMAN, F. C. and GRANT, N. J. (1956) *Proc. ASTM* **56** 593.

42   EVANS, H. E. (1984) *Mechanisms of Creep Ruptuure*. Elsveier Applied Science. London and New York.

43   KACHANOV, L. M. (1960) *The Theory of Creep*. English Translation (ed. Kennedy, A. J.).

44   RABOTNOV, Y. N. (1969) *Creep Problems in Structural Members* English Translation by Leckie, F. A. North-Holland. Amsterdam.

45   HARRISON, C. B. and SANDOR, G. N. (1971) *Eng. Fracture Mech.* **3** 403.

46   HUTCHINSON, J. W. (1968) *J. Mech. Phys. Sol.* **16** 13.

47   HUTCHINSON, J. W. (1968) *J. Mech. Phys. Sol.* **16** 337.

48   RICE, J. R. and ROSENGREN G. F. *J. Mech. Phys. Sol.* **16** 1.

49   RIEDEL, H. (1987) *Fracture at High Temperatures*. Springer-Verlag, Berlin.

50   GOLDMAN, N. L. and HUTCHINSON J. W. (1975) *Int. J. Solids Struct.* **11** 575.

51   HAIGH, J. R. (1975) *Mater. Sci. Engng.* **20** 213.

52   AINSWORTH, R. A. (1982) *Int. J. Solids Struct.* **18** 873.

53   RIEDEL, H. and RICE, J. R. (1979) *Brown University Report E(11-1) 3084-64.*

54   BASSANI, J. L. and McCLINTOCK, F. A. (1981) *Int. J. Solids Struct.* **17** 479.

55   HUI, C. Y. and RIEDEL, H. (1979) *Brown University Report MRL E-117.*

56   ANDERSON, R. G., GARDNER, L. R. T. and HODGKINS, W. R. (1963) *J. Mech. Engng. Sci.* **5** 238.

57   MARRIOTT, D. L. and LECKIE, F. A. (1964) *Proc. I. Mech. E.* **178** Pt. 3L 115.

58   SIM, R. G. (1968) PhD Thesis, University of Cambridge.

59   LECKIE, F. A. and MARTIN, J. B. (1967) *J. Appl. Mech.* **34** 411.

60   LECKIE, F. A. and PONTER, A. R. S. (1970) *J. Appl. Mech.* **37** 426.

61   LECKIE, F. A. and PONTER, A. R. S. (1970) *J. Appl. Mech.* **37** 753.

62   PONTER, A. R. S. (1972) *J. Appl. Mech.* **39** 953.

63   GOODALL, I. W. and COCKROFT R. D. H. (1973) *Int. J. Mech. Sci.* **15** 251.

64   GOODALL, I. W. and CHUBB, E. J. (1976) *Int. J. Fract.* **12** 289.

65   HAIGH, J. R. (1975) *Materials Science and Engineering* **20** 225.

66   NEATE, G. J. (1977) *Eng. Fracture Mech.* **9** 297.

67   NEATE, G. J. (1978) *Materials Science and Engineering* **33** 165.

68   BASSANI, J. L. and McCLINTOCK, F. A. (1981) *Int. J. Solids Struct.* **17** 179.

69   HAWK, D. E. and BASSANI, J. L. (1986) *J. Mech. Phys. Sol.* **34** 191.

70   RIEDEL, H. (1981) *J. Mech. Phys. Sol.* **29** 35.

71   CHUANG, T. -J. (1982) *J. Am. Ceram. Soc.* **65** 93.

72   NIKBIN, K. M. and WEBSTER G. A. (1982) In: *Micro and Macro Mechanics of Crack Growth.* (eds. Sadananda, K., Bath, B. B. and Michael, D. J.) AIME 137.

73   COCKS, A. C. F. and ASHBY, M. F. (1982) *Scripta Met.* **16** 109.

74   NIKBIN, K. M., SMITH, D. J. and WEBSTER, G. A. (1984) *Proc. R. Soc. Lond.* A **396** 183.

75   WILKINSON, D. S. and VITEK, V. (1982) *Acta Met.* **30** 1722.

76   AINSWORTH, R. A. (1989) In: *Mechanics of Creep Brittle Materials - 1.* (eds. Cocks, A. C. F. and Ponter, A. R. S.) Elsevier Applied Science, London and New York. 13.

77   WEBSTER, G. A. (1989) In: *Mechanics of Creep Brittle Materials - 1.* (eds. Cocks, A. C. F. and Ponter, A. R. S.) Elsevier Applied Science, London and New York. 36.

78   AINSWORTH, R. A. and BUDDEN, P. J. (1990) *Fatigue Fract. Engng. Mater. Struct.* **13** 263.

79 AINSWORTH, R. A. and BUDDEN, P. J. (1990) *Fatigue Fract. Engng. Mater. Struct.* **13** 277.

80 FINNIE, I. and HELLER, W. R. (1959) *Creep of Engineering Materials*. McGraw-Hill, New York.

81 BASSANI, J. L. (1983) In: *Elastic-Plastic Fracture: Second Symposium Vol. 1. Inelastic Crack Analysis. ASTM STP 803*. American Society for Testing and Materials. I-532.

82 GOVILA, R. K. (1980) *J. Am. Ceram. Soc.* **63** 319.

83 THOULESS, M. D. (1988) In: *Mechanics of Creep Brittle Materials - 1.* (eds. Cocks, A. C. F. and Ponter, A. R. S.) Elsevere. London New York.

84 THOULESS, M. D. and EVANS, A. G. (1986) *Acta Met.* **34** 23.

85 THOULESS, M. D. (1988) *J. Am. Ceram. Soc.* **71** 408.

86 McMEEKING, R. M. (1977) *J. Mech. Phys. Sol.* **25** 357.

87 RIEDEL, H. (1985) IN: *Fundamentals of Deformation and Fracture*. (eds. Bilby, B. A. et. al.) Cambridge University Press. Cambridge.

88 BLUMENTHAL, W. and EVANS, A. G. (1984) *J. Am. Ceram. Soc.* **67** 751.

89 UD DIN, S. and NICHOLSON, P. S. (1975) *J. Mat. Sci.* **10** 1375.

90 GRATHWOL, G. and THÜMMLER, F. (1978) *J. Mat. Sci.* **13** 1177.

91 GOODMAN, A. M., HEATON, M. D., MARTIN D. C., MORSE, D. C., PHILLIPS, J. and FIELDING, J. (1988) *R5: An assessment procedure for the high temperature response of structures, volume 2: proposed analysis and assessment methods for defect free structures*. CEGB Report.

92 NEEDLEMAN, A. and RICE, J. R. (1980) Acta Met. **28** 1315.

93 RAJ, R., SHIH, H. M. and JOHNSON, H. H. (1977) *Scripta Met.* **11** 839.

94 DYSON, B. F. (1976) *Metal Sci.* **10** 349.

95 CHUANG, T. -J. and RICE, J. R. (1973) *Acta Met.* **21** 1625.

96 RIEDEL, H. (1980) In: *Creep in Structures - IUTAM symposium Leicester/UK* (eds. Ponter, A. R. S. and Hayhurst, D. R.) Springer-Verlag. Berlin Heidelberg New York.

97   COCKS, A. C. F. and ASHBY, M. A. (1982) *Prog. Mat. Sci* **27** 189.

98   BS 3500 *British Standard Methods for Creep and Rupture Testing of Metals.*

99   TALTY, P. K. and DIRKS, R. A. (1978) *J. Mat. Sci.* **13** 580.

100   *The Concise Oxford Dictionary.* (1990) Oxford University Press.

101   WEIBULL, W. (1939) *Ing. Ventenstape Akad.* **151** 1.

102   KAMO, R. and BRYZIK, W. (1984) In: *Proceedings of the 21st Automotive Contractors Coordination Meeting.* Society of Automotive Engineers, Warrendale, PA.

103   COCKS, A. C. F. and PONTER, A. R. S. (1989) *Nuclear Engineering and Design* **116** 363.

104   TADA, H., PARIS, P. C. and IRWIN, G. R. (1973) *Stress Analysis of cracks Handbook.* Del Research Corporation, Hellertown, Pennsylvania.

105   *Materials Data* (1982) Cambridge University Engineering Department. 22.